DEEP LEARNING INTEGRATION OF DIVERSE DATA TYPES FOR SURVIVAL PREDICTION IN SEROUS OVARIAN CANCER

by

Fatma Ezgi Öğülmüş

M.D., in Medicine, Koç University, 2021

Submitted to the Institute of Biomedical Engineering
in partial fulfillment of the requirements
for the degree of
Master of Science
in
Biomedical Engineering

Boğaziçi University
2024

DEEP LEARNING INTEGRATION OF DIVERSE DATA TYPES FOR SURVIVAL PREDICTION IN SEROUS OVARIAN CANCER

APPROVED BY:

Assoc. Prof. Dr. Mehmet Turan .....
(Thesis Co-advisor)

Prof. Dr. Albert Güveniş .....
(Thesis Co-advisor)

Prof. Dr. Cengizhan Öztürk .....

Prof. Dr. Ahmet Ademoğlu .....

Prof. Dr. Handan Özdemir .....

DATE OF APPROVAL: 2 April 2024

ACKNOWLEDGMENTS

This work acknowledges the use of ChatGPT by OpenAI for improving the manuscript's language clarity and readability.

ACADEMIC ETHICS AND INTEGRITY STATEMENT

I, Fatma Ezgi Öğülmüş, hereby certify that I am aware of the Academic Ethics and Integrity Policy issued by the Council of Higher Education (YÖK) and I fully acknowledge all the consequences due to its violation by plagiarism or any other way.

Name :

Signature:

Date:

ABSTRACT

DEEP LEARNING INTEGRATION OF DIVERSE DATA TYPES FOR SURVIVAL PREDICTION IN SEROUS OVARIAN CANCER

Ovarian cancer, known for its high mortality and treatment resistance, demands precise survival predictions for personalized treatments. This research develops the Ovarian Cancer Vision Transformer Aggregated Network (OViTANet), a novel deep learning model that forecasts survival in serous ovarian cancer by combining histopathology images with clinical and genetic data, such as mutations, copy-number variations, mRNA-sequencing, DNA methylation, and protein expressions. Using data from the Cancer Genome Archive, OViTANet was developed and rigorously tested. Moreover an external validation set procured from Başkent University Hospital was used to evaluate the effectiveness of the image feature extractors in the model. The performance of OViTANet was meticulously categorized based on the data categories, each reflecting varying sample sizes due to the disparate availability of genetic data. When compared to an existing multi-modal network in the literature, OViTANet outperforms across all data categories for predicting overall survival, with concordance indices ranging from 0.5991 ± 0.0369 to 0.6902 ± 0.0499. Although the model's efficacy slightly diminished for disease-free survival prediction–with concordance indices spanning 0.5385 ± 0.052 to 0.5989 ± 0.0284–it still performed better than the comparative model across most data categories. This work not only enhances survival prediction through data integration but also contributes to understanding serous ovarian cancer's genetic traits, marking a significant advancement in oncological analysis and leading to more effective, personalized treatments to improve patient outcomes.

Keywords: Serous Ovarian Cancer, Survival Prediction, Deep Learning, Histopathology Images, Clinical Data, mRNA-Sequencing, DNA Methylation, Copy Number Variation, Protein Expression, Feature Selection, Multi-modal Fusion, OViTANet

ÖZET

FARKLI VERİ TİPLERİNİ BİRLEŞTİREN DERİN ÖĞRENME İLE SERÖZ YUMURTALIK KANSERİNDE SAĞKALIM TAHMİNİ

Yüksek mortalite oranları ve tedaviye dirençli olması ile bilinen yumurtalık kanserinde, kişiselleştirilmiş tedaviler için hayatta kalma tahminleri önemlidir. Bu araştırmada, histopatoloji görüntüleri ile klinik ve genetik verileri (mutasyonlar, kopya sayısı varyasyonları, mRNA sekanslaması, DNA metilasyonu ve protein ekspresyonu) birleştirerek seröz yumurtalık kanserinde hayatta kalma süresini tahmin eden yeni bir derin öğrenme modeli olan OViTANet geliştirilmiştir. Model oluşturma ve test etmede Amerika'nın kanser arşivi'nden alınan veriler, model içindeki görüntü özellik çıkarıcılarının etkinliğini değerlendirmek üzere Başkent Üniversitesi Hastanesi'nden toplanan doğrulama seti kullanılmıştır. OViTANet'in performansı, her genetik verinin her hastada bulunmaması sebebiyle değişen örneklem sayılarını göz önüne alarak, farklı veri kategorilerinde değerlendirilmiştir. Literatürdeki başka bir çoklu-modalite füzyonu yapan derin öğrenme temelli sağkalım modeli ile karşılaştırıldığında, OViTANet, genel hayatta kalma tahminlerinde konkordans indeksi 0.5991 ± 0.0369 ile 0.6902 ± 0.0499 arasında değişmek üzere tüm veri kategorilerinde üstün performans göstermiştir. Modelin hastalıksız hayatta kalma tahmini performansı daha düşük olsa da –uyum indeksleri 0.5385 ± 0.052 ile 0.5989 ± 0.0284 arasında değişmektedir– karşılaştırmalı modele göre çoğu veri kategorisinde daha iyi performansa sahip olduğu görülmüştür. Bu çalışma, sadece hayatta kalma tahminini farklı veri tiplerinin birleştirerek geliştirmekle kalmayıp, aynı zamanda seröz yumurtalık kanserinin genetik özelliklerini anlama konusunda da katkıda bulunmuş, böylece kişiselleştirilmiş tedaviler geliştirilmesine yardımcı olmayı ve hasta sonuçlarını iyileştirmeyi hedeflemiştir.

Anahtar Sözcükler: Seröz Yumurtalık Kanseri, Sağkalım Tahmini, Derin Öğrenme, Histopatoloji Görüntöleri, Klinik Veri, mRNA Sekanslaması, DNA Metilasyonu, Kopya Sayısı Değişikliği, Protein Ekspresyonu, Özellik Seçimi, Çoklu-Modalite Füzyonu

TABLE OF CONTENTS

ACKNOWLEDGMENTS . . . iii
ACADEMIC ETHICS AND INTEGRITY STATEMENT . . . iv
ABSTRACT . . . v
ÖZET . . . vi
LIST OF FIGURES . . . x
LIST OF TABLES . . . xiv
LIST OF SYMBOLS . . . xvii
LIST OF ABBREVIATIONS . . . xviii
1. INTRODUCTION . . . 1
1.1 Overview of Ovarian Cancer . . . 1
1.1.1 Epidemiology and Risk Factors . . . 2
1.1.2 Diagnosis and Assessment . . . 3
1.1.2.1 Staging . . . 4
1.1.2.2 Grading . . . 5
1.1.2.3 Histological Subtypes . . . 5
1.1.3 Genetic Alterations in Ovarian Cancer . . . 6
1.1.3.1 Signaling Pathways . . . 6
1.1.3.2 Mutations . . . 8
1.1.3.3 Copy Number Variations . . . 9
1.1.3.4 DNA Methylation . . . 10
1.1.3.5 Protein Expression . . . 11
1.2 Survival Analysis . . . 12
1.2.1 Modeling Techniques in Survival Analysis . . . 15
1.2.1.1 Parametric Models . . . 16
1.2.1.2 Non-parametric Models . . . 17
1.2.1.3 Semi-parametric Models . . . 18
1.2.2 Deep Learning for Survival Analysis . . . 21
1.2.2.1 Continuous-Time Models . . . 21
1.2.2.2 Discrete-Time Models . . . 22

1.2.2.3 Evaluation of Survival Models 25
1.3 AI Studies in Ovarian Cancer Survival Prediction 26
2. MATERIALS AND METHODS 30
2.1 Overview of Datasets 30
2.1.1 TCGA Dataset 30
2.1.1.1 Histopathology Images 30
2.1.1.2 Clinical Data 30
2.1.1.3 Genomic Profiles 33
2.1.1.4 Data Categorization 34
2.1.2 Başkent Dataset 35
2.2 Feature Engineering 35
2.2.1 Image Feature Extraction 36
2.2.2 Tabular Data Processing 37
2.2.2.1 Statistical Feature Selection 37
2.2.2.2 Neural Network-based Feature Selection 39
2.3 Model Development and Training 42
2.3.1 Architectural Overview 42
2.3.1.1 Multi-Modal Fusion 43
2.3.2 Training and Evaluation 48
2.3.3 Benchmarking 49
3. RESULTS 50
3.1 Insights from Data 50
3.1.1 TCGA Dataset Description 50
3.1.1.1 Data Categories 53
3.1.2 Başkent Dataset Description 56
3.2 Feature Selection Outcomes 56
3.2.1 Statistical Methods 57
3.2.2 Neural Network Approach 58
3.3 Model Performance 60
3.3.1 Image Feature Extractors 60
3.3.2 Multi-Modal Fusion Results 61
3.3.3 Comparative Analysis 66

4. DISCUSSION 69
4.1 Comparison of Selected Genetic Features with Literature 69
4.1.1 Signaling Pathways 69
4.1.2 Mutations 71
4.1.3 Copy Number Variation 73
4.1.4 DNA Methylation 75
4.1.5 Protein Expressions 76
4.2 Comparison of Image Encoders 77
4.3 Efficacy of Fusion Techniques 78
4.4 Benchmarking Analysis 81
4.5 Limitations 83
5. CONCLUSION 86
APPENDIX A. Feature Selection 88
A.1 Statistical Methods 88
A.1.1 Analysis of the Clinical Features 91
A.1.1.1 Correlation 91
A.1.1.2 Univariate Analysis 92
A.1.1.3 Multivariate Analysis 93
A.2 Neural Network Approach 95
APPENDIX B. Additional Comparative Analysis 97
REFERENCES 98

LIST OF FIGURES

Figure 1.1 Illustration of Four Distinct Hazard Function Models in Survival Analysis. This figure presents a comparative visualization of four key hazard function models, each representing different dynamics in survival data, including Constant Hazard, Increasing and Decreasing Weibull, and Log-Normal models. 13

Figure 2.1 Overview of Analytical Processes. This figure delineates the sequential methodology applied to both tabular and image data, aimed at predicting survival outcomes in ovarian cancer patients. Feature selection for clinical and genetic data yields the most representative tabular data. Among three evaluated image encoders, HistoSSL was selected as the most effective for image data feature extraction. The extracted patch features were subsequently integrated with tabular data using various fusion techniques to compute patient-level discrete-time survival probabilities. The Kaplan-Meier plots, depicted in the figure, belong to the TCGA dataset and illustrate the survival probability estimates. 38

Figure 2.2 Neural Network Architectures for Processing Tabular Data. This figure depicts the neural network architecture consisting of multilayer perceptron (MLP) blocks, tailored to the number of features. Each block includes a fully-connected (FC) layer, batch normalization (BN), rectified linear unit (ReLU) activation, and a dropout layer with a 0.25 dropout rate. 40

Figure 2.3 OViTANet Architecture. Image features are extracted using the pretrained self-supervised learning (SSL) network, HistoSSL [1], following segmentation and patching. Tabular data is processed through a dense network with skip connections to generate an embedding vector for the tabular data. This research explores diverse multi-modal fusion strategies including elementary techniques, such as concatenation, adaptive learning, and multiplication, which are applied at various stages of the model–early, mid, and late. Notably, a mid-level cross-attention mechanism is introduced, where keys (K) and values (V) are concatenated from both image and tabular data vectors, while queries (Q) are derived exclusively from image data, facilitating enhanced focus during multi-head attention processes. Moreover, bilinear fusion is utilized as a sophisticated late-stage fusion method, aiming to capture more complex interactions between the modalities. After five transformation blocks that consists of multi-head attention and feed forward modules, a multi-layer perceptron (MLP) head, comprising two fully-connected (FC) layers, yields discrete-time survival predictions. 43

Figure 3.1 Exclusion Process and Dataset Splitting for Discovery and Test Sets. This figure illustrates the methodical exclusion and splitting process of the dataset showing the number of frozen and formalin-fixed paraffin-embedded (FFPE) slides in each set. 51

Figure 3.2 Distribution of Cases by Data Volume. This figure illustrates the allocation of cases across discovery and test sets for predicting overall (OS) and disease-free (DFS) survival, categorized into six data volumes: Large in blue, Medium-high in green, Medium-low in yellow, Small I in orange, Small II in red, and Small III in purple. Horizontally aligned bars indicate the case counts per category, with OS predictions featured as the top bar and DFS predictions as the lower bar within each data volume segment. Training and test sets are differentiated by color intensity, with training sets in deeper tones and test sets in lighter tones, showcasing the dataset composition for each prediction task. 55

Figure 3.3 Performance of Image Encoders on Test Datasets. The bar chart illustrates the average concordance index and the 95% confidence interval for predictions of overall survival (on the left) and disease-free survival (on the right) across the TCGA test set and Başkent dataset. 61

Figure 3.4 Heatmap of the Fusion Search Results for Large and Medium Data Categories. Test concordance indices are shown for both overall survival (on the left) and disease-free survival (on the right). Each row represents the tabular feature that were fused with the patch features using strategies given in the columns. 62

Figure 3.5 Heatmap of the Fusion Search Results for Small Data Categories. Test concordance indices are shown for both overall survival (on the left) and disease-free survival (on the right). Each row represents the tabular feature that were fused with the patch features using strategies given in the columns. 63

Figure A.1 Heatmap of the Correlation Matrix of the Clinical Features. Pearson's correlation coefficient values are shown in the figure for each pair of clinical features as well as the overall survival months and exitus status. 91

Figure A.2 Kaplan-Meier Survival Curves for Clinically Significant Variables. This figure presents four Kaplan-Meier curves, each representing the survival function $S(t)$ over time t for different clinical variables identified as significant in the log-rank test. Each graph displays the survival estimates for the two groups, illustrating the differences in survival probabilities over time. 93

Figure A.3 Evaluation of Feature Sets by Neural Network Training. This figure presents comparative bar plots for six distinct data types for both overall (OS) and disease-free (DFS) survival prediction. For each data type, mean and 95% confidence interval values derived from a 5-fold cross-validation process, augmented with 1000 bootstrapping iterations, are depicted. 96

LIST OF TABLES

Table 1.1 Survival and hazard functions for three commonly used distributions in parametric survival analysis. 16

Table 3.1 Clinical characteristics for censored and uncensored cases in overall survival prediction are shown, listing continuous variables as mean ± standard deviation and categorical variables by count and percentage. P-values from t-test and chi-square analysis compare discovery and test set distributions. 52

Table 3.2 Clinical characteristics for censored and uncensored cases in disease-free survival prediction are shown, listing continuous variables as mean ± standard deviation and categorical variables by count and percentage. P-values from t-test and chi-square analysis compare discovery and test set distributions. 54

Table 3.3 This table presents the average test concordance index across various fusion techniques for predicting overall survival in each data category. 64

Table 3.4 This table presents the average test concordance index across various fusion techniques for predicting disease-free survival in each data category. 65

Table 3.5 The table displays the 5-fold cross-validation results for overall survival prediction of the proposed model OViTANet and PORPOISE [2] with mean ± standard deviation of test concordance index. Image features were combined with the tabular data combinations using the fusion strategies on the table for OViTANet and bilinear fusion for PORPOISE models. 67

Table 3.6 The table displays the 5-fold cross-validation results for disease-free survival prediction of the proposed model OViTANet and PORPOISE [2] with mean ± standard deviation of test concordance index. Image features were combined with the tabular data combinations using the fusion strategies on the table for OViTANet and bilinear fusion for PORPOISE models. 68

Table A.1 The table displays the number of features retained after applying various feature selection methods and their combinations for OS prediction. The methods include variance threshold (VarThr), multi-collinearity reduction (Collin), log-rank test (LR), and Cox proportional hazards model with varying levels of regularization: low ($\text{CoxPH}_{\text{low}}$), intermediate ($\text{CoxPH}_{\text{int}}$), and high ($\text{CoxPH}_{\text{high}}$). Features chosen for each data category are highlighted in bold. 89

Table A.2 The table displays the number of features retained after applying various feature selection methods and their combinations for DFS prediction. The methods include variance threshold (VarThr), multi-collinearity reduction (Collin), log-rank test (LR), and Cox proportional hazards model with varying levels of regularization: low ($\text{CoxPH}_{\text{low}}$), intermediate ($\text{CoxPH}_{\text{int}}$), and high ($\text{CoxPH}_{\text{high}}$). Features chosen for each data category are highlighted in bold. 90

Table A.3 Log-rank test p-values for various clinical features are given for OS and DFS prediction. Significant p-values < 0.05 are bolded. 92

Table A.4 The outcomes of the multivariate feature selection using Cox's proportional hazards model with an elastic net penalty are displayed for Overall (OS) and Disease-free (DFS) Survival predictions. Features with zero coefficients are bolded for clarity across different α values, signifying their exclusion from the feature set. 94

Table B.1 The table displays the 5-fold cross-validation results for overall survival prediction of the proposed model OViTANet and PORPOISE [2] with mean ± standard deviation of test concordance index. Image features were combined with the tabular data combinations using early concatenation for OViTANet and bilinear fusion for PORPOISE models. 97

LIST OF SYMBOLS

t	Time
$h(t)$	Hazard function
$S(t)$	Survival function
$\hat{S}(t)$	Estimator of the survival function
$F(t)$	Cumulative distribution function of survival times
$f(t)$	Probability density function of survival times
X	Covariates in a multivariate survival model
$\widehat{HR}$	Estimated hazard ratio
$\overline{x}$	Mean of the sample
s	Standard deviation of the sample
n	Sample size
z	The z-score for the specified confidence level
$\odot$	Element-wise multiplication
$\otimes$	Kronecker Product
β	Covariates' coefficients
Δt	Change in time
μ	Mean of a population
σ	Standard deviation of a population

LIST OF ABBREVIATIONS

AJCC	American Joint Committee on Cancer
AUROC	Area Under the Receiver Operating Characteristic Curve
C-Index	Concordance Index
CI	Confidence Interval
CNV	Copy-Number Variation
COXPH	Cox's Proportional Hazards Model
DFS	Disease-Free Survival
DNAm	DNA Methylation
FFPE	Formalin-Fixed Paraffin-Embedded
H&E	Hematoxylin & Eosin
HR	Hazard Ratio
KM	Kaplan-Meier
MLP	Multi-Layer Perceptron
MHA	Multi-Head Attention
Mut	Mutation
mRNA-Seq	mRNA Sequencing
OS	Overall Survival
OViTANet	Ovarian Cancer Vision Transformer Aggregated Network
RPPA-Exp	Reverse-Phase Protein Array Expression
SOC	Serous Ovarian Cancer
TCGA	The Cancer Genome Atlas

1. INTRODUCTION

1.1 Overview of Ovarian Cancer

Ovarian cancer, characterized by its high mortality rate and substantial prevalence, remains a significant challenge in the field of oncology. This malignancy is influenced by a complex interplay of genetic predispositions and environmental factors, underscoring the critical need for thorough risk assessment. The accurate evaluation of ovarian cancer involves a multifaceted approach, encompassing staging, grading, and determination of histological subtypes. These diagnostic measures are crucial for formulating an effective treatment strategy and providing a prognosis [3].

Recent breakthroughs in molecular biology have profoundly expanded our understanding of the genetic and molecular underpinnings of ovarian cancer. This knowledge has opened the door to more personalized treatment approaches, aiming to target specific molecular alterations inherent to the tumor. Such advancements are especially pertinent given the disease's high mortality rate; they offer hope for improved therapeutic outcomes and patient survival.

Furthermore, the ability to accurately predict survival at the time of diagnosis is invaluable. It not only assists patients in setting realistic expectations regarding their disease trajectory but also enables clinicians to tailor treatments to individual patient profiles. This prognostic insight is particularly crucial in ovarian cancer, where early and precise predictions can significantly impact treatment decisions and, ultimately, patient quality of life. This chapter aims to delve into the complexities of ovarian cancer, exploring its risk factors, diagnostic procedures, molecular characteristics, and the pivotal role of survival prediction in managing this formidable disease.

1.1.1 Epidemiology and Risk Factors

Ovarian cancer, despite not being among the most common cancers, holds a disproportionately high fatality rate, ranking as the 5th leading cause of cancer-related deaths in the United States [4]. Its prevalence in Turkey further underscores its global impact, where it is the 7th most commonly diagnosed cancer with an incidence rate fluctuating between 6.9 and 7.3 per 100,000 cases. Notably, the median age of diagnosis is 63 years, indicating a higher vulnerability in the older population [3]. Advances in medical technology and treatment strategies have only moderately improved survival rates; the 5-year relative survival rate has gradually increased from 44.5% [95% Confidence Interval (CI): 43.3 - 45.8] to 51.2% [95% CI: 50.0 - 52.4] over nearly two decades [5].

The risk factors for ovarian cancer are multifaceted and include:

- Ovulation-related factors: The incessant ovulation theory suggests that each ovulation event can cause minor trauma to the ovarian epithelium, potentially leading to mutations due to oxidative stress from tissue repair [6]. Key factors include:
  - Early onset of menarche and late onset of menopause
  - Nulliparity, which approximately doubles the risk
  - Infertility
  - Polycystic ovary syndrome
- Age: The likelihood of developing ovarian cancer escalates with age. For women under 50, the risk increases by 2% annually, whereas it rises to as much as 11% for older women.
- Endometriosis: This condition is linked to rarer subtypes such as clear cell, endometrioid, and low-grade serous ovarian cancer, generally associated with a more favorable prognosis.
- Family History and Genetic Predisposition:

  - Breast Cancer gene 1 and 2 (BRCA1/BRCA2) Mutations: Individuals with these mutations face a cumulative risk of developing ovarian cancer by age 80 estimated at 44% for BRCA1 and 17% for BRCA2 mutations.
  - Lynch Syndrome: This genetic syndrome, characterized by mutations in repair genes such as MutL Homolog 1 (MLH1), MutS Homolog 2 (MSH2), MutS Homolog 6 (MSH6), Postmeiotic Segregation Increased 1 (PMS1), Postmeiotic Segregation Increased 2 (PMS2) is associated with an elevated risk of several cancers, including ovarian cancer.

- Lifestyle Factors:
  - Smoking: It is specifically correlated with an increased risk of mucinous ovarian cancer, with risk levels rising in proportion to the duration of smoking.
  - Obesity: It is related to both a heightened risk of developing ovarian cancer and increased mortality rates.
  - Dietary Influences: Dietary patterns also play a role, where high consumption of animal fats is linked to increased risk, whereas a high intake of soy products offers a protective effect.

1.1.2 Diagnosis and Assessment

In the clinical management of ovarian cancer, accurate diagnosis and assessment are pivotal for determining the most effective treatment strategy. This section delves into three critical aspects of this process: staging, grading, and histological subtypes. Each plays a unique role in understanding the extent and aggressiveness of the disease. Staging categorizes the cancer based on its spread within the body while grading evaluates the tumor's cellular makeup to ascertain how much it deviates from normal, healthy cells, providing insights into its likely growth rate and tendency to spread. Lastly, identifying the histological subtypes of ovarian cancer is crucial, as different types exhibit distinct behaviors and responses to treatment. This classification not only aids in prognosis but also in tailoring specific therapeutic approaches, enhancing

the effectiveness of the treatment plan. Together, these diagnostic and assessment tools form a comprehensive framework essential for guiding clinical decisions and optimizing patient outcomes in ovarian cancer management.

1.1.2.1 Staging. Staging is crucial for both treatment planning and predicting the disease outcome in ovarian cancer. Pathological staging is generally preferred due to its higher precision. However, in instances where immediate surgery is not feasible, clinical staging is utilized. Two commonly used staging systems are the International Federation of Gynecology and Obstetrics system and the American Joint Committee on Cancer (AJCC) TNM staging system, which are fundamentally aligned. These systems categorize ovarian cancer based on three primary criteria:

- The Extent of the **T**umor (T)
- The Spread to Lymph **N**odes (N)
- The Spread (**M**etastasis) to Other Organs or Organ Fluids (M)

Based on these criteria, ovarian cancer is classified into four stages:

- **Stage I:** Characterized by localized tumors confined to one or both ovaries or fallopian tubes.
- **Stage II:** Indicates pelvic extension, affecting the uterus or other pelvic organs, including the bladder, sigmoid colon, or rectum.
- **Stage III:** Represents more advanced tumors, marked by either lymph node metastases or the presence of primary peritoneal cancer.
- **Stage IV:** Denotes the presence of distant organ metastasis [7].

1.1.2.2 Grading. Tumor grading is an essential factor in assessing the progression of cancer. The AJCC classifies cancers into four grades based on tissue differentiation:

- Well-Differentiated (G1): Tumors exhibit a structure similar to normal tissue and tend to grow and spread at a slower rate.
- Moderately Differentiated (G2): These tumors have features between grades 1 and 3 and are somewhat similar to normal tissue.
- Poorly Differentiated (G3): Tumors appear abnormal and tend to grow and spread more quickly.
- Undifferentiated (G4): Tumors lack normal tissue structures and have an aggressive growth pattern.

Apart from this 4-tier system, there are other grading systems employing a 3-tier categorization–low (G1), intermediate (G2), and high (G3 or G4)–or a 2-tier categorization–low (G1) and high (G2, G3, or G4) grades. Notably, in serous ovarian cancer, low and high-grade tumors not only exhibit distinct histological features but are also believed to have divergent pathogenesis and molecular characteristics. However, the process of accurate tumor grading can be challenging and is highly subjective, depending largely on the pathologist's assessment. This subjectivity was highlighted in a study demonstrating only fair to moderate agreement between two pathologists in tumor grading [8].

1.1.2.3 Histological Subtypes. Ovarian cancer is categorized into four primary groups based on the cell of origin: epithelial, sex-cord stromal, germ cell, and mixed-cell types. Of these, epithelial ovarian cancer is the predominant type, comprising about 90% of all ovarian cancer cases. This category is further subdivided into five histological subtypes, each characterized by distinct microenvironmental, molecular, and clinical features.

The most prevalent and aggressive among these subtypes is high-grade serous ovarian cancer (SOC), representing approximately 70% of all epithelial ovarian cancer cases. The second most frequent subtype, low-grade SOC, accounts for around 10% of these cases. Notably, while low-grade SOC typically exhibits a less aggressive progression compared to high-grade SOC, it tends to be more resistant to treatment. Other less common subtypes include ovarian clear-cell carcinoma, endometrioid, and mucinous ovarian cancers [9].

1.1.3 Genetic Alterations in Ovarian Cancer

Ovarian cancer, a complex and heterogenous disease, exhibits a wide array of genetic variations that significantly influence its pathogenesis and progression. This section delves into the intricate web of pathway signaling, mutations, copy number variations (CNVs), DNA methylation, and protein expressions that underpin the molecular landscape of ovarian cancer. Pathway signaling disruptions, often triggered by genetic mutations, play a pivotal role in the onset and development of the disease, manipulating cellular processes in ways that promote cancer growth and resistance to treatment. CNVs contribute to oncogenesis by altering gene dosage, thus affecting gene expression levels and, consequently, cellular function. DNA methylation patterns, which regulate gene expression without altering the DNA sequence, are frequently aberrant in ovarian cancer, leading to the silencing of tumor suppressor genes or the activation of oncogenes. Lastly, changes in protein expressions, driven by genetic alterations, impact a wide range of cellular mechanisms, including cell cycle regulation, apoptosis, and metastasis. Together, these genetic and epigenetic variations offer critical insights into the molecular mechanisms driving ovarian cancer, presenting potential targets for therapeutic intervention and biomarkers for diagnosis and prognosis.

1.1.3.1 Signaling Pathways. In the context of ovarian cancer, a multitude of signaling pathways have been identified as excessively active, notably including the phosphatidylinositol 3-kinase (PI3K)/protein kinase B (Akt)/mammalian target of

rapamycin (mTOR), Janus kinase/signal transducers and activators of transcription (JAK/STAT), Src, lysophosphatidic acid (LPA), and nuclear factor κB (NF-κB) pathways. These pathways are intrinsically linked to the progression of aggressive forms of the disease and are characterized by poor prognostic outcomes, primarily due to elevated mutation frequencies and hyperactivation [10].

Specifically, the aberrant activation of the PI3K/Akt/mTOR pathway is implicated in the deregulation of cellular growth and survival mechanisms. An association has been established between heightened Akt signaling and reduced survival durations in patients with ovarian cancer. Moreover, mutations and disruptions in key tumor suppressor genes, such as retinoblastoma 1 (RB1), phosphatase and tensin homolog (PTEN), neurofibromin 1 (NF1) and RAD51B, have been identified, which contribute to a chemotherapy-resistant phenotype. The involvement of this pathway extends to the preservation of cancer stemness, which further exacerbates drug resistance and enhances metastatic potential [11]. Remarkably, mutations in PIK3CA exhibit a higher prevalence in less common ovarian cancer subtypes. Prior investigations have highlighted the significant occurrence of activating PIK3CA mutations in clear cell ovarian carcinoma and endometrioid ovarian cancer, particularly in cases linked to endometriosis [12].

Interleukin-6 is predominantly overexpressed in ovarian cancers, instigating autocrine activation of its receptor. This activation triggers the JAK2, leading to the phosphorylation and subsequent nuclear translocation of STAT3. The activation of STAT3 promotes gene expression that facilitates cellular proliferation, inhibits apoptosis, and stimulates angiogenesis. Over 70% of ovarian cancers exhibit nuclear localization of phosphorylated STAT3, a phenomenon correlated with diminished overall survival. Furthermore, activated STAT3 coordinates with Src to enhance cellular motility through its integration into focal adhesion complexes.

LPA, synthesized by the enzyme autotaxin, plays a pivotal role in the malignant transformation of ovarian surface epithelial cells. The upregulation of G protein-coupled LPA receptors, specifically LPAR2 and LPAR3, is noted during this transfor-

mation process. LPAR3, in particular, is responsive to LPAs with unsaturated fatty acyl chains produced by ovarian cancers.

The NF-κB transcription factor is found to be constitutively active in a significant fraction of ovarian cancers, a condition facilitated by signals originating from various cytokines and growth factors. The consequent activation of NF-κB leads to the upregulation of genes associated with anti-apoptotic functions, antioxidant proteins, cytokines regulating growth, and angiogenic factors [10].

1.1.3.2 Mutations. In the realm of high-grade SOC, a notable feature is the impairment in DNA repair mechanisms, coupled with prevalent CNVs. These characteristics render high-grade SOC initially responsive to platinum-based chemotherapy, albeit with a subsequent evolution towards therapeutic resistance [13]. The comprehensive evaluation by The Cancer Genome Atlas (TCGA) Research Network identifies mutations in tumor protein p53 gene (TP53) (present in 96% of cases), BRCA1 and BRCA2 (accounting for 22%) as predominantly observed alterations. Additionally, recurrent mutations are observed in several crucial genes, including RB1, NF1, FAT Atypical Cadherin 3 (FAT3), CUB and Sushi Multiple Domains 3 (CSMD3), Gamma-Aminobutyric Acid Type A Receptor Alpha6 Subunit (GABRA6), and Cyclin Dependent Kinase 12 (CDK12), with the latter implicated in the regulation of RNA splicing [14]. Moreover, the specific overexpression of various genes, such as ATP Binding Cassette Subfamily 1 (ABC1), ATP Binding Cassette Subfamily 2 (ABC2), and Glutathione Synthetase 1 (GSH1), is correlated with disease advancement and resistance to treatment. The induction of mesenchymal markers, including SNAIL, SLUG, and TWIST, through epithelial-to-mesenchymal transition, is associated with the development of chemotherapy resistance.

Conversely, low-grade SOC exhibit slower growth kinetics and a higher incidence of mutations in Kirsten rat sarcoma viral oncogene (KRAS), V-Raf Murine Sarcoma Viral Oncogene Homolog B (BRAF), and v-erb-b2 avian erythroblastic leukemia viral oncogene homolog 2 (ERBB2), typically devoid of TP53 mutations. Each mutation

serves as a hallmark of the activation within the mitogen-activated protein kinase (MAPK) pathways. Elevated MAPK pathway activity in low-grade SOC relative to high-grade SOC counterparts is linked with increased sensitivity to paclitaxel and an enhanced 5-year survival prognosis. In addition to harboring functional TP53, these tumors are characterized by genomic stability, with fewer rearrangements, mutations, and a lower degree of tumor heterogeneity. Nonetheless, the efficacy of front-line chemotherapy is diminished due to more proficient DNA repair capabilities compared to high-grade SOC. The regulatory role of the MAPK pathway in cell cycle control is posited to be a critical factor underlying the chemoresistance observed in LGS tumors [13].

A study involving high-grade SOC biobanks in Australia and the United States identified genetic distinctions between long-term survivors (more than 10 years) and moderate/short-term survivors. Seven features were associated with OS in univariable Cox regression models. These include DNA repair gene alterations with a hazard ratio (HR) of 0.39, activated CD4 memory T cells (HR: 0.47), BRCA2-type homologous recombination deficiency (HR: 0.48), proliferating cell nuclear antigen (PCNA) expression (HR: 0.51), plasma cells (HR: 0.60), neoantigen count (HR: 0.71), and residual disease (HR: 2.38). A multivariable model showed four features statistically linked to OS: homologous recombination deficiency type, PCNA expression, plasma cells, and residual disease. The study found a higher rate of combined germline and somatic homologous recombination alterations in long-term and moderate-term survivors compared to short-term survivors, involving mutations in several genes like BRCA1, BRCA2, and PTEN. CCNE1 gene amplification, typically a poor prognostic marker, was more prevalent in short-term survivors but also appeared in some long-term survivor tumors. Long-term survivors had a higher proportion of tumors with multiple DNA repair gene alterations. These patients exhibited longer survival compared to those with fewer or no DNA repair gene alterations [15].

1.1.3.3 Copy Number Variations. Genomic disarray characterizes high-grade SOC, with frequent mutations and promoter methylation in DNA repair genes, potentially explaining the high prevalence of somatic CNV. In fact, the prevalence of

oncogene amplifications in ovarian cancer surpasses that of activating mutations [10]. TCGA Research Network identifies recurrent focal somatic CNVs including amplifications in cyclin E1 (CCNE1), MDS1 and EVI1 complex locus protein EVI1 (MECOM) and MYC, each amplified in over 20% of tumors [14]. Importantly, the amplification of CCNE1 is linked to an adverse prognosis and resistance to platinum-based chemotherapy in high-grade SOC [13]. Furthermore, deletions in the tumor suppressor genes PTEN, RB1, and NF1 have been observed [14]. Specifically, the loss of PTEN expression in tumor-specific cells serves as a predictor of unfavorable patient survival outcomes in ovarian cancer [13].

1.1.3.4 DNA Methylation. Alterations in DNA methylation, which result in chromosome instability and modifications in gene expression, are strongly associated with the process of carcinogenesis [16]. The analysis conducted by the TCGA Research Network identified the epigenetic silencing of 168 genes in high-grade SOC compared to controls from the fallopian tube, with a notable instance being the hypermethylation in the promoter region of BRCA1. The clustering of DNA methylation patterns revealed four subtypes that were significantly associated with variables such as age, events of BRCA inactivation, and survival outcomes, though these associations were found to have modest stability. A transcriptional signature comprising 193 genes predictive of OS was discovered, with Kaplan-Meier survival analysis validating its significant association with survival across various validation datasets [14].

Beyond BRCA1, Ras Association Domain Family Member 1 (RASSF1A) was identified as another tumor suppressor gene undergoing epigenetic deregulation, with its alteration frequency varying between 10% and 49%. Additionally, Opioid Binding Protein/Cell Adhesion Molecule Like (OPCML), present in up to 83% of ovarian tumors, and p16INK4a, frequently methylated in ovarian cancer but rarely in control samples, were highlighted as tumor suppressor genes frequently methylated at their promoters in ovarian cancer [16].

The focus on hypomethylation within ovarian cancer studies has increased in

recent years, despite being less studied than hypermethylation historically. A study from 2009 pointed out that hypomethylation is the predominant methylation change in ovarian cancer. In this study, around 27,000 CpG sites were screened in 113 ovarian cancer cases and 148 healthy controls, leading to the identification of 2,714 cancer-related CpG sites, 56% of which were hypomethylated. Remarkably, among the 50 CpG sites with the highest correlation to cancer, 87% exhibited hypomethylation [17].

Over the past two decades, research has identified a plethora of candidate genes with hypo- or hypermethylation profiles linked to chemoresistance in ovarian cancer. This includes the hypermethylation of genes such as BRCA1, Cadherin 2 (CDH2), c-FOS, Dishevelled-Binding Antagonist of Beta-Catenin 1 (DACT1), Integrin Subunit Alpha V (ITFAV), Methylation-Controlled J Protein (MCJ), Mesoderm Specific Transcript (MEST), MLH1, MSH2, Alpha-N-Acetylgalactosaminidase (NAGA), Neogenin 1 (NEO1), PTEN, RASSF1A, Regulator of G Protein Signaling 10 (RGS10), Secreted Frizzled-Related Proteins 1-5 (SFRP1-5), Tribbles Pseudokinase 2 (TRIB2), and the hypomethylation of ATP Binding Cassette Subfamily B Member 1 (ABCB1), ATP Binding Cassette Subfamily G Member 2 (ABCG2), Claudin 4 (CLDN4), Serpin Family E Member 1 (SERPINE1), Solute Carrier Family 6 Member 14 (SLC6A14), Transmembrane Protein 88 (TMEM88), Vimentin (VIM) [18].

1.1.3.5 Protein Expression. In a comprehensive study including 239 epithelial ovarian cancer patients, 4447 high-quality proteins were identified, among which 295 were significantly upregulated and 927 were downregulated. The analysis revealed a general trend of protein downregulation in tumor tissues, with these proteins significantly enriched in biological processes such as cell death, DNA repair/damage, development, and immune response. Conversely, upregulated proteins were associated with a limited range of biological processes but were notably overrepresented in key KEGG pathways including DNA replication, cell cycle, and HIF-1 signaling pathway, pointing to their role in tumor cell proliferation and metastasis. The gene set enrichment analysis further highlighted the disparity in cancer hallmark pathways between upregulated and downregulated proteins, suggesting potential mechanisms of tumor progression.

Moreover, certain proteins like Cyclin-Dependent Kinase 4 (CDK4), Cyclin-Dependent Kinase Inhibitor 1B (CDKN1B), and Collagen Type I Alpha 2 Chain (COL1A2) were identified as high-risk factors for mortality in epithelial ovarian cancer , with the expression of extracellular matrix receptor members like COL1A1, COL1A2, and COL6A3 correlating with recurrence-free survival and showcasing significantly lower expression in tumor samples. Additionally, MMP7 emerged as a promising therapeutic target in SOC, validated by its high expression and prognostic significance in the external validation dataset [19].

1.2 Survival Analysis

Survival analysis, also known as time-to-event analysis, is a branch of statistics that deals with the prediction of time until the occurrence of an event of interest. The key components in survival analysis are time, event, and censoring.

- **Time:** The duration until the occurrence of an event or the end of the study period.
- **Event:** The specific outcome or occurrence that the study is designed to predict, such as death, relapse, or failure of a system.
- **Censoring:** Occurs when the event of interest has not been observed for a subject during the study period. This can happen due to loss of follow-up, withdrawal from the study, or the study ending before the event occurs.

In terms of censoring types, right-censoring occurs when the actual survival time is at least as long as the observed survival time. Conversely, left-censoring happens when the true survival time is shorter than or equal to the observed survival time. In the context of ovarian cancer patient survival analysis, right-censoring is prevalent, signified by the availability of the last follow-up date for patients whose events haven't been observed.

Hazards Function: The concept of hazard functions and survival functions is central to survival analysis. The hazard function, denoted as $h(t)$, refers to the instantaneous risk or chance of an event occurring at a particular time t, considering that the event has not occurred until that point. This function quantifies how the risk of the event changes over time. Mathematically, it is expressed as:

$$h(t) = \lim_{\Delta t \to 0} \frac{P(t \leq T < t + \Delta t | T \geq t)}{\Delta t} \tag{1.1}$$

where T represents the time until the event occurs. The numerator in this equation calculates the probability of the event occurring in the interval from t to $t + \Delta t$, given survival until time t. As Δt approaches zero, this gives the instantaneous hazard at time t.

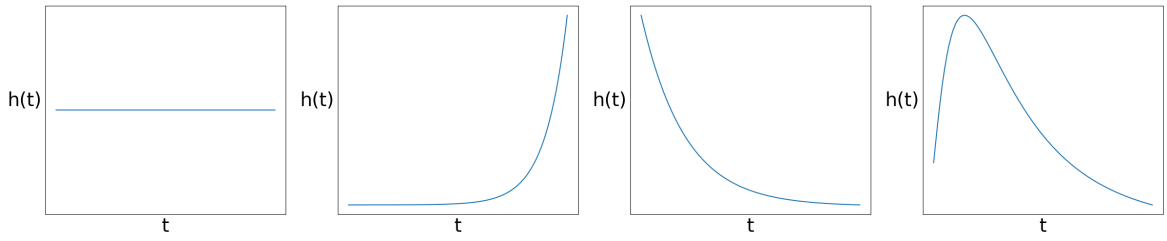


Figure 1.1 Illustration of Four Distinct Hazard Function Models in Survival Analysis. This figure presents a comparative visualization of four key hazard function models, each representing different dynamics in survival data, including Constant Hazard, Increasing and Decreasing Weibull, and Log-Normal models.

In the field of survival analysis, four distinct survival models are recognized, each characterized by the unique behavior of the hazard function over time, as illustrated in Figure 1.1. The first model, known as the *exponential survival model*, is identified by a constant hazard function. This implies a consistent risk over time, making it a simplistic yet effective model under certain conditions. The next two models, the *increasing and decreasing Weibull models*, represent contrasting scenarios. The increasing Weibull model is applicable when the hazard grows over time, a situation commonly seen in progressive diseases. Conversely, the decreasing Weibull model applies to scenarios where the risk diminishes over time, akin to the healing process in various medical conditions. Finally, the *log-normal survival model* is distinguished by a hazard function that initially increases and subsequently decreases. This pattern is often observed in

diseases such as tuberculosis, where the risk of adverse outcomes is higher in the early stages of the disease and decreases as the disease progresses. These models provide a framework for understanding and predicting survival times in various contexts, each tailored to the specific nature of the hazard function associated with different conditions and diseases.

Survival Function: The survival function, denoted as $S(t)$, is defined as the probability of an individual surviving beyond a specific time t. It essentially measures the likelihood that the time to event exceeds t. The survival function is complementary to the cumulative distribution function of the survival times, $F(t)$, and is mathematically described as:

$$S(t) = P(T > t) = 1 - F(t) \tag{1.2}$$

The survival function, $S(t)$, and the hazard function, $h(t)$, are fundamentally interlinked in survival analysis. While $S(t)$ represents the probability of an individual surviving beyond a specific time t, capturing the likelihood that the time to event exceeds t, the hazard function $h(t)$ denotes the instantaneous risk of the event occurring at time t.

The survival function is often expressed in terms of the hazard function. Mathematically, it is described by the equation:

$$S(t) = e^{\left(-\int_0^t h(u)\,du\right)} \tag{1.3}$$

This formula indicates that the survival probability up to time t is the exponential of the negative integral of the hazard function over time from 0 to t. The integral of $h(u)$ from 0 to t gives the cumulative hazard up to time t, and taking the negative exponential of this value yields the survival probability.

Conversely, the hazard function can be derived from the survival function. The instantaneous hazard at time t, $h(t)$, can be understood as the rate of decline of the

survival function at time t, relative to the survival probability at that time. This relationship can be mathematically represented as:

$$h(t) = -\frac{d}{dt} \ln S(t) \tag{1.4}$$

where $\ln S(t)$ is the natural logarithm of the survival function. The derivative of $\ln S(t)$ with respect to time t gives the rate at which the log survival probability is changing at that moment, reflecting the instantaneous hazard [20].

1.2.1 Modeling Techniques in Survival Analysis

In survival analysis, two principal categories of models are typically considered by researchers: non-parametric and parametric models. Non-parametric models, known for their flexibility, are preferred in scenarios where fewer assumptions about the data distribution shape are desirable. On the other hand, parametric models offer greater efficiency in data analysis due to their reliance on predefined distribution shapes. Additionally, semi-parametric models have emerged as a significant approach in survival analysis, combining elements of both parametric and non-parametric methodologies. These models, such as the Cox Proportional Hazards (CoxPH) model, offer a balance between the flexibility of non-parametric models and the specific functional form of parametric models. They allow for the inclusion of covariates without assuming a fixed baseline hazard function, making them particularly useful for more complex analyses where the relationships between survival time and multiple predictors are considered. In the context of medical literature, the application of survival analysis typically follows a phased approach. Initially, non-parametric methods like the Kaplan-Meier estimator are employed to discern the overall trend of survival probabilities. This preliminary analysis provides a basic understanding of the survival patterns without delving into the effects of different variables. Subsequently, researchers often employ the Cox Proportional Hazards model for a more detailed investigation. This can be in the form of a univariable analysis, focusing on the relationship between survival time and a single predictor, or a multivariable approach, where multiple factors are considered simultaneously. This progression allows for an initial descriptive analysis followed

by a more complex exploration of the effects of various covariates on survival. However, if there is a strong understanding of the risk distribution and a specific interest in estimating survival times, parametric survival analysis may be preferred [21].

1.2.1.1 Parametric Models. A parametric survival model assumes that the survival times follow a specific known distribution. This approach is characterized by defining a probability density function $f(t)$ for survival time, based on certain unknown parameters. Commonly used distributions in parametric models include the exponential, Weibull, and log-logistic distributions, as detailed in Table 1.1. Each distribution is defined by its unique parameters: the exponential model has a single parameter and assumes a constant hazard rate, while the Weibull and log-logistic models are two-parameter models with more complex hazard functions. The exponential model becomes a special case of the Weibull model when the shape parameter, p, equals one.

Table 1.1
Survival and hazard functions for three commonly used distributions in parametric survival analysis.

Distribution	$S(t)$	$h(t)$
Exponential	$e^{-\lambda t}$	λ
Weibull	$e^{-\lambda t^p}$	$\lambda p t^{p-1}$
Log-logistic	$\frac{1}{1+\lambda t^p}$	$\frac{\lambda p t^{p-1}}{1+\lambda t^p}$

Parametric models operate on the assumption that survival times adhere to a specific, pre-defined distribution. This presumption, while useful in theoretical scenarios or controlled studies, often does not hold true in real-world, real-time data environments. The diversity and unpredictability inherent in real-life data sets, especially those collected in real-time, can lead to mismatches between the assumed and actual distributions of survival times. This discrepancy can result in less accurate or reliable model predictions. Consequently, in practical applications involving real-time data, such as dynamic patient monitoring in medical settings or real-time system failure analysis, researchers often lean towards non-parametric or semi-parametric models. These models offer greater flexibility and adaptability, attributes crucial for accurately

capturing the complexities of real-time data without the need for predefined distributional assumptions [22].

1.2.1.2 Non-parametric Models. The Kaplan-Meier (KM) estimator is a fundamental non-parametric method used for estimating survival probabilities at different time points in survival analysis. It is particularly adept at handling right-censored data, a common scenario in survival studies. It calculates the survival probability at a specific time $t_{(f)}$ using the product of conditional survival probabilities up to that time. The formula is as follows:

$$\hat{S}(t) = \prod_{i:t_i<=t} \left(1 - \frac{d(t_i)}{n(t_i)}\right) \tag{1.5}$$

Here, $\hat{S}(t)$ represents the estimator of the survival function, $d(t_i)$ is the number of events at each time point t_i, and $n(t_i)$ denotes the number of individuals at risk of the event just before time t_i. This formula effectively provides the probability of survival by multiplying the conditional probabilities of surviving past each observed failure time. It's a stepwise method that accumulates survival probability across different time points, offering a detailed view of the survival experience of the study population [23].

The Kaplan-Meier estimator, like other non-parametric survival models, excels in accurately estimating survival probabilities from observed data. This approach allows for a detailed assessment of survival times, effectively capturing the probability of survival at each time point through the multiplication of conditional probabilities. However, a notable limitation of the Kaplan-Meier estimator, and indeed all non-parametric survival models, is their inability to extrapolate these insights to predict future events or outcomes in different datasets. While adept at estimating survival probabilities based on existing data, they lack the predictive modeling capabilities often required for forecasting or planning purposes.

Despite this, the utility of non-parametric methods extends significantly into

analytical domains, particularly in understanding the characteristics and dynamics within survival data. A prime example of this is the log-rank test, a robust non-parametric test based on the chi-square statistic. Predominantly used for comparing survival distributions between two distinct groups, the log-rank test operates on the principle of contrasting hazard functions at each observed event time. It achieves this by calculating and then summing the differences between the observed and expected number of events in each group at every event time. Formally, under the null hypothesis $H_0 : S_1(t) = S_0(t)$, indicating no difference in survival distributions between the two groups, the test statistic Z is calculated as:

$$Z = \frac{\sum_{j=1}^{k}(O_j - E_j)}{\sqrt{\sum_{j=1}^{k} V_j}} \sim N(0,1) \text{ under } H_0 \tag{1.6}$$

In this formula, O_j represents the observed number of events, E_j denotes the expected number of events, and V_j is the variance of the observed number of events at each event time j. The resultant Z statistic is then used to compute a p-value from chi-square distribution tables, facilitating a robust statistical assessment of survival differences between groups [24],[25].

1.2.1.3 Semi-parametric Models. CoxPH model stands as a fundamental semi-parametric approach in survival analysis. Unlike parametric models, the CoxPH model does not require the specification of the underlying survival time distribution, making it more flexible in handling various types of survival data. It focuses on estimating the hazard ratio, allowing researchers to evaluate the effect of different covariates on survival times. The model assumes that these covariates multiplicatively affect the hazard rate and that the effect remains constant over time - an assumption known as proportional hazards. The CoxPH model's formulation is:

$$h(t, X) = h_0(t)e^{\sum_{i=1}^{p} \beta_i X_i} \tag{1.7}$$

Where in this equation:

- $h(t, X)$ is the hazard function at time t given the covariates X.
- $h_0(t)$ represents the baseline hazard function, which is the hazard function when all covariates X_i are equal to zero.
- The exponential term $e^{\sum_{i=1}^{p} \beta_i X_i}$ reflects the effect of p covariates X_i on the hazard, where each β_i is the coefficient corresponding to the i-th covariate X_i.

One of the revolutionary aspects of the CoxPH model is its treatment of the baseline hazard function. It does not require the explicit specification of $h_0(t)$. This approach contrasts with parametric models, where a specific mathematical form of the hazard function must be assumed. The CoxPH model's flexibility allows it to adapt to various underlying hazard shapes, making it broadly applicable in diverse situations.

The estimation of the model's parameters, particularly the β_i coefficients, is achieved through maximum likelihood estimation. However, due to the unspecified baseline hazard, the model uses a partial likelihood function, which is a modification of the standard likelihood function used in typical maximum likelihood estimation. The partial likelihood for the CoxPH model is expressed as:

$$L(\beta) = \prod_{i:\delta_i=1} \left(\frac{e^{\sum_{j=1}^{p} \beta_j X_{ij}}}{\sum_{l \in R(t_i)} e^{\sum_{j=1}^{p} \beta_j X_{lj}}} \right) \tag{1.8}$$

In this formula, the product is over all individuals i for whom the event of interest has occurred ($\delta_i = 1$). The risk set $R(t_i)$ comprises individuals who are at risk of experiencing the event at time t_i. The partial likelihood contrasts the covariate effects for those who experienced the event at each time t_i with those at risk at the same time, effectively isolating the covariate effects from the baseline hazard.

Through this formulation, the CoxPH model efficiently provides estimates for the impact of covariates on survival, while remaining agnostic about the underlying baseline hazard. This characteristic renders the CoxPH model a robust and versatile tool in survival analysis, capable of providing insightful interpretations in a wide range

of scenarios where the exact hazard function is not known or is difficult to specify.

The hazard ratio (HR) is a key concept in survival analysis, particularly in the context of the CoxPH model. It quantifies the relative risk of the event occurring (such as failure or death) between two groups at any specific time point, given the covariates in the model. Mathematically, the hazard ratio between two groups can be expressed using the hazard functions for these groups. If $h_1(t, X)$ and $h_2(t, X)$ are the hazard functions for two groups with covariate sets X_1 and X_2, respectively, then the hazard ratio is defined as:

$$\widehat{HR} = \frac{\hat{h}_1(t, X)}{\hat{h}_2(t, X)} \tag{1.9}$$

Using the Cox model formulation, this becomes:

$$\widehat{HR} = \frac{\hat{h}_0(t) e^{\sum_{i=1}^{p} \beta_i X_{1i}}}{\hat{h}_0(t) e^{\sum_{i=1}^{p} \beta_i X_{2i}}} \tag{1.10}$$

Simplifying this, since $\hat{h}_0(t)$ cancels out, we get:

$$\widehat{HR} = e^{\sum_{i=1}^{p} \beta_i (X_{1i} - X_{2i})} \tag{1.11}$$

The hazard ratio is a measure of the effect size. An HR of 1 implies no difference in risk between the two groups, an HR greater than 1 indicates a higher risk in the first group, and an HR less than 1 suggests a lower risk in the first group compared to the second.

The concept of proportional hazards assumes that the hazard ratios between groups are constant over time. This means that while the absolute risk (hazard) may change, the relative risk (ratio of hazards) between groups remains constant throughout the study period. This assumption allows for the simplified expression of the HR without explicitly needing the baseline hazard function, $h_0(t)$ [26].

1.2.2 Deep Learning for Survival Analysis

Deep learning, with its advanced computational power and ability to handle large and complex datasets, offers significant advancements in predicting and understanding time-to-event data. This exploration is particularly focused on two distinct approaches: continuous-time and discrete-time survival models. Continuous-time survival models represent a category where the models are grounded in the framework of Cox's partial likelihood. These models maintain the continuous nature of time, capturing the instantaneous risk of an event at any given time point. They leverage the strengths of deep learning to enhance the Cox model, handling complex, high-dimensional data with intricate relationships between covariates and survival times. Conversely, discrete-time survival models represent a different approach, wherein the survival time is categorized into distinct intervals. These models typically involve classifying the probability of an event occurring within specified time periods. This approach suits scenarios where survival times are naturally discretized or when simplification of the survival time into intervals is beneficial for analysis.

1.2.2.1 Continuous-Time Models. The first notable example is the work of Faraggi and Simon, who pioneered the integration of neural networks into survival analysis. They introduced a novel approach for modeling censored survival data, utilizing the input-output relationship of a simple feed-forward neural network. This formed the basis for a non-linear proportional hazards model [27].

However, subsequent studies exploring neural networks' capabilities in risk pre-

diction have shown mixed results. Various extensions of the Faraggi-Simon network were applied, but they often failed to demonstrate superiority over the traditional linear Cox model. It was observed that the performance of neural networks varied significantly depending on the dataset, suggesting that their effectiveness might be context-dependent [28],[29],[30].

Another notable contribution came from Katzman et al. with the introduction of DeepSurv, a deep learning approach applying modern techniques to the Cox proportional hazards loss function. DeepSurv utilized a configurable feed-forward deep neural network, where the input comprised baseline data, and the network propagated these inputs through multiple hidden layers with specific weights θ. The network's final layer, consisting of a single node, performed a linear combination of the hidden features to predict the log-risk function. Their findings indicated that these novel networks could outperform classical Cox models in terms of the C-index [31].

Following DeepSurv, there has been a surge in research extending this model. Kvamme et al., for instance, proposed an alternative loss function that effectively handles both proportional and non-proportional hazards scenarios, thereby extending the Cox model's applicability.[32] Other significant works include SurvivalNet by Yousefi et al., which integrates proportional Cox models with neural networks and Bayesian optimization for hyperparameter tuning [33]. Zhu et al. further expanded the Cox methodology to image data by replacing DeepSurv's multi-layer perceptron (MLP) with a convolutional neural network [34].

1.2.2.2 Discrete-Time Models. In survival analysis, continuous-time models are frequently utilized. Nonetheless, the integration of neural networks, as parametric models, with survival analysis presents a compelling case for discrete-time models, which are also parametric. The alignment of discrete-time models with neural network architectures offers a promising avenue for advancing methods in time-to-event prediction [35].

A significant advancement in the domain of survival analysis was made by Lee et al., who innovatively applied modern neural networks to model the discrete-time likelihood for right-censored data. Their methodology, referred to as DeepHit, utilizes a neural network to define the probability mass function of the survival distribution, marking a notable development in this field [36]. Building on this, Gensheimer and Narasimhan introduced an approach where the discrete-time hazard rate was parameterized using a neural network, presenting a different perspective in the application of neural networks to survival analysis [37].

Further exploration in this area, encompassing both simulated and real-world data, was conducted to compare these methodologies. This study revealed that the Logistic-Hazard method, as proposed by Gensheimer and Narasimhan, tends to outperform the probability mass function parameterization strategy proposed by Lee et al. in several key aspects. Specifically, the Logistic-Hazard method demonstrated superior performance in discrimination and calibration of survival predictions, illustrating the potential effectiveness of this approach in survival analysis [35].

In discrete-time survival analysis the negative log-likelihood loss function is a critical component, especially in the context of right-censored data. This function is vital for estimating the likelihood of survival probabilities across defined time intervals, taking into account both uncensored and censored data scenarios.

For the set of time intervals $[t_1, t_2, ..., t_n]$, the conditional hazard probability h_j is defined as the probability that an individual experiences an event in interval j, given that they have survived up to the beginning of this interval. The probability that an individual survives up to and including interval j is represented by S_j, formulated as:

$$S_j = \prod_{i=1}^{j}(1 - h_i) \tag{1.12}$$

Here, $1 - h_i$ represents the survival probability in each interval up to j.

For individuals experiencing an event (uncensored) during interval j, the like-

lihood includes the probability of surviving through all previous intervals and then failing in interval j. This likelihood and its corresponding log-likelihood are expressed as:

$$\text{lik} = h_j \prod_{i=1}^{j-1} (1 - h_i) \tag{1.13}$$

$$\text{loglik} = \ln(h_j) + \sum_{i=1}^{j-1} \ln(1 - h_i) \tag{1.14}$$

In cases of censored data, where the censoring time t_c falls within a certain interval, the likelihood is the probability of surviving through all intervals up to the censoring point. For censoring occurring between intervals $j-1$ and j, this is given by:

$$\text{lik} = \prod_{i=1}^{j-1} (1 - h_i) \tag{1.15}$$

$$\text{loglik} = \sum_{i=1}^{j-1} \ln(1 - h_i) \tag{1.16}$$

Gensheimer and Narasimhan's deep learning adaptation of this function utilizes two vectors: surv_s and surv_f. The vector surv_s indicates the intervals through which an individual has survived, while surv_f indicates the interval of failure, if it occurred. The neural network outputs a vector $\text{surv}_{\text{pred}}$, representing the predicted conditional survival probabilities for each interval. The log-likelihood, crucial for optimizing the neural network, is formulated as:

$$\text{loglik} = \sum_{i=1}^{n} \left(\ln(1 + \text{surv}_s(i)(\text{surv}_{\text{pred}}(i) - 1)) + \ln(1 - \text{surv}_f(i)\text{surv}_{\text{pred}}(i))\right) \tag{1.17}$$

This equation effectively combines the survival and failure probabilities, adjusting the model's predictions to align with observed survival times and events, thereby optimizing the survival predictions in a discrete-time framework [37].

1.2.2.3 Evaluation of Survival Models. In the context of survival analysis, while traditional regression metrics like mean squared error or mean absolute error can be employed to assess the accuracy of risk prediction models, their application is somewhat limited. To address the unique challenges posed by survival data, particularly the impact of censoring, more specialized metrics have been developed. The concordance index (c-index) and the Brier score are prime examples of such metrics. The c-index is instrumental in evaluating a model's discriminative power, determining how well the predicted risk scores align with the observed event times. The Brier score, on the other hand, provides a comprehensive measure of a model's calibration, comparing the predicted probabilities of event occurrence at specific times against the actual observed frequencies. It also aids in assessing the model's ability to correctly rank the order of events, offering a more nuanced understanding of its predictive capabilities. These specialized metrics are thus integral to the thorough evaluation of survival models, ensuring that the nuances of censoring and the time-to-event nature of the data are appropriately accounted for.

C-Index The c-index stands as the most commonly used metric for evaluating the performance of survival models. It serves as a measure of the rank correlation between the predicted risk scores, denoted as $\hat{f}$, and the observed survival times, t. The c-index is defined by the proportion of concordant pairs relative to the total number of comparable pairs in the data.

A pair of samples, i and j, is considered comparable if the sample with the shorter observed survival time experienced an event. Formally, this is the case if $t_j > t_i$ and $\delta_i = 1$, where δ_i is a binary event indicator signifying whether an event occurred for sample i. Further, a comparable pair is defined as concordant when the survival model estimates a higher risk for the subject with the shorter survival time. In mathematical terms, a pair (i, j) is concordant if $\hat{f}_i > \hat{f}_j$ and $t_j > t_i$. Conversely, the pair is considered discordant if this condition is not met. The c-index thus encapsulates the model's ability to correctly rank pairs of subjects in terms of their risk scores and survival times, offering a valuable tool for assessing the predictive accuracy of survival models [38].

Brier Score The concordance index, often used in survival analysis, mainly assesses how well a model can rank predicted risk scores. However, it is limited in that it doesn't measure the model's accuracy in predicting the actual likelihood of events–its calibration. For this purpose, the Brier score is more suitable. It compares the model's predicted probability of an event occurring at a given time with the actual occurrence rate. A model is considered well-calibrated when its predictions closely match the observed event frequencies. For instance, if a model predicts a 80% risk of an event happening at a specific time, this prediction should be consistent with a 80% occurrence rate in the observed data. Beyond calibration, the Brier score also evaluates the model's discriminative power, particularly its effectiveness in correctly sequencing the occurrence of events based on their predicted risks.

The time-dependent Brier score extends the concept of mean squared error to accommodate right-censored data. Given a time point t, the time-dependent Brier score is defined as follows:

$$BS^c(t) = \frac{1}{n} \sum \left(I(y_i \leq t \wedge \delta_i = 1) \left[\frac{(0 - \hat{\pi}(t|x_i))^2}{\hat{G}(y_i)} \right] + I(y_i > t) \left[\frac{(1 - \hat{\pi}(t|x_i))^2}{\hat{G}(t)} \right] \right) \tag{1.18}$$

where $\hat{\pi}(t|x)$ denotes the model's predicted probability of remaining event-free up to time t for a given feature vector x and $\frac{1}{\hat{G}(t)}$ represents the inverse probability of censoring weight. The time-dependent Brier score is pertinent only for models capable of estimating a survival function, offering a comprehensive metric that encompasses both calibration and discrimination [39].

1.3 AI Studies in Ovarian Cancer Survival Prediction

In recent years, deep learning models have gained significant attention in the medical research, particularly in predicting survival outcomes from histopathology data

of cancer patients. These models offer a nuanced understanding of complex biological interactions and have shown promise in enhancing prognostic accuracy.

In a comprehensive study, ovarian cancer patients from three distinct cohorts were analyzed for survival prediction: TCGA, the Prostate, Lung, Colorectal, and Ovarian Cancer Screening Trial (PLCO), and the Harbin Medical University Cancer Hospital (HMUCH) cohorts. The study utilized 99 Formalin-Fixed Paraffin-Embedded (FFPE) samples from the TCGA cohort for model development, with 192 frozen slides from the same patients set aside for fine-tuning. Remaining 932 frozen slides from TCGA along with 608 slides from the PLCO cohort and 94 from the HMUCH cohort were employed for evaluating the model's performance. The Ovarian Cancer Digital Pathology Index (OCDPI) was calculated using CTransPath, a histopathological feature extraction tool [40], followed by a graph-based aggregation module. Kaplan-Meier analysis of the stratified risk groups based on the OCDPI scores revealed significant results in the TCGA test cohort for overall survival (OS) (HR=1.562; 95% CI: 1.143-2.134, log-rank test p-value = 0.0048), disease-free survival (DFS) (HR=1.736; 95% CI: 1.174-2.566, log-rank test p-value = 0.0052), and progression-free survival (HR=1.456; 95% CI: 1.116-1.898, log-rank test p-value = 0.0053). Furthermore, the model demonstrated robust performance in OS discrimination in external datasets, with HRs of 1.916 (95% CI: 1.380-2.660; log-rank test p-value < 0.001) for the PLCO dataset and 2.796 (95% CI: 1.404-5.568; log-rank test p-value = 0.0022) for the HMUCH dataset. The study also delved into the genetic and molecular aspects of ovarian cancer. The integrated gradient method was used to compute gradients for each histopathological patch, leading to the identification of ten prognosis-related clusters. Utilizing the CIBERSORT deconvolution method to estimate the abundance of infiltrating immune cells from bulk RNA-seq data, it was observed that clusters associated with favorable prognosis positively correlated with the abundance of T cells follicular helper and activated dendritic cells, and negatively with eosinophils. In contrast, clusters indicative of poor prognosis showed positive correlations with activated mast cells and neutrophils but a negative correlation with activated dendritic cells. Further analysis using single-sample gene set enrichment of functional gene expression signatures revealed that higher-risk clusters were positively correlated with angiogenesis, fibroblast activity, and

pro-tumor microenvironments, whereas lower-risk clusters showed inverse trends. Poor prognostic clusters were also associated with pathways related to carcinogenesis and tumor metastasis, including adipogenesis, Notch signaling, epithelial-to-mesenchymal transition, and protein secretion, while favorable prognosis clusters exhibited a negative correlation with these pathways [41].

Another notable study by Azarianpour et al. set out to predict the survival outcomes of 926 patients with gynecological cancers, using diagnostic histology slides. This study involved a semi-automated annotation process to identify four distinct cell types: epithelial and stromal tumor infiltrating lymphocytes, along with epithelial and stromal non-lymphocyte cells. Then, four classes of proximity graphs for each histological patch were defined by constructing the spatial graphs. The research focused on extracting features that described the geospatial architecture and interactions between tumor-infiltrating lymphocytes and cancer nuclei within individual tissue compartments. These features encompassed both the spatial arrangement of each cell class and the interplay between different cell types. To translate these patch-level features to patient-level insights, the study computed six statistical measures across various types of patches in whole slide images, resulting in a comprehensive set of features per patient. These features were then analyzed using the least shrinkage and selection operator method, identifying the most prognostic features for inclusion in a Cox regression model. This approach led to the creation of the ArcTIL risk score, a linear combination of selected features and their corresponding coefficients. Based on these risk scores, patients were categorized into high and low risk groups. The model was initially developed using data from 51 ovarian cancer cases and subsequently evaluated on an independent set of 52 ovarian cancer cases. Additionally, its applicability was extended to other cancer types, specifically cervical and uterine cancers. The evaluation demonstrated notable impacts of these risk groups on survival outcomes across these cancer types. In ovarian cancer test cohort, the model exhibited an HR of 1.96 [95% CI: 1.02-3.76] and a c-index of 0.69 [42].

In the field of pan-cancer survival analysis, the PC-CHiP model, developed by Fu et al., represents a significant advancement. This study encompassed a compre-

hensive analysis of 17,396 Hematoxylin and Eosin (H&E) stained histopathology slides from 10,452 patients across 28 diverse cancer types. The study's objectives were multifaceted, encompassing cancer type classification, the correlation between genetic and histological data, and the prediction of survival outcomes. For feature extraction from the histopathology images, a pretrained Inception-V4 architecture was utilized [43]. Survival analysis was subsequently conducted using a penalized Cox's proportional hazard regression, which incorporated a mix of L1 and L2 regularization, a method commonly referred to as the Cox elastic net. Focusing on the ovarian cancer cohort within this study, it was observed that the inclusion of histological data in the survival analysis model led to an improvement in predictive performance compared to using only grade and subtype information. Despite this enhancement, the mean c-index for the ovarian cancer cohort was reported to be below 0.6 [44].

Several other studies have focused on classification tasks with the objective of predicting different clinical outcomes. These studies, while not directly engaging in survival analysis, leverage artificial intelligence for binary classification, which is generally a simpler task. One such study reported a sensitivity of 73% and a specificity of 91% in differentiating between patients with low platinum-free intervals of six months or shorter and those with high intervals of 18 months or longer [45]. Another research effort distinguished 85 patients experiencing recurrence from 46 patients without recurrence, achieving an Area Under the Receiver Operating Characteristic (AUROC) of 0.71 [46]. Additionally, a third study successfully classified treatment resistance in a test set of 40 patients, achieving a mean AUROC of 0.846 ± 0.009 [47]. It is important to note that these studies, while contributing valuable insights into patient outcomes, primarily focus on binary classification tasks. This approach is distinct from the more complex and nuanced methods used in survival analysis, which often involve modeling time-to-event data and addressing the challenges of censored data. Consequently, while these classification studies are instrumental in their respective areas, they represent a different aspect of predictive modeling in medical research compared to survival analysis.

2. MATERIALS AND METHODS

2.1 Overview of Datasets

For the development and testing of the deep learning model, the TCGA-OV dataset was utilized. Additionally, data collected from Başkent University Hospital, adhering to the ethical permit granted with a number of E-94603339-604.01-314783 was used for external validation of the image encoders. The TCGA dataset comprised histopathology images, patient clinical variables, and genetic data, encompassing mutation details, transcriptome analysis, DNA methylation, CNVs, and protein expression profiles. Conversely, the Başkent dataset was limited to histopathology images and select clinical information, including patient age and follow-up data.

2.1.1 TCGA Dataset

Histopathology images, clinical variables and genetic data were acquired from TCGA dataset. Inclusion criteria encompassed primary ovarian cancer patients with both histopathology images and follow-up data.

2.1.1.1 Histopathology Images. In this study, both FFPE and frozen section slides, stained with H&E, were used, which were procured from the TCGA data portal [48]. Tissue areas on these slides were meticulously segmented, following which 1024 x 1024 pixel patches were generated from each slide. This process was facilitated by the segmentation algorithm of the CLAM model [49].

2.1.1.2 Clinical Data. The dataset, accessed through the cBioPortal website [50], initially included the following clinical variables:

1. Demographic Data of the Patient
    - Age
    - Sex
    - Race
    - Ethnicity
    - Jewish Religion Heritage Indicator
2. Information Regarding the Diagnosis of the Cancer
    - History of Other Malignancy
    - Initial Pathologic Diagnosis Year
    - Method of Initial Sample Procurement
    - Histological Diagnosis
3. Stage or Evolvement of the Cancer
    - Grade
    - Vascular Invasion Indicator
    - Lymphovascular Invasion Indicator
    - Extra-nodal Involvement
    - Clinical Stage: T, N, M stages and total stage
    - Pathological Stage: T, N, M stages and total stage (AJCC or other)
4. Treatment Type and Consequences
    - History of Neoadjuvant Treatment
    - Adjuvant Treatment: Radiation/Pharmaceutical
    - Treatment Outcome of First Course
    - New Tumor Event after Initial Treatment
    - Residual Tumor
    - Tumor Status

- Performance scores after treatment: Karnofsky Performance Score, ECOG Score, Performance Status Timing

Twenty-six variables, exhibiting missing values in over half of the cases, were excluded to maintain data integrity and reliability. Sex and tumor status at the last follow-up were excluded since all cases involved female patients, and tumor presence was determined during follow-up, which did not align with the study's objectives. The variable 'History of Neoadjuvant Treatment' was excluded as it was relevant for only one patient. A binary clinical stage variable was added in the feature set in which stages I and II were classified as 'low stage' and stages III and IV as 'high stage'.

The remaining seven clinical features comprised:

- Age
- Race: White, Black, Asian
- Ethnicity: Hispanic or non-Hispanic
- Method of Initial Sample Procurement: tumor resection, fine needle aspiration cytology, incisional biopsy, excisional biopsy
- Grade: G1, G2, G3, G4
- Clinical Stage: I, II, III, IV
- Stage (binary): low or high

Categorical variables were encoded, culminating in a total of eighteen features for subsequent analysis. Missing variables were filled using the median value of the discovery set for feature selection process and train set during deep learning training. Similarly, z-score normalization was performed using the mean and standard values of discovery and train sets for feature selection and deep learning, respectively.

2.1.1.3 Genomic Profiles. A comprehensive analysis of the genetic data from patients with primary ovarian cancer was conducted using the TCGA dataset, accessed through the cBioPortal website. This dataset encompasses a wide range of genetic information, which is crucial for understanding the complex nature of ovarian cancer. To ensure a thorough exploration, data from various types of genetic analyses were included, each contributing unique insights into the cancer's characteristics.

- **Copy-Number Variation (CNV):** The study used putative copy-number calls determined by GISTIC 2.0. These values, ranging from -2 to +2, provide an indication of the loss or gain in the copy number of each genomic strand, highlighting significant genomic changes that could influence cancer development and progression.
- **Mutation Data (Mut):** Binary variables indicating the presence of mutations were extracted from whole exome sequencing, with silent mutations being excluded. This approach focuses on identifying functionally relevant genetic alterations, thereby enhancing the potential predictive power of the analysis.
- **DNA Methylation (DNAm):** The study utilized beta values obtained using Human Methylation 27 probes. These continuous variables are instrumental in representing the methylation degree at specific genomic sites, offering insights into epigenetic modifications in cancer cells.
- **mRNA Sequencing (mRNA-Seq):** Gene expression values estimated by RNA Seq V2 RSEM were included in the dataset. This technology is recognized for its enhanced accuracy in quantifying gene expression compared to traditional microarray methods [51]. The continuous variable data from this analysis offer a detailed view of the gene expression patterns in ovarian cancer.
- **Reverse-Phase Protein Array Expression (RPPA-Exp):** Protein expression levels, measured using a reverse-phase protein array were also used. This data is essential for understanding the protein landscape of cancer cells, providing a direct link between genetic alterations and functional outcomes in the cell.

The duplicated genes were handled by taking the mean or median for the continuous and categorical data, respectively. DNA methylation and protein expression data included missing values, which were filled with median values extracted from the discovery set for feature selection algorithms and the train set for deep learning training.

2.1.1.4 Data Categorization. The dataset assembly for each training iteration was meticulously designed around the available genetic data types, focusing on the intersection of cases possessing complete datasets. This methodology was essential due to the potential for substantial missing data if all cases were included indiscriminately. Concentrating on the intersecting cases allowed for the maintenance of data quality and integrity, reduced the likelihood of model overfitting, and upheld the validity of multivariate analyses. Empirical observations from initial experiments underscored that filling in missing data could inadvertently weaken the models' predictive accuracy. To facilitate a balanced comparison among various models and account for disparities in dataset sizes, the datasets were systematically categorized into six distinct groups.

This categorization yielded three primary data groupings: Large, Medium, and Small. The Large group comprised datasets that were nearly available to all cases. The Medium and Small groups were distinguished based on whether they contained datasets from at least half of the cases, with the Medium group being further divided into Medium-high and Medium-low subgroups to align data sizes more closely. The Small data category was similarly divided into three subgroups (I, II, and III) to facilitate nuanced analysis. To maintain consistency and comparability in experiments, predetermined test and validation splits were rigorously applied across all studies. These splits were established prior to any analytical undertakings, ensuring the integrity of the test set for accurate model evaluation and comparative assessments.

2.1.2 Başkent Dataset

The dataset comprising ovarian cancer patients was retrospectively assembled from Başkent University Hospital records spanning the years 2011 to 2020. The collection process adhered to a consecutive sampling method. The inclusion criteria for this dataset were specifically defined to ensure the relevance and uniformity of the data. These criteria included patients with a serous histological subtype of ovarian cancer, the availability of histopathological images, and follow-up information. Conversely, the exclusion criteria were meticulously established to omit data that could introduce biases or inconsistencies. This included slides that contained non-ovarian tissue, those obtained from recurrent tumors, and cases where the patient had a history of chemotherapy for a recent pelvic tumor.

OS durations were determined by subtracting the date of initial diagnosis from the date of death or last known follow-up. The DFS interval was established from the conclusion of primary treatment to the occurrence of relapse or the last follow-up without any relapse.

Selected H&E stained FFPE and frozen section slides were scanned using the Hamamatsu NanoZoomer S60 model digital pathology scanner with 20x zoom mode. In line with the approach taken for TCGA data, the slide images underwent patching using the CLAM model, ensuring consistency in the preprocessing steps across different data sources.

2.2 Feature Engineering

Both image and tabular data underwent extensive feature engineering to enhance the predictive accuracy of survival outcomes in this research. For the image data, experimentation with three different encoders provided insights into optimal feature extraction techniques. Simultaneously, the tabular data, comprising clinical and genetic information, was processed using a combined approach of statistical methods

and neural network algorithms. This comprehensive strategy aimed at selecting the most promising clinical and genetic data features, thereby improving the potential for accurate survival predictions.

2.2.1 Image Feature Extraction

For the purpose of training, this study used image features rather than direct analysis of whole-slide images to enhance computational efficiency and facilitate multiple experimental iterations, particularly in the exploration of multi-modal fusion techniques. Features were derived from patches using three distinct pretrained models across both TCGA and Başkent datasets:

- **ResNet-50:** A deep convolutional neural network architecture, ResNet-50 is renowned for its 'residual learning' function to facilitate the training of deeper networks. The skip connections within the architecture are designed to prevent the vanishing and exploding gradients problem. In this study, ResNet-50 was used with its pretrained weights based on the ImageNet dataset, leveraging its extensive feature recognition capabilities [52].

- **CTransPath:** CTransPath represents an innovative network tailored for pathological images. The backbone network employs the Swin Transformer framework [53], where the patch partition is replaced by a convolutional neural network structure. It was initially pretrained on the unlabeled TCGA dataset. The usage of CTransPath in this study, with its TCGA-based pretrained weights, highlights its adaptability and effectiveness in handling complex cancer tissue imagery [40].

- **HistoSSL:** HistoSSL, a self-supervised transformer-based framework, is specifically designed for histopathological image analysis using masked image modeling. This technique involves concealing portions of the input images and training the model to predict these missing parts, thereby learning robust feature representations. Employed with weights pretrained on the unlabeled TCGA data,

HistoSSL's architecture proves effective at discerning intricate patterns in histological images, thus enhancing the feature extraction process [1].

2.2.2 Tabular Data Processing

The process of feature selection was executed in two main stages: statistical methods and a neural network approach, as visualized in Figure 2.1. Initially, the aim was to generate numerous feature sets through statistical techniques, subsequently narrowing down to the most effective set via neural network evaluation. This procedure was applied across various data types, including clinical, CNV, Mut, DNAm, mRNA-Seq, and RPPA-Exp data, with all features undergoing Z-score normalization as shown in Eq. 2.1:

$$x' = \frac{(x - \mu)}{\sigma} \tag{2.1}$$

Here, μ and σ denote the mean and standard deviation of the development dataset, respectively.

2.2.2.1 Statistical Feature Selection. This phase employed multiple statistical strategies, individually and collectively, to refine the feature set:

- Variance Threshold: Variables exhibiting a variance of less than 1% were excluded.
- Multi-collinearity Reduction: Features that were found to have an absolute Pearson correlation coefficient exceeding 70% were identified. In such cases, one of the collinear features was retained, while the others were eliminated. For clinical data, the selection process prioritized features most correlated with survival time. Due to high dimensionality, this choice was random for other data types, balancing computational efficiency.
- Univariate Analysis: Cases were divided into two groups using the median of

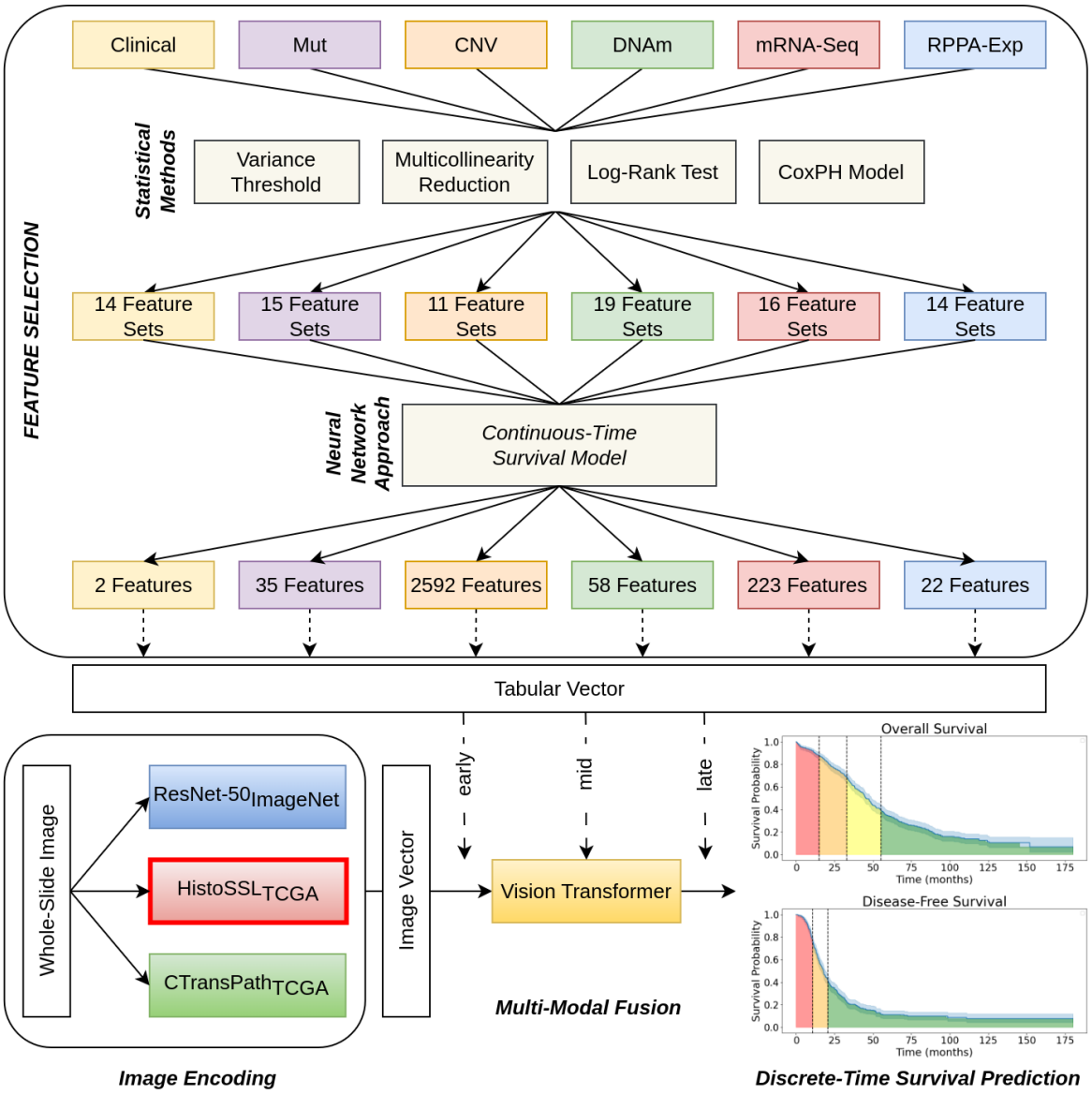


Figure 2.1 Overview of Analytical Processes. This figure delineates the sequential methodology applied to both tabular and image data, aimed at predicting survival outcomes in ovarian cancer patients. Feature selection for clinical and genetic data yields the most representative tabular data. Among three evaluated image encoders, HistoSSL was selected as the most effective for image data feature extraction. The extracted patch features were subsequently integrated with tabular data using various fusion techniques to compute patient-level discrete-time survival probabilities. The Kaplan-Meier plots, depicted in the figure, belong to the TCGA dataset and illustrate the survival probability estimates.

each feature and lifelines library is used to perform log-rank test. The features with a p-value of less than 0.05 were selected.

- Multivariate Analysis: Cox's Proportional Hazards Model with L1 and L2 regularization, as implemented in the Sci-kit Survival library, was used for multivari-

ate feature selection [54]. Three different alpha values (0.001, 0.01, and 0.1) were tested.

Combinations of these methods were also employed to enhance the selection process. This strategy involved identifying the intersection of features as determined by different methods. However, an exception was made in the case of multivariate analysis due to its unique characteristics. Rather than simply identifying intersecting features, multivariate analysis was applied to each combined feature set. For example, when integrating all selection methods, features that were selected through variance threshold, multi-collinearity reduction, and univariate analysis were first identified. Following this identification, these features then underwent multivariate analysis. This approach allowed for a comprehensive evaluation of features, leveraging the strengths of each individual method while also benefiting from their synergistic combination. To enhance computational efficiency, any duplicated lists resulting from these combinations were removed, preventing redundant calculations.

2.2.2.2 Neural Network-based Feature Selection. The feature selection lists generated by the statistical methods detailed in the previous section were further evaluated using deep learning approaches. Specifically, an MLP with skip connections, as depicted in Figure 2.2, was employed. This model comprised four MLP blocks, each consisting of a linear layer followed by batch normalization, a rectified linear unit (ReLU) activation function, and a dropout layer with a dropout probability of 0.25. To mitigate overfitting, particularly for inputs with fewer than 100 features, a simplified model incorporating only one MLP block was utilized. Tabular features extracted through this architecture were passed through a classification head that consisted of two fully-connected layers to yield risk scores.

The methodology approached the problem as a continuous time regression model, aligning with the Cox-nnet framework [55]. The survival loss function used in the model is a PyTorch implementation of the loss described in Travers Ching's negative partial log-likelihood loss implementation [56], mathematically represented as:

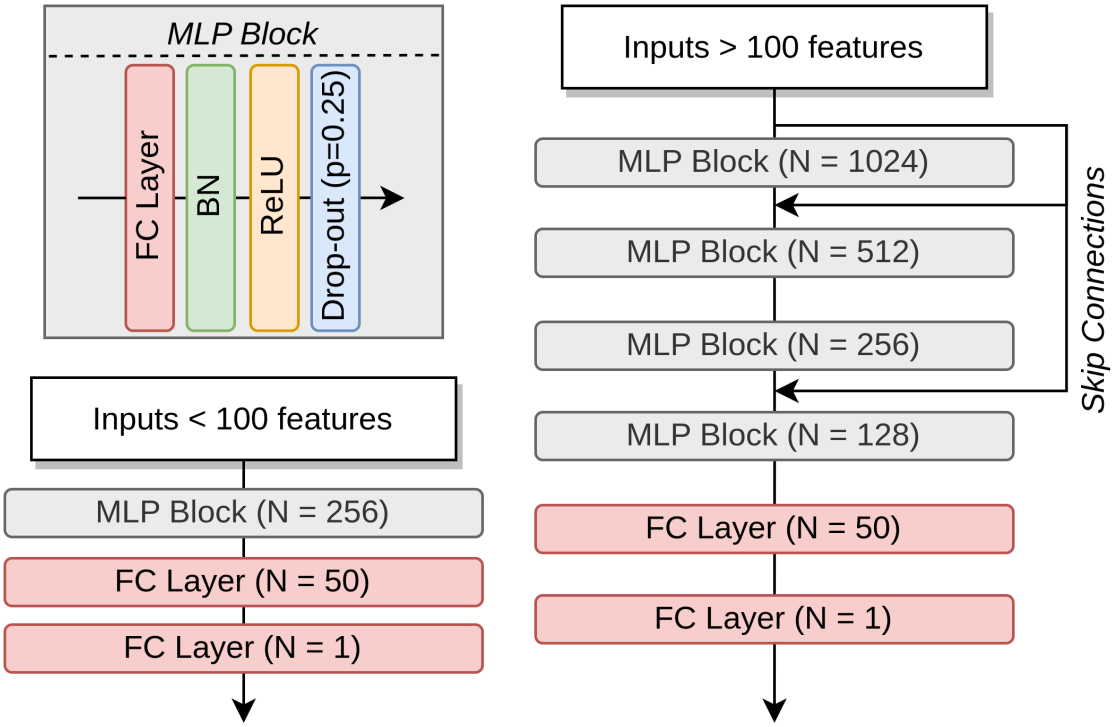


Figure 2.2 Neural Network Architectures for Processing Tabular Data. This figure depicts the neural network architecture consisting of multi-layer perceptron (MLP) blocks, tailored to the number of features. Each block includes a fully-connected (FC) layer, batch normalization (BN), rectified linear unit (ReLU) activation, and a dropout layer with a 0.25 dropout rate.

$$\text{Loss} = -\frac{1}{N}\sum_{i=1}^{N}\left[\hat{h}_\theta(x_i) - \log\left(\sum_{j\in R(T_i)} e^{\hat{h}_\theta(x_j)}\right)\right](1-c_i) \tag{2.2}$$

Where N is the total number of cases, $\hat{h}_\theta(x_i)$ is the estimated risk for sample i, as predicted by the model, $R(T_i)$ is the risk set at the event time T_i for the i-th sample, including all samples that have not yet experienced the event or been censored. c_i is the censorship indicator, which is 0 if the event occurred for sample i and 1 for censored cases. This ensures that the loss contribution is zero for censored cases. The loss is computed as the negative average of the differences between each sample's risk score and the logarithm of the sum of exponentiated risk scores of all samples in its risk set, weighted by the event indicator.

Training used the Adam optimizer, noted for its efficacy in deep learning contexts, with a learning rate set to 0.001. The batch size, determining the number of samples processed before each parameter update, was established at 16. To ensure the stability of the training process, especially in preventing the exploding gradient problem, gradient clipping with a threshold of 32 was implemented. The training duration was capped at a maximum of 100 epochs, but with an early stopping mechanism set to activate after 15 epochs without performance improvement on a validation set measured by the loss value. Additionally, to further mitigate overfitting, a regularization parameter of 0.001 was applied. This parameter penalizes larger weight values in the model, promoting the development of simpler, more generalizable models.

In the conducted analysis, each of the six data categories–clinical, CNV, Mut, DNAm, mRNA-Seq, and RPPA-Exp–underwent individualized training based on feature sets identified through statistical methods. To ensure robust comparability between datasets of varying sizes, a bootstrapping technique with 1000 iterations was utilized. Furthermore, to ascertain the models' generalizability, a 5-fold cross-validation strategy was implemented. The evaluation of model performance involved calculating the mean test c-index from cross-validation results across bootstrapping, in addition to pooled variance and 95% confidence intervals (CI), as per the following formula:

$$s_p^2 = \frac{(n_1 - 1)s_1^2 + (n_2 - 1)s_2^2}{n_1 + n_2 - 2} \tag{2.3}$$

$$CI = \overline{x} \pm z\frac{s}{\sqrt{n}} \tag{2.4}$$

where n denotes the sample sizes, s the standard deviations, z the z-score for the specified confidence level, and $\overline{x}$ the mean of the samples. The optimal feature set, distinguished by the highest mean test c-index, was selected for subsequent application within each data type.

2.3 Model Development and Training

A novel deep learning model was developed in this research, integrating architectural innovations with multi-modal fusion strategies to enhance survival prediction accuracy in ovarian cancer. The architecture is designed to seamlessly integrate image and tabular data, maximizing the predictive strength of both data types. Rigorous training and evaluation protocols were established to ensure the model's robustness and efficacy. Additionally, benchmarking against an existing model demonstrates a comparison in predictive performance, underscoring the developed model's contribution to the field of survival prediction.

2.3.1 Architectural Overview

Ovarian cancer Vision Transformer Aggregated Network (OViTANet), was designed to process patch features derived from all available slides of a patient. Additionally, when available, it integrates tabular data features extracted through a skip-connected MLP as given in Figure 2.2. At the core of the proposed model lies a Vision Transformer (ViT) architecture [57]–outlined in Figure 2.3–which serves as the primary mechanism for aggregating patch features. The initial phase involves generating a class token vector via random initialization, adhering to a normal distribution. This vector is subsequently merged with the patch features, and the amalgamated data undergoes a dropout process with a 0.5 probability to curb the risk of overfitting. Following this dropout layer, the model leverages five transformer blocks to refine the feature processing. Each transformer block comprises a multi-head attention (MHA) mechanism with four heads, each with a dimensionality of 16, and a feed-forward layer, facilitating complex feature extraction and transformation. The concluding segment of the model is an MLP head, consisting of two fully connected layers, to result in predictions for four time intervals for the OS prediction and three time intervals for DFS as it is a shorter time period.

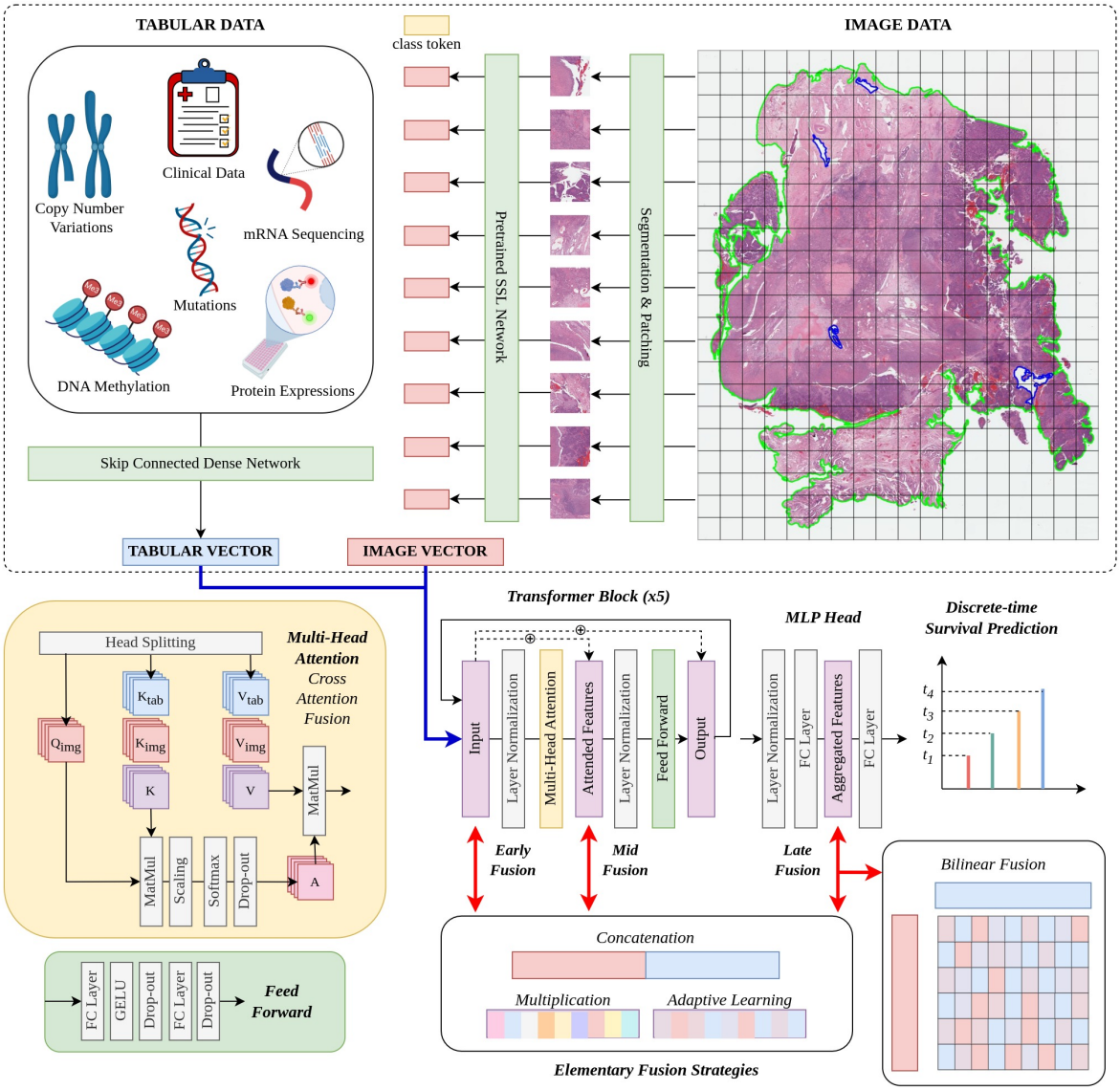


Figure 2.3 OViTANet Architecture. Image features are extracted using the pretrained self-supervised learning (SSL) network, HistoSSL [1], following segmentation and patching. Tabular data is processed through a dense network with skip connections to generate an embedding vector for the tabular data. This research explores diverse multi-modal fusion strategies including elementary techniques, such as concatenation, adaptive learning, and multiplication, which are applied at various stages of the model–early, mid, and late. Notably, a mid-level cross-attention mechanism is introduced, where keys (K) and values (V) are concatenated from both image and tabular data vectors, while queries (Q) are derived exclusively from image data, facilitating enhanced focus during multi-head attention processes. Moreover, bilinear fusion is utilized as a sophisticated late-stage fusion method, aiming to capture more complex interactions between the modalities. After five transformation blocks that consists of multi-head attention and feed forward modules, a multi-layer perceptron (MLP) head, comprising two fully-connected (FC) layers, yields discrete-time survival predictions.

2.3.1.1 Multi-Modal Fusion.

In the quest to identify the top-performing multi-modal data fusion method for this project, a range of fusion techniques were explored. These ranged from straightforward approaches like concatenation and multiplication

to more sophisticated techniques such as cross-attention. To assess the impact of fusion at different stages of the model, three distinct locations within the architectural framework were chosen for implementing early, mid, and late fusion strategies. The integration strategies for tabular data within the deep learning model's architecture were diversified to explore varying impacts on performance and feature representation. These strategies are categorized as follows:

- **Early Fusion:** Characterized by the incorporation of tabular data immediately after the process of concatenating the class token. This method aims to infuse auxiliary data at the inception of the model's computational pathway, enriching the initial feature set before it undergoes further transformation.
- **Mid Fusion:** This strategy diverges by introducing tabular data at strategic junctures within the model, specifically during or after the operations within each multi-head attention block. The implementation of mid fusion is adaptable, with its execution and the technique of fusion varying to facilitate a dynamic and contextually informed integration of data at the mid-points of the feature processing pipeline.
- **Late Fusion:** Implemented in the latter stages of the model, specifically between the two dense layers of the classifier head, where the resulting vectors align in dimensionality, each being 50. Late fusion aims to augment the processed features with additional data immediately preceding the final decision-making phase, thereby allowing the model to leverage this late-stage contextual information for refined classification outcomes.

In total, five distinct fusion techniques were incorporated into the project, each evaluated for its efficacy in enhancing model performance and data integration. These techniques include:

- **Concatenation:** It is the most straightforward method of combining features from different sources or modalities. It involves aligning the features end-to-end

to form a longer, unified feature vector. If $\mathbf{X_1}$ and $\mathbf{X_2}$ are two feature vectors (or matrices, in the case of batch processing), their concatenation $\mathbf{X}_{\text{concat}}$ is given by:

$$\mathbf{X}_{\text{concat}} = \text{concat}(\mathbf{X_1}, \mathbf{X_2}) \tag{2.5}$$

where concat$(\cdot)$ denotes the concatenation operation. The dimensionality of $\mathbf{X}_{\text{concat}}$ is the sum of the dimensionalities of $\mathbf{X_1}$ and $\mathbf{X_2}$. To ensure an equal contribution of both tabular and image features, the tabular features were embedded to match the size of the image features, which was 786 for early and mid fusions and 50 for late fusion. This method is particularly useful when each set of features captures distinct aspects of the data, and we want the downstream model to learn from the full spectrum of information.

- **Adaptive Learning:** Adaptive fusion, or weighted sum fusion, is a more dynamic approach that involves combining features by taking their weighted sum. The weights can be learned during training, allowing the model to adaptively decide the relative importance of each feature set. Given feature vectors $\mathbf{X}_1$ and $\mathbf{X}_2$, and their corresponding learned weights α and β, the adaptive fusion $\mathbf{X}_{\text{adaptive}}$ is computed as:

$$\mathbf{X}_{\text{adaptive}} = \alpha \cdot \mathbf{X}_1 + \beta \cdot \mathbf{X}_2 \tag{2.6}$$

where α and β are scalar weights, usually constrained to sum up to 1 for normalization. A key advantage of this method lies in its capacity to capitalize on the impact of the feature that offers the most benefit for the primary task.

- **Multiplication**: In this method, the features are simply combined by element-wise multiplication. For feature vectors $\mathbf{X}_1$ and $\mathbf{X}_2$, their multiplication fusion $\mathbf{X}_{\text{mult}}$ is given by:

$$\mathbf{X}_{\text{mult}} = \mathbf{X}_1 \odot \mathbf{X}_2 \tag{2.7}$$

where $\odot$ denotes element-wise multiplication. The dimensions of the two vectors, $\mathbf{X}_1$ and $\mathbf{X}_2$, were maintained identically, as in concatenation. Consequently, the resultant vector $\mathbf{X}_{\text{mult}}$retains the same dimensionality as the individual input

vectors.

The significance of this approach lies in its ability to introduce non-linearity, which is a crucial aspect for capturing more complex relationships within the data. Unlike linear operations, such as concatenation or weighted-sum, the element-wise multiplication of vectors creates an interaction effect between corresponding elements. This interaction enables the model to discern and represent more intricate patterns and dependencies that might exist within and across the datasets, potentially leading to more robust and accurate predictions in complex problem-solving scenarios.

- **Bilinear Fusion:** It is the strategy delineated in the PORPOISE model [2] for the effective integration of data across multiple modalities. Central to this method is the use of a Kronecker Product Fusion technique, which forms a comprehensive multimodal feature representation. This technique is essential for capturing the interactive dynamics between two distinct modalities, achieved by the pairwise multiplication of neurons from each modality. The mathematical representation of this process is given by:

$$\mathbf{h}_{\text{fusion}} = \mathbf{h}_{\text{patch}} \otimes \mathbf{h}_{\text{tabular}} \tag{2.8}$$

In this formula, $\otimes$ symbolizes the Kronecker Product. The resulting multimodal tensor $\mathbf{h}_{\text{fusion}}$ resides in $\mathbf{R}^{51\times51}$, accounting for an additional constant value of "1" appended to each unimodal feature to preserve individual modality characteristics.

A crucial aspect of this approach is the incorporation of a gating-based attention mechanism. This mechanism enhances the fusion process by assigning relative importance to each feature within a modality, denoted as $\mathbf{h}_i$. The attention mechanism generates scores $\mathbf{z}_i$ that reflect how much each feature in $\mathbf{h}_{\text{patch}}$ and $\mathbf{h}_{\text{tabular}}$ focuses on specific aspects of $\mathbf{h}_i$. The gated feature representation $\mathbf{h}_{i,\text{gated}}$ emerges from the element-wise multiplication of $\mathbf{z}_i$ and $\mathbf{h}_i$, as described below:

$$\mathbf{h}_{i,\text{gated}} = \mathbf{z}_i \times \mathbf{h}_i, \text{ for all } \mathbf{h}_i \in \{\mathbf{h}_{\text{patch}}, \mathbf{h}_{\text{tabular}}\} \tag{2.9}$$

$$\text{where, } \mathbf{h}_i = \text{ReLU}(\mathbf{W}_i \cdot \mathbf{h}_i) \tag{2.10}$$

$$\mathbf{z}_i = \sigma(\mathbf{W}_i \cdot [\mathbf{h}_{\text{patch}}, \mathbf{h}_{\text{tabular}}]) \tag{2.11}$$

Gating precedes fusion for both modalities, accompanied by skip connections to a later hidden layer in the multimodal network. Following the fusion, the resulting tensor undergoes further processing through two hidden layers, each comprising 256 units. As the dimensionality of the patch features and tabular data are needed to be the same, this fusion is only applied as late fusion.

- **Cross-Attention:** This fusion method, specifically designed for integration within the Vision Transformer (ViT) architecture in this project, as illustrated in Figure 2.3, introduces a novel approach to feature fusion by operating directly within the attention mechanism. In this method, both tabular and image features are divided into three segments to represent the key, value, and query components essential to the attention mechanism. For the process of fusion, keys and values are derived by concatenating corresponding segments from both tabular and image features, thereby enriching the contextual information available for attention computation. The query component, however, is exclusively sourced from the image features, maintaining a visual-centric perspective for the attention process. The mechanism then proceeds with the calculation of the scaled dot-product attention, where the dot product of the query with each key is computed, scaled by the dimensionality of the keys to ensure stable gradients, and then passed through a softmax function to obtain attention weights. After a drop-out layer, these weights are subsequently used to aggregate the values, producing an output that embodies a weighted combination of features, effectively merging information from both modalities.

  This cross-attention method leverages the MHA architecture by performing the described process in parallel across multiple heads, each potentially focusing on different aspects of the feature interaction. MHA enhances the model's capacity to capture various relationships within the data, allowing for a more comprehensive and nuanced integration of the tabular and image features. The outcome

is a feature representation that is deeply informed by the interplay between the different data types, poised to improve the model's performance by leveraging the strengths of each modality.

2.3.2 Training and Evaluation

The model's training regimen was governed by the Adam optimizer, set to a learning rate of 0.001 and augmented by a weight decay of the same magnitude. Training was constrained to a maximum of 100 epochs, accompanied by a gradient clipping threshold established at 32. To enhance the training efficiency and prevent overfitting, an early stopping mechanism was integrated, activated in the absence of any reduction in validation loss across a span of 15 consecutive epochs. This criterion was applied subsequent to the initial 5 epochs and contingent upon the training surpassing a minimal threshold of 20 epochs. Batch size was one and the patches from all slides pertaining to a single patient were processed collectively. A notable training strategy involved randomly selecting 50% of the patches during the training phase to avoid overfitting, while all patches were used during the validation and testing phases for comprehensive model evaluation.

The experiments to identify the best performing fusion methods for each data category was conducted with one set of train, validation and test. Then, the top results from each data category was further trained using 5-fold cross-validation. Model weights were saved when the validation loss was minimum in each fold and these weights were used to test on the predefined test set. Comparison of the image feature extractors were also performed using a 5-fold cross-validation and apart from the test set separated from the TCGA data, Başkent dataset was used as the external test set.

2.3.3 Benchmarking

PORPOISE model was selected for comparison as it effectively integrates histopathology and genetic data to predict survival outcome of the patients from various cancer types. Although their model achieved significant c-indices in many cancers, they did not report the results for ovarian cancer. The model was accessed through their GitHub page (`https://github.com/mahmoodlab/PORPOISE/`). Same inputs were used in OVi-TANet and PORPOISE for better comparison after the preprocessing steps as described above. Train, validation and test sets were also identical for both models. Default configuration was used for PORPOISE as described in the GitHub page with bilinear fusion, drop-out probability of 0.25, weight decay of 0.00001, learning rate of 0.0002, Adam optimizer, a maximum epochs of 20 and applying gradient clipping at every 32 epochs.

3. RESULTS

3.1 Insights from Data

In this investigation, two distinct datasets were employed: the TCGA and the dataset from Başkent University Hospital. The TCGA dataset is widely acknowledged for its comprehensive compilation of genetic information, offering an extensive array of demographics, clinical outcomes, and genomic profiles. It serves as an invaluable resource for the development of models aimed at enhancing survival predictions in ovarian cancer through the utilization of diverse data sets.

On the other hand, the dataset from Başkent University Hospital, which was meticulously assembled specifically for this research, provides a specialized assortment of clinical and pathological data aligned with the study's goals. It includes exhaustive patient records, featuring demographic details and clinical outcomes, all collected in accordance with the stringent data management protocols of the hospital. This dataset was particularly leveraged to assess the performance of image extractors that had been pre-trained on the TCGA data, offering a unique advantage due to its derivation from an entirely distinct cohort and geographical location.

3.1.1 TCGA Dataset Description

In this thesis, ovarian cancer patients with primary tumors and accompanying histology and follow-up data were considered. A total of 1263 histological slide images from 580 patients were obtained from the TCGA data portal, adhering to the specified inclusion criteria. Out of these, 104 images from 104 individual cases were sourced from FFPE slides, and the remaining 1159 images were from frozen sections. However, 23 of the frozen slides were not used due to insufficient image quality for effective tissue segmentation by the CLAM algorithm [49], leaving 1136 frozen slides from 579 patients.

Additionally, 5 cases of extra-ovarian carcinomas were excluded, finalizing the dataset at 1231 slides from 574 patients. Notably, all 104 patients with FFPE images also had frozen section images, contributing to a total of 301 (25%) images, while 470 patients only had frozen slides, accounting for 930 (75%) images. Exclusion process is depicted in Figure 3.1.

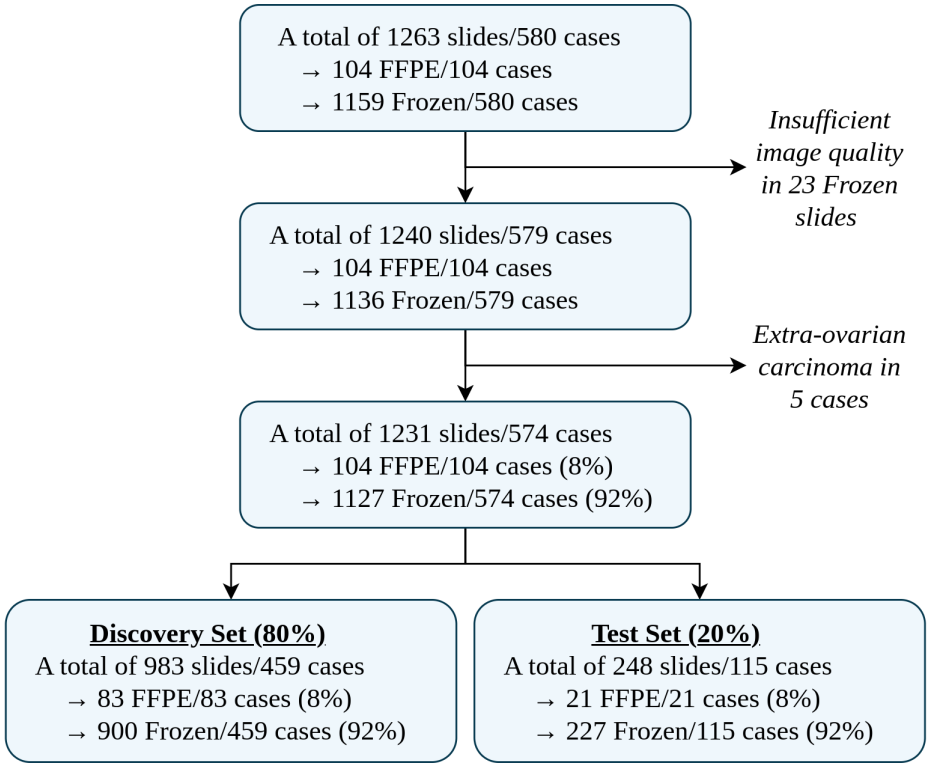


Figure 3.1 Exclusion Process and Dataset Splitting for Discovery and Test Sets. This figure illustrates the methodical exclusion and splitting process of the dataset showing the number of frozen and formalin-fixed paraffin-embedded (FFPE) slides in each set.

For the task of predicting OS, the test set was composed of 248 slides from 115 patients. This selection was strategically made to maintain the distribution across the time intervals and the proportion of frozen to FFPE slides. Conversely, the discovery set included the remaining 983 slides from 459 patients, serving as a substantial repository for initial analysis. Regarding DFS prediction, the dataset encompassed 490 cases with 1,036 slides, of which 959 were frozen and 77 were FFPE, all with recurrence information available. Specifically, 114 (20%) cases comprising 210 slides (194 frozen and 16 FFPE) were designated for the test set, leaving 826 (765 frozen and 61 FFPE) slides from 453 cases for the discovery set. This subset was also stratified by survival-time distribution and slide type. The delineation of the test set preceded all analytical

processes. The discovery sets played a crucial role in the feature selection for tabular data, laying the groundwork for the development of the deep learning model.

Table 3.1
Clinical characteristics for censored and uncensored cases in overall survival prediction are shown, listing continuous variables as mean ± standard deviation and categorical variables by count and percentage. P-values from t-test and chi-square analysis compare discovery and test set distributions.

Clinical Variables	Discovery Set		Test Set		
	Alive (N = 186)	Deceased (N = 273)	Alive (N = 47)	Deceased (N = 68)	p-value
Age	57.05 ± 11.96	61.31 ± 10.92	59.74 ± 12.11	60.6 ± 11.43	0.58
Hispanic	4 (1%)	7 (1%)	0 (0%)	0 (0%)	-
Race					0.28
White	150 (26%)	243 (42%)	37 (6%)	61 (11%)	>.99
Black	11 (2%)	18 (3%)	1 (0%)	3 (1%)	-
Asian	10 (2%)	4 (1%)	4 (1%)	2 (0%)	0.4
Biopsy					0.22
Resection	151 (26%)	222 (39%)	38 (7%)	49 (9%)	0.22
Cytology	24 (4%)	42 (7%)	7 (1%)	15 (3%)	0.26
Excisional	4 (1%)	3 (1%)	0 (0%)	0 (0%)	-
Incisional	3 (1%)	6 (1%)	1 (0%)	3 (1%)	-
Grade					0.96
G1	3 (1%)	2 (0%)	1 (0%)	0 (0%)	-
G2	24 (4%)	31 (5%)	2 (0%)	11 (2%)	0.97
G3	153 (27%)	234 (41%)	44 (8%)	53 (9%)	>.99
G4	0 (0%)	1 (0%)	0 (0%)	0 (0%)	-
Stage					0.2
I	12 (2%)	4 (1%)	0 (0%)	0 (0%)	-
II	17 (3%)	6 (1%)	5 (1%)	2 (0%)	0.82
III	139 (24%)	210 (37%)	38 (7%)	50 (9%)	>.99
IV	16 (3%)	52 (9%)	4 (1%)	16 (3%)	0.59
Survival Months	40.1 ± 37.23	38.25 ± 25.29	39.36 ± 36.18	36.93 ± 27.39	0.74

Demographically, the patients had an average age of 59.71 ± 11.55, ranging from 26 to 89 years. The majority were White (86%), followed by Black (6%), and Asian (3%). Hispanic patients constituted 2% (11 patients), while 59% (338 patients)

were non-Hispanic, and the ethnicity for the remaining cases was unreported. The primary diagnostic procedure for most patients was tumor resection, covering 460 (80%) of the cases, supplemented by other methods such as fine needle aspiration cytology in 88 (15%) cases, incisional biopsy in 13 (2%) cases, and excisional biopsy in 7 (1%) cases. Tumor differentiation varied, with a small percentage being well-differentiated G1 tumors (6 cases, 1%), but the majority were high-grade, including 68 (12%) G2, 484 (84%) G3, and 1 (0.2%) G4. The clinical stages were predominantly high, with 46 (8%) low-stage (16 Stage I and 30 Stage II) and 525 (91%) high-stage patients (437 Stage III and 88 Stage IV). The dataset reflected a balance in survival status, with 341 (59%) patients reported deceased and 233 (41%) alive at the last follow-up, and the mean OS time was 38.17 ± 30.40 months, ranging from 0.26 to 180.06 months. Regarding recurrence, it was recorded in 355 instances (72%), whereas 135 patients (28%) exhibited no recurrence at their most recent follow-up, with the average DFS period being 21.46 ± 22.18 months. The allocation of cases within the discovery and test sets for both OS and DFS prediction tasks has been detailed in Table 3.1 and Table 3.2, respectively. Subsequent analysis confirmed the absence of substantial discrepancies in the distributions across these sets, corroborated by elevated p-values derived from t-test and chi-square tests for continuous and categorical variables, respectively, indicating statistical non-significance.

3.1.1.1 Data Categories.

In an effort to address variations in dataset sizes and enhance comparative analysis across different models, the datasets were stratified into categories based on case availability. The distribution of train and test sizes for each genetic data category is depicted in Figure 3.2 for both OS and DFS prediction.

1. **Large:** Incorporates CNV and DNAm datasets and their combinations, with case counts ranging from 548 to 559 for OS and from 469 to 478 for DFS.

2. **Medium-high:** Encompasses RPPA-Exp datasets along with combinations of RPPA-Exp, CNV, and DNAm, with case counts between 392 and 414 for OS and between 340 and 359 for DFS.

Table 3.2
Clinical characteristics for censored and uncensored cases in disease-free survival prediction are shown, listing continuous variables as mean ± standard deviation and categorical variables by count and percentage. P-values from t-test and chi-square analysis compare discovery and test set distributions.

Clinical Variables	Discovery Set		Test Set		
	Non-Relapsed (N = 109)	Relapsed (N = 283)	Non-Relapsed (N = 26)	Relapsed (N = 72)	p-value
Age	58.84 ± 11.71	58.9 ± 11.28	58.46 ± 13.39	59.07 ± 12.08	0.98
Hispanic	2 (0%)	8 (2%)	0 (0%)	1 (0%)	-
Race					0.3
Asian	6 (1%)	9 (2%)	1 (0%)	3 (1%)	>.99
Black	8 (2%)	9 (2%)	0 (0%)	8 (2%)	0.2
White	85 (17%)	255 (52%)	23 (5%)	58 (12%)	0.38
Biopsy					0.7
Resection	92 (19%)	217 (44%)	22 (4%)	54 (11%)	0.89
Cytology	9 (2%)	55 (11%)	4 (1%)	13 (3%)	0.93
Excisional	4 (1%)	1 (0%)	0 (0%)	1 (0%)	>.99
Incisional	0 (0%)	8 (2%)	0 (0%)	4 (1%)	0.42
Grade					0.8
G1	1 (0%)	3 (1%)	1 (0%)	0 (0%)	>.99
G2	10 (2%)	34 (7%)	3 (1%)	11 (2%)	0.51
G3	94 (19%)	241 (49%)	21 (4%)	59 (12%)	0.43
G4	0 (0%)	1 (0%)	0 (0%)	0 (0%)	>.99
Stage					0.98
I	10 (2%)	1 (0%)	1 (0%)	1 (0%)	0.94
II	12 (2%)	12 (2%)	3 (1%)	3 (1%)	>.99
III	76 (16%)	226 (46%)	19 (4%)	57 (12%)	>.99
IV	10 (2%)	44 (9%)	2 (0%)	11 (2%)	>.99
Survival Months	28.91 ± 35.38	18.75 ± 13.34	27.3 ± 34.88	18.69 ± 14.64	0.81

3. **Medium-low:** Includes Mut, mRNA-Seq, and their selected combinations with CNV and DNAm, excluding direct mRNA-Seq and Mut pairings, featuring case counts from 288 to 312 for OS and from 236 to 266 for DFS.

4. **Small I:** Features datasets combining mRNA-Seq and RPPA-Exp with CNV and DNAm, as well as Mut and RPPA-Exp with CNV and DNAm, presenting case

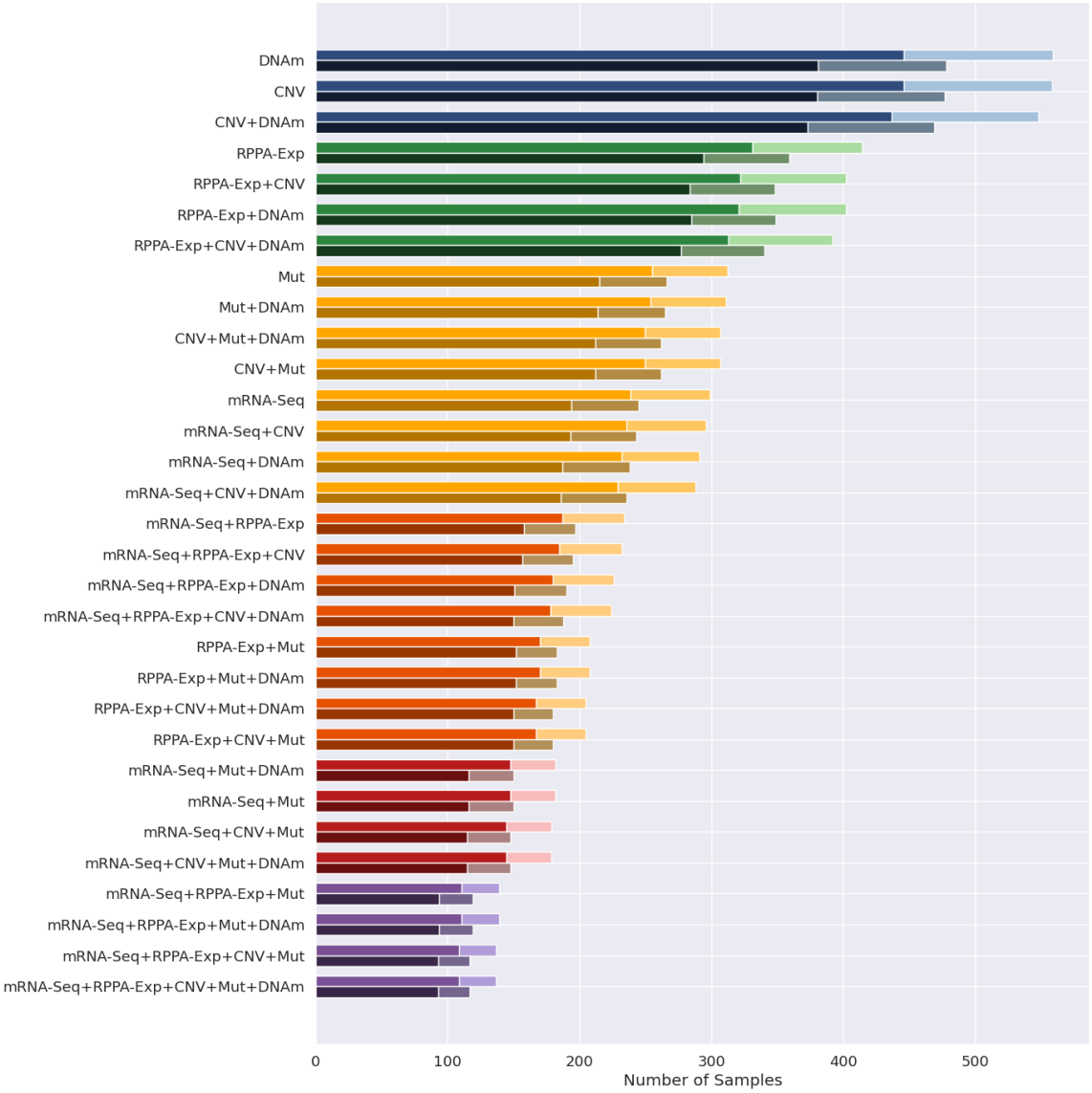


Figure 3.2 Distribution of Cases by Data Volume. This figure illustrates the allocation of cases across discovery and test sets for predicting overall (OS) and disease-free (DFS) survival, categorized into six data volumes: Large in blue, Medium-high in green, Medium-low in yellow, Small I in orange, Small II in red, and Small III in purple. Horizontally aligned bars indicate the case counts per category, with OS predictions featured as the top bar and DFS predictions as the lower bar within each data volume segment. Training and test sets are differentiated by color intensity, with training sets in deeper tones and test sets in lighter tones, showcasing the dataset composition for each prediction task.

counts from 205 to 234 for OS and from 180 to 197 for DFS.

5. **Small II:** Groups together cases with both Mut and mRNA-Seq and their CNV and DNAm combinations, showing case counts from 179 to 182 for OS and from 148 to 150 for DFS.

6. **Small III:** Covers cases including Mut, RPPA-Exp, and mRNA-Seq along with their CNV and DNAm combinations, with case counts ranging from 137 to 139 for OS and from 117 to 119 for DFS.

3.1.2 Başkent Dataset Description

Within the archives of Başkent University Hospital, 148 patients diagnosed with ovarian cancer from May 2011 through November 2020 were identified. Exclusions were made for 11 patients due to their diagnosis with non-serous subtypes–comprising 3 clear cell, 7 mixed, and 1 endometrioid. An additional 3 cases were omitted due to the exclusive presence of non-ovarian tissue slides. Consequently, a collection of 929 slides from 134 cases was amassed. Among these, 121 patients contributed 823 FFPE slides, while 12 patients provided 100 frozen slides. Notably, a single patient had a collection of both slide types, contributing 5 FFPE and 1 frozen slide.

The age distribution of patients spanned from 34 to 84 years, with an average age of 57.72 $\pm$ 11.63 years. At the last follow-up, 47 patients (35%) were alive, whereas 87 patients (65%) had deceased with a mean OS duration of 62.66 $\pm$ 36.14 months. Among the 76 patients for whom clinical data were accessible, including the conclusion date of primary chemotherapy, alongside remission and relapse details, recurrence was observed in 62 patients, constituting 82% of the cohort. The average DFS duration for these patients was calculated to be 25.64 $\pm$ 29.21 months.

3.2 Feature Selection Outcomes

The assessment of the predictive capability of the features was conducted using two distinct analytical strategies: statistical methods and neural network approaches. This evaluation spanned six different data categories, namely clinical variables, DNAm, CNV, mRNA-Seq, RPPA-Exp, and Mut. These categories were explored within the context of predicting both OS and DFS.

Initially, feature sets were identified through statistical analyses, employing methods aimed at capturing the most informative predictors for each data category. Subsequently, these feature sets underwent further refinement via a neural network strategy, specifically utilizing a continuous-time survival model designed to optimize the predictive performance for OS and DFS outcomes. From each data type, a singular set of features was chosen based on its demonstrated predictive strength. These selected feature sets were then employed in subsequent stages of the investigation, focusing on exploring various fusion techniques and combinations of data types.

3.2.1 Statistical Methods

Statistical methods were instrumental in discerning various feature sets across different data types, with the outcomes enumerated in Table A.1 for OS prediction and in Table A.2 for DFS prediction. Absences within the table signal either feature set repetitions by preceding methods or the absence of features, notably in the CoxPH model under high regularization ($\alpha = 0.01$). For clarity, features retained for each data type are highlighted in the corresponding table.

Clinical Features Initially, a variance threshold of 1% was employed, which resulted in the exclusion of only the variable G4, owing to its low variance of 0.0017 in the OS cohort and 0.0020 in the DFS cohort, indicating that it was only the highest grade (G4) that was excluded. Additionally, the analysis revealed the presence of collinearity, as evident in the heatmap of Pearson correlation coefficients (Figure A.1 for OS, resulted in the removal of four features, namely Cytology, G3, Clinical Stages II and III. The correlation pattern was the same for DFS prediction and the same features were removed. The univariate log-rank test resulted in selection of different features for OS and DFS predictions, as delineated in Table A.3. For OS, age, binary stage, clinical stages II and IV were pinpointed with significant p-values (<0.05), while for DFS these were ethnicity, G4, binary stage, clinical stages I and II. Advancing to multivariate analysis, a Cox proportional hazards model with L1 and L2 regularization was used, with resultant coefficients detailed in Table A.4, showcasing feature reduction through

zero coefficients with increasing α values. For OS prediction, the regularization values of α at 0.001, 0.01, and 0.1 selected seventeen, fourteen, and six features, respectively. On the other hand, only high regularization yielded in a distinct feature set for DFS prediction, consisting of six features.

Genetic Features The investigation incorporated varied data types, including CNV, Mut, DNAm, mRNA-Seq, and RPPA-Exp, reflecting different genetic material processing stages. For OS prediction, the feature selection process resulted in the establishment of 11 feature sets for CNV, 15 for Mut, 16 for mRNA-Seq, 19 for DNAm, and 14 for RPPA-Exp. In the context of DFS prediction, a total of 90 feature sets were delineated, encompassing 15 clinical feature sets, 12 for CNV, 16 for Mut, 16 for mRNA-Seq, 20 for DNAm, and 11 for RPPA-Exp.

The scope of CNV feature sets ranged from 13 (1%) to 2592 (10%) of 24,765 genes for OS prediction, and from 5 (0.02%) to 1373 (6%) for DFS prediction. Mutation data analysis yielded feature sets ranging from 32 (0.4%) to 2133 (24%) of 8765 genes for OS, and from 51 (0.6%) to 2703 (31%) for DFS. mRNA-Seq data analysis revealed feature sets ranging broadly from 105 (0.5%) to 19,840 (97%) of 20,515 genes for OS, and from 115 (0.6%) to 19,824 (97%) for DFS. DNAm feature sets spanned from 58 (0.4%) to 7,876 (55%) out of 14,373 variables for OS, and from 60 (0.4%) to 7880 (55%) for DFS. Lastly, for RPPA-Exp, the generated feature sets ranged from 13 (6%) to 191 (94%) of 204 proteins for OS, and from 11 (5%) to 188 (92%) for DFS.

3.2.2 Neural Network Approach

Following the derivation of feature sets through statistical methodologies each set underwent testing in a neural network framework. This framework was based on a continuous time survival model, employing 5-fold cross-validation and 1,000 bootstrap iterations for robust evaluation. In the context of OS prediction, 89 distinct runs across various data types yielded mean c-indices spanning from 0.37 ± 0.06 to 0.65 ± 0.03. For DFS prediction, analysis of 90 feature sets revealed mean c-indices ranging

between 0.41 ± 0.06 and 0.59 ± 0.06. The outcomes for each data type are documented in Figure A.3. Select feature sets demonstrating superior performance for each data type were advanced for further analysis. For OS prediction, the selected feature sets included:

- **Clinical Features:** Selection of age and clinical stage II from clinical variables, achieving a mean c-index of 0.65 ± 0.03.
- **Mut:** Selection of 35 genes, with a mean c-index of 0.60 ± 0.04.
- **RPPA-Exp:** Selection of 22 proteins, with a mean c-index of 0.59 ± 0.05.
- **mRNA-Seq:** Selection of 223 genes, with a mean c-index of 0.58 ± 0.06.
- **DNAm:** Selection of 58 genes, with a mean c-index of 0.55 ± 0.04.
- **CNV:** Selection of 2592 genes, with a mean c-index of 0.54 ± 0.04.

For DFS prediction, the top-performing feature sets comprised:

- **Clinical Features:** Inclusion of 10 clinical variables such as age, ethnicity, race (Asian and White), binary stage, biopsy type (excisional and resection), G2, and clinical stages I and IV, which led to a mean c-index of 0.56 ± 0.04.
- **Mut:** Selection of 397 genes, with a mean c-index of 0.59 ± 0.06.
- **RPPA-Exp:** Selection of 22 proteins, with a mean c-index of 0.58 ± 0.04.
- **mRNA-Seq:** Selection of 666 genes, with a mean c-index of 0.58 ± 0.06.
- **DNAm:** Selection of 865 genes, with a mean c-index of 0.55 ± 0.04.
- **CNV:** Selection of 434 genes, with a mean c-index of 0.56 ± 0.04.

3.3 Model Performance

The performance evaluation of the developed model highlights its predictive accuracy in survival prediction, focusing on three key areas: the efficacy of various image encoders, the comparative analysis of multi-modal fusion strategies, and benchmarking against the established PORPOISE model [2]. This analysis demonstrates the significant impact of choosing the optimal image encoder on overall model performance. Additionally, it delves into the effectiveness of different fusion strategies in integrating image and tabular data, underscoring the synergy achieved through their combination. Lastly, by comparing the developed model's performance with the PORPOISE model, we underscore the advancements made in survival prediction accuracy, establishing the model's contribution to the field.

3.3.1 Image Feature Extractors

Three different image encoders were experimented: ResNet-50 architecture pretrained on ImageNet dataset ($\text{ResNet-50}_{\text{ImageNet}}$), CTransPath pretrained on TCGA (CTP_{TCGA}) and HistoSSL pretrained on TCGA ($\text{HistoSSL}_{\text{TCGA}}$). After extracting patch features, OViTANet was trained for OS and DFS on TCGA development set and tested on TCGA test set and Başkent dataset. Mean c-index of 5-fold cross-validation with 95% CI for each encoder is visualized in Figure 3.3.

In both survival tasks HistoSSL showed superior performance in TCGA test set, therefore it is selected to be used in further analyses. Mean c-index was 0.60 $\pm$ 0.02 and a maximum value reaching 0.64 for OS. Notably, OS prediction was not as good in the Başkent dataset as in TCGA dataset with a mean of 0.50 $\pm$ 0.02. However, for DFS prediction, HistoSSL ranked first in both TCGA and Başkent test sets with c-indices of 0.59 $\pm$ 0.01 and 0.54 $\pm$ 0.03, respectively. CTransPath showed consistent but lower performance on both TCGA and Başkent test sets with c-indices of 0.54 $\pm$ 0.02, 0.53 $\pm$ 0.02 in OS prediction and 0.52 $\pm$ 0.03 and 0.51 $\pm$ 0.03 in DFS prediction for TCGA and Başkent test sets, respectively. Lastly, ResNet-50 exhibited similar results with

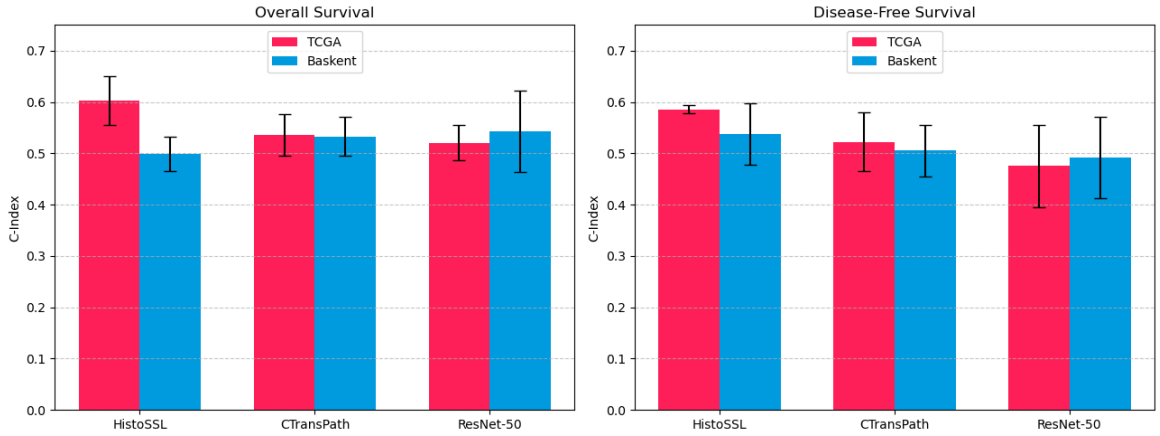


Figure 3.3 Performance of Image Encoders on Test Datasets. The bar chart illustrates the average concordance index and the 95% confidence interval for predictions of overall survival (on the left) and disease-free survival (on the right) across the TCGA test set and Başkent dataset.

CTransPath for OS prediction with c-indices of 0.52 ± 0.02 and 0.54 ± 0.04 in TCGA and Başkent datasets, respectively but it fell behind others for DFS prediction with c-indices of 0.47 ± 0.04 and 0.49 ± 0.04 in both TCGA and Başkent, respectively.

3.3.2 Multi-Modal Fusion Results

Every combination of the feature sets selected by the continuous-time survival model was fused with the image features extracted by pretrained HistoSSL model [1] on different levels using different fusion techniques. A total of 693 runs resulted in a wide range of c-indices from 0.44 to 0.75 in OS prediction and from 0.38 to 0.63 in DFS prediction. For each data category, resuts are shown in Figures 3.4 and 3.5.

In the Large dataset category, a decline in performance was noted for CNV and DNAm data, while clinical variables consistently emerged as the best-performing tabular data in OS prediction across all fusion strategies. The most effective fusion approach was identified as early concatenation, achieving a test c-index of 0.67. Conversely, for DFS prediction, no single data type distinctly outperformed others, with the highest c-index reaching only 0.58. The most promising fusion strategy for DFS was cross attention with CNV data, closely matched by mid concatenation of DNAm

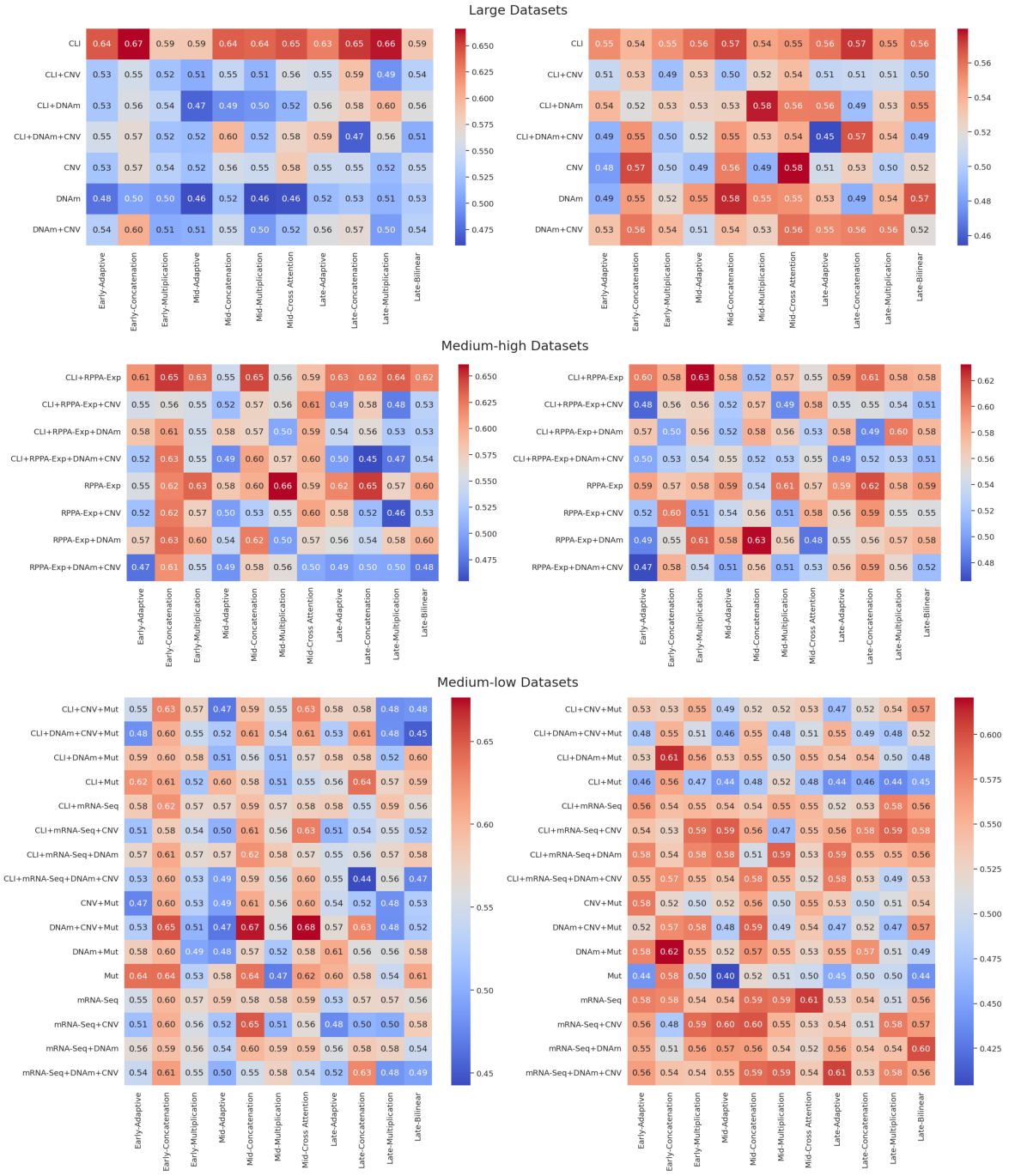


Figure 3.4 Heatmap of the Fusion Search Results for Large and Medium Data Categories. Test concordance indices are shown for both overall survival (on the left) and disease-free survival (on the right). Each row represents the tabular feature that were fused with the patch features using strategies given in the columns.

and a mid multiplication strategy involving a combination of clinical and DNAm data, suggesting a lack of clear differentiation in fusion efficacy.

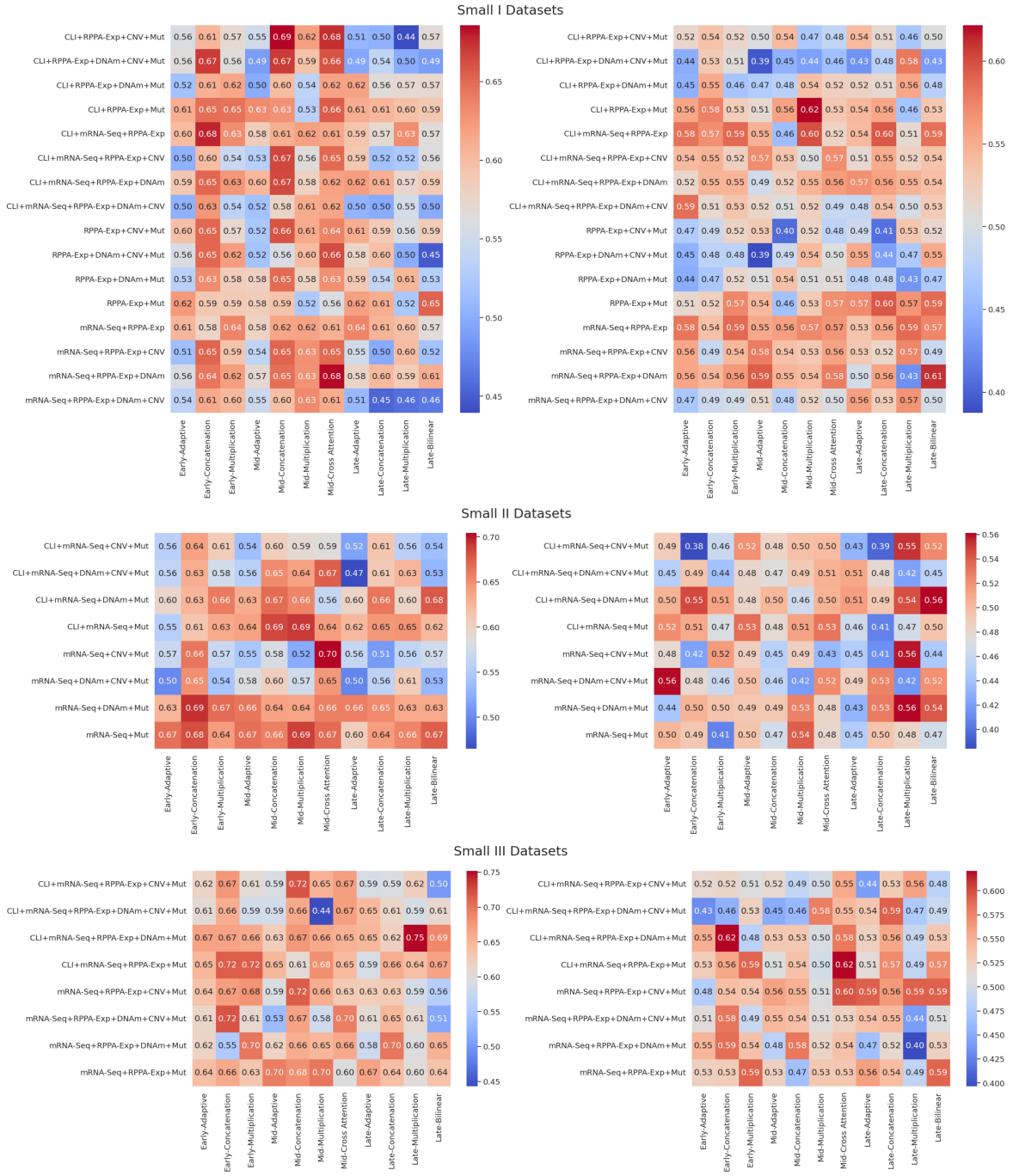


Figure 3.5 Heatmap of the Fusion Search Results for Small Data Categories. Test concordance indices are shown for both overall survival (on the left) and disease-free survival (on the right). Each row represents the tabular feature that were fused with the patch features using strategies given in the columns.

The highest performance in OS prediction was seen among Medium-high datasets when RPPA-Exp data was fused with image features using multiplication at the mid stage, yielding a test c-index of 0.66. This specific fusion method, however, did not

translate well to other data combinations. In DFS prediction, early multiplication of clinical and RPPA-Exp data slightly outperformed mid concatenation of DNAm and RPPA-Exp data with patch features, indicating nuanced differences in fusion effectiveness.

Table 3.3
This table presents the average test concordance index across various fusion techniques for predicting overall survival in each data category.

Location	Fusion	Large	Medium High	Medium Low	Small I	Small II	Small III
Early	Adaptive	0.5422	0.5486	0.5516	0.5607	0.5786	0.6316
	Concatenation	**0.5750**	**0.6162**	**0.6095**	0.6315	**0.6502**	0.6646
	Multiplication	0.5317	0.5784	0.5463	0.5972	0.6126	0.6489
Mid	Adaptive	0.5120	0.5288	0.5243	0.5530	0.6032	0.6118
	Concatenation	0.5579	0.5896	0.6009	0.6301	0.6371	**0.6733**
	Multiplication	0.5256	0.5577	0.5459	0.5931	0.6247	0.6291
	Cross Attention	0.552	0.5811	0.5935	**0.6350**	0.6432	0.6534
Late	Adaptive	0.5664	0.5502	0.5519	0.5758	0.5662	0.6189
	Concatenation	0.5631	0.5532	0.5666	0.5568	0.6122	0.6387
	Multiplication	0.5505	0.5277	0.5322	0.5511	0.6110	0.6252
	Bilinear	0.5450	0.5532	0.5430	0.5506	0.5978	0.6032

For Medium-low datasets, the top OS prediction performance was achieved using cross-attention with a combination of DNAm, CNV, and Mut data, demonstrating a test c-index of 0.68. The best fusion strategy for DFS prediction in this category was early concatenation of DNAm and Mut data with patch features, resulting in a test c-index of 0.62.

In the Small I dataset category, early and mid concatenation, along with cross-attention, were effective fusion strategies for OS prediction, with mid concatenation of clinical, RPPA-Exp, CNV, and Mut data leading with a c-index of 0.69. For DFS prediction, mid multiplication of clinical, RPPA-Exp, and Mut data outperformed other strategies, achieving a c-index of 0.62.

Among Small II datasets, the combination of mRNA-Seq, CNV, and Mut data excelled with cross-attention for OS prediction, reaching a top c-index of 0.70, while strategies for DFS prediction showed lower performance, peaking at a c-index of 0.56 with bilinear fusion of clinical, mRNA-Seq, DNAm, and Mut data with imagery features.

Finally, the highest OS prediction performance was observed when combining all tabular data, excluding CNV, with late multiplication fusion of tabular and image features, attaining a test c-index of 0.75. For DFS prediction, early concatenation of the same tabular data with imagery features achieved the top performance with a c-index of 0.62, highlighting the strategic significance of fusion techniques and data combinations in enhancing predictive accuracy.

Table 3.4
This table presents the average test concordance index across various fusion techniques for predicting disease-free survival in each data category.

Location	Fusion	Large	Medium High	Medium Low	Small I	Small II	Small III
Early	Adaptive	0.5117	0.5260	0.5383	0.5141	0.4940	0.5117
	Concatenation	0.5447	0.5592	0.5525	0.5241	0.4791	0.5491
	Multiplication	0.5186	0.5662	0.5441	0.5300	0.4702	0.5330
Mid	Adaptive	0.5257	0.5491	0.5234	0.5132	0.4990	0.5154
	Concatenation	0.5438	0.5598	**0.5532**	0.5034	0.4752	0.5198
	Multiplication	0.5354	0.5428	0.5315	**0.5307**	0.4920	0.5200
	Cross Attention	**0.5534**	0.5463	0.5320	0.5247	0.4954	**0.5623**
Late	Adaptive	0.5250	0.5586	0.5297	0.5219	0.4668	0.5217
	Concatenation	0.5299	**0.5663**	0.5241	0.5237	0.4671	0.5527
	Multiplication	0.5310	0.5637	0.5219	0.5182	0.5002	0.4911
	Bilinear	0.5297	0.5517	0.5353	0.5266	**0.5007**	0.5375

Overall, analysis presented in Table 3.3 highlights that early concatenation emerges as a notably effective fusion strategy in the context of OS prediction. This is substantiated by its consistently higher mean c-index across the majority of data types and categories, with the exception of the Small I and III data categories. For these par-

ticular categories, cross attention and mid-level concatenation strategies demonstrated superior performance, achieving higher mean test c-indices, while strategies involving late fusion generally lagged in effectiveness.

Conversely, for the DFS prediction, the comparison of fusion strategies reveals a more uniform performance landscape. As indicated by the mean test c-indices in Table 3.4, no single fusion approach distinctly outperforms the others. Furthermore, the observed maximum mean c-index did not exceed 0.60, suggesting an overall lower predictive potential for DFS outcomes based on the current fusion strategies.

3.3.3 Comparative Analysis

In assessing the efficacy of tabular data combinations alongside fusion strategies through 5-fold cross-validation, HistoSSL image features were amalgamated with selected tabular features to predict OS and DFS.

According to the results detailed in Table 3.5, OViTANet consistently outperformed PORPOISE across all data categories for OS prediction. Specifically, in the integration of clinical variables, OViTANet achieved a test c-index of 0.6424 ± 0.0238, surpassing PORPOISE's 0.6289 ± 0.0044. The margin of difference was narrower in the Medium-high data category, registering 0.5991 ± 0.0369 for OViTANet against 0.5944 ± 0.0327 for PORPOISE. For the Medium-low group, a combination of Mut, CNV, and DNAm fused with cross-attention in OViTANet resulted in a c-index of 0.6204 ± 0.0413, compared to 0.5888 ± 0.0111 in PORPOISE. The Small I data category saw a modest improvement with OViTANet at 0.6463 ± 0.0273 versus 0.6382 ± 0.0183 in PORPOISE. Notably, in the smaller data categories, OViTANet demonstrated a more pronounced advantage, achieving c-indices of 0.6554 ± 0.0557 and 0.6902 ± 0.0499 in the Small II and III datasets, respectively, in contrast to 0.5984 ± 0.0313 and 0.6211 ± 0.0113 observed in PORPOISE.

For DFS prediction, OViTANet exhibited superior mean test c-indices across

Table 3.5
The table displays the 5-fold cross-validation results for overall survival prediction of the proposed model OViTANet and PORPOISE [2] with mean ± standard deviation of test concordance index. Image features were combined with the tabular data combinations using the fusion strategies on the table for OViTANet and bilinear fusion for PORPOISE models.

Category	Tabular Data	Fusion Strategy	OViTANet	PORPOISE
Large	Clinical	Early Concatenation	**0.6424 ± 0.0238**	0.6289 ± 0.0044
Medium-high	RPPA-Exp	Mid Multiplication	**0.5991 ± 0.0369**	0.5944 ± 0.0327
Medium-low	Mut, CNV, DNAm	Mid Cross Attention	**0.6204 ± 0.0413**	0.5888 ± 0.011
Small I	Cli, RPPA-Exp, Mut, CNV	Mid Concatenation	**0.6463 ± 0.0273**	0.6382 ± 0.0183
Small II	mRNA-Seq, Mut, CNV	Mid Cross Attention	**0.6554 ± 0.0557**	0.5984 ± 0.0313
Small III	Clinical, RPPA-Exp, mRNA-Seq, Mut, DNAm	Late Multiplication	**0.6902 ± 0.0499**	0.6211 ± 0.0113

nearly all data categories compared to PORPOISE, as highlighted in Table 3.5. Within the Large data category, OViTANet, integrating clinical and RPPA-Exp data with patch features via early multiplication, recorded a c-index of 0.5666 ± 0.0104, significantly outpacing PORPOISE's 0.5210 ± 0.0142. The difference was marginal in the Medium-high data category, with OViTANet at 0.5989 ± 0.0284 versus 0.5882 ± 0.0268 for PORPOISE. A fusion of CNV data with cross-attention in OViTANet yielded a lower performance, with a mean c-index of 0.5385 ± 0.0520, whereas PORPOISE attained 0.5670 ± 0.0183. In the Small I category, OViTANet showcased significantly better performance, achieving 0.5905 ± 0.0430 compared to PORPOISE's 0.5106 ± 0.0056, with only a slight edge observed in the Small II category for OViTANet with a c-index of 0.5181 ± 0.0458 against 0.5172 ± 0.0135 in PORPOISE. Contrarily, in the Small III dataset, PORPOISE performed more effectively, securing a c-index of 0.6293 ± 0.0209 versus 0.5288 ± 0.0676 by OViTANet.

Table 3.6
The table displays the 5-fold cross-validation results for disease-free survival prediction of the proposed model OViTANet and PORPOISE [2] with mean ± standard deviation of test concordance index. Image features were combined with the tabular data combinations using the fusion strategies on the table for OViTANet and bilinear fusion for PORPOISE models.

Category	**Tabular Data**	**Fusion Strategy**	**OViTANet**	**PORPOISE**
Large	Clinical, RPPA-Exp	Early Multiplication	$\mathbf{0.5666 \pm 0.0104}$	0.521 ± 0.0142
Medium-high	Clinical, RPPA-Exp, Mut	Mid Multiplication	$\mathbf{0.5989 \pm 0.0284}$	0.5882 ± 0.0268
Medium-low	CNV	Mid Cross Attention	0.5385 ± 0.052	$\mathbf{0.567 \pm 0.0183}$
Small I	Clinical, mRNA-Seq, RPPA-Exp, Mut	Mid Cross Attention	$\mathbf{0.5905 \pm 0.043}$	0.5106 ± 0.0056
Small II	Clinical, mRNA-Seq, DNAm, Mut	Late Bilinear	$\mathbf{0.5181 \pm 0.0458}$	0.5172 ± 0.0135
Small III	DNAm, Mut	Early Concatenation	0.5388 ± 0.0676	$\mathbf{0.6293 \pm 0.0209}$

4. DISCUSSION

4.1 Comparison of Selected Genetic Features with Literature

The process of feature selection stands as a pivotal component of this thesis, necessitated by the complex and high-dimensional nature of genetic data. Recognizing the intricacies inherent in genetics–a field marked by its sophisticated web of gene expressions, mutations, and their interactions–this study eschewed the approach of selecting features purely based on domain knowledge in favor of survival-specific statistical and neural network approaches. This decision was driven by the understanding that genetics requires a nuanced level of expertise for the effective identification of significant genes and mutations. Moreover, manual selection risks neglecting the subtle yet critical interactions between genetic factors, interactions that AI methods are uniquely equipped to uncover.

To ensure that our method is not only statistically relevant but also biologically meaningful, the comparison of the findings of the feature selection process against existing literature will be discussed in this section. This comparison encompasses various dimensions of genetic variations, including Signaling Pathways, Mutations, CNVs, DNA Methylation, and Protein Expressions. Through an AI-driven approach, this study elucidates the genetic and molecular landscapes pivotal for understanding the intricacies of ovarian cancer. This methodology not only corroborates with the established literature but also unveils novel insights into the disease's biological foundation, paving the way for targeted therapeutic strategies and enhanced prognostic models.

4.1.1 Signaling Pathways

For the pathway analysis, gene sets were retrieved from the Kyoto Encyclopedia of Genes and Genomes (KEGG) Database [58], specifically for pathways reported in

the literature such as PI3K/Akt/mTOR (map04151), JAK/STAT (map04630), Src (map04510), NF-κB (map04064), and LPA (map04072) [10]. Within a cohort of 312 patients with accessible mutation data, a minority of 20 patients exhibited no mutations in genes associated with the PI3K/Akt/mTOR pathway. The majority of mutations were identified in TP53, involving 274 patients, followed by BRCA1 mutations present in 11 patients. For OS prediction, none of the genes within this pathway were selected among the Mut data and only CDKN1B was chosen from mRNA-Seq data. Conversely, for DFS prediction, several genes including Akt1, Glucose-6-Phosphatase Catalytic Subunit (G6PC), Laminin Subunit Beta 3 (LAMB3), Serum/Glucocorticoid Regulated Kinase 3 (SGK3), BCL2 like protein 11 gene (BCL2L11), Fibroblast Growth Factor 1 (FGF1), and Artemin (ARTN) were selected from mRNA-Seq data, alongside CD19, Integrin Subunit Alpha 8 (ITGA8), and Nitric Oxide Synthase 3 (NOS3) from mutation data.

The comparative analysis of the JAK/STAT pathway did not identify any genes for OS prediction, despite the selection of genes such as CREB Binding Protein (CREBBP), STAT6, Interleukin 11 Receptor Alpha (IL11RA), and IL20RA from mutation data and IL20RB, IL11, IL13, IL15, and IL31RA from mRNA-Seq data for DFS prediction. This exclusion in the context of OS prediction may be attributed to the insufficient frequency of mutations, with CREBBP and Epidermal Growth Factor Receptor (EGFR) emerging as the most prevalent ones with occuring only in seven instances.

Similarly, genes associated with the Src pathway exhibited limited occurrence, with the RELN mutation identified in eight cases. Nevertheless, Myosin Light Chain 2 (MYL2) and SRC were selected from mRNA-Seq and mutation data, respectively, for OS prediction, while a broader array of genes, including Cell Division Cycle 42 (CDC42), Laminin Subunit Beta 3 (LAMB3), Epithelial Membrane Protein 1 (EMP1) (from mRNA-Seq data), and SRC, ITGA8, MYL2, Dedicator Of Cytokinesis 1 (DOCK1) (from Mut data), were identified for DFS prediction.

The LPA pathway mutations, predominantly KIT and EGFR, were noted in

seven cases, yet no genes were selected for OS prediction. Conversely, for DFS prediction, Arginine Vasopressin Receptor 1B (AVPR1B) and Glutamate Metabotropic Receptor 8 (GRM8) mutations were chosen from mRNA-Seq and mutation data.

Furthermore, mutations within the NF-κB pathway were comparatively rare, with Ataxia Telangiectasia Mutated (ATM), TNF Receptor Associated Factor 1 (TRAF1), and TNF Alpha Induced Protein 3 (TNFAIP3) mutations occurring in four instances. The ATM gene was selected for both OS and DFS prediction from mutation data. In the analysis of mRNA-Seq data for feature selection, only the IL1B gene was chosen for DFS prediction, with no selection made for OS prediction.

4.1.2 Mutations

In the study of SOC, extensive research has identified a plethora of significant mutations. Prominent among these are mutations in TP53, BRCA1, BRCA2, RB1, NF1, CSMD3, CDK12, and PTEN genes, which are frequently observed. Additionally, mutations in BRAF, PIK3CA, KRAS, NRAS, and ERBB2 are less common but noteworthy [14], particularly due to their prevalence in low-grade SOC [59]. Moreover, the expression of specific genes, including ABC1, ABC2, and GSH1, has been correlated with the progression of the disease and resistance to treatment [13]. The roles of tumor suppressor genes such as RB1, PTEN, NF1, and RAD51B [11], alongside mesenchymal genes like SNAIL, SLUG, and TWIST, have been implicated in fostering resistance to chemotherapy [13].

Within the TCGA dataset, mutations in TP53, BRCA1, BRCA2, RB1, NF1, CSMD3, CDK12, PTEN, BRAF, PIK3CA, KRAS, NRAS, ERBB2, and BRIP1 were documented. However, none of these mutations were selected in the feature selection phase for mutation data or mRNA-Seq analysis aimed at predicting OS. Interestingly, the TP53 binding protein-1 (TP53BP1) was identified as a significant feature in the mutation data. Moreover, RAD51, a gene integral to the homologous recombination and DNA repair processes [60], and CSMD3, which is hypothesized to play a role in

dendrite development and to be located in the plasma membrane [61], were selected for mRNA-Seq analysis in the prediction of DFS.

The feature selection methodology employed in this thesis identified several genes as significant, including some that, while not as prominently mentioned in the literature as others previously discussed, still play crucial roles. Mucin 20, cell surface associated gene (MUC20), was selected for both prediction tasks within the mRNA-Seq dataset, recognized for its potential to exacerbate the aggressive nature and metastatic capability of epithelial ovarian cancer cells [62]. Also chosen for OS prediction from the mRNA-Seq data were ATP Binding Cassette Subfamily A Member 13 (ABCA13) and Cyclin-Dependent Kinase Inhibitor 1B (CDKN1B). ABCA13 is associated with lower survival in metastatic SOC [63], while CDKN1B, linked to the p27Kip1 protein, correlates with ovarian cancer's poor prognosis and chemoresistance [64].

For the prediction of DFS, BCL2 Associated Athanogene 5 (BAG5), Transferrin Receptor (TFRC) and Mucin 4, Cell Surface Associated (MUC4) genes emerged as notable. The direct regulation of the BAG5 gene by miR-127-3p in epithelial ovarian cancer and the resultant mitigation of miR-127-3p's tumor-suppressive overexpression through BAG5 upregulation suggest that miR-127-3p acts as a tumor suppressor in epithelial ovarian cancer, specifically through BAG5 modulation [65]. TFRC, responsible for encoding the transferrin receptor (TFR1) involved in iron importation, is found to be elevated in high-grade SOC tissues. Decreasing intracellular iron levels has been shown to curb the proliferation of ovarian cancer tumor-initiating cells in vitro, as well as hinder tumor growth and the spread of tumor cells in vivo [66]. Moreover, MUC4 is a membrane-bound mucin protein, known for promoting tumorigenicity, aggressive behavior, and adverse outcomes across various epithelial carcinomas, including those of the pancreas, breast, colon, ovarian, and prostate [67].

In the exploration of genes selected from the mutation data, certain genes come into prominence with a literature search especially the ones selected for DFS prediction. These include B-Cell CLL/Lymphoma 9 (BCL9), linked to ovarian cancer metastasis [68]; Nitric Oxide Synthase 3 (NOS3), where allelic variation is associated with ad-

vanced tumor stages and positive lymph node involvement [69]; Receptor Tyrosine Kinase-Like Orphan Receptor 1 (ROR1) which influences ovarian cancer dissemination to the omentum [70]; and SET Domain Containing 2 (SETD2), also known as Hypoxia-Inducible Factor 1 [HIF-1]), which plays a crucial role in angiogenesis through Vascular Endothelial Growth Factor regulation, impacting ovarian cancer [71].

4.1.3 Copy Number Variation

To address the selected CNV features, it's essential to highlight findings that align with existing literature, particularly regarding gene amplification and deletion patterns. The analysis demonstrated that MECOM was the gene most frequently subjected to amplification, exhibiting homozygous amplification in 205 instances and heterozygous amplification in 264 cases. Additionally, a heterozygous deletion was observed in four cases, while 85 cases presented no alterations. Similarly, MYC gene was commonly amplified, albeit to a lesser extent compared to MECOM. 235 cases had homozygous amplification, 207 had heterozygous amplification, 91 were neutral, and 25 showed heterozygous deletion. Despite the prevalence of these alterations, neither gene was selected for OS or DFS prediction tasks. On the other hand the CCNE1 gene was selected for OS prediction despite of having less variations with homozygous amplification in 120 cases and heterozygous amplification in 193 cases, while 198 cases showed neutral amplification status and 47 cases exhibited heterozygous deletion.

The literature also highlights three significant tumor suppressor genes–PTEN, RB1, and NF1–subject to deletions. Within the TCGA dataset, NF1 deletions were the most frequent, with 424 heterozygous and 37 homozygous cases. RB1 deletions followed, with 306 heterozygous and 50 homozygous cases. PTEN deletions were observed in 217 cases, including 25 homozygous deletions. Notably, only RB1 gene was selected for OS prediction while others were not selected for either task.

Among the genes selected from the CNV data for both OS and DFS predictions, notable mentions include BRCA2, emphasizing the gene's potential role in the genetic

predisposition and progression of ovarian cancer. Furthermore, the list included Caudal Type Homeobox 2 (CDX2), which was recognized for its involvement in the proliferation, migration, and invasion of ovarian cancer cells[72]; Charged Multivesicular Body Protein 4C (CHMP4C), which has been highlighted as a potential diagnostic and therapeutic target [73]; and Zinc Finger Protein 671 (ZNF671) which was suggested as a biomarker for monitoring SOC recurrence after platinum-based adjuvant chemotherapy [74].

The feature selection method used in this thesis highlighted several other crucial genes, especially for OS prediction. Notably, Collagen Type 11 Alpha 2 chain (COL11A2), also known as PARP, emerged as a clinical target, particularly for patients with BRCA1/2 mutations or other deficiencies in the homologous recombination DNA repair pathway [75]. Genes linked to drug resistance, such as ATP-Binding Cassette super-family G member 2 (ABCG2) [76] and Annexin A3 (ANXA3) [77], were identified from CNV data for OS prediction. Additionally, genes associated with poor prognosis in ovarian cancer, including Klotho (KL) [78], SRY-Box Transcription Factor 18 (SOX18) [79], Sodium Channel Epithelial 1 Alpha Subunit (SCNN1A) [80], and ATPase Copper Transporting Beta (ATP7B) [81], were also highlighted. Furthermore, genes related to tumor spread and metastasis, such as Fatty Acid Binding Protein 4 (FABP4) [82], Fms Related Tyrosine Kinase 1 (FLT1) [83], Secreted Phosphoprotein 1 (SPP1) [84], AXL Receptor Tyrosine Kinase (AXL) [85], Testis Expressed 19 (TEX19) [86], and SERPINE1 [87], were selected for OS prediction. Lastly, The Erb-B2 Receptor Tyrosine Kinase 2 (ERBB2) gene, more commonly mutated in lower grades [13], and mismatch repair genes PMS2 and MutS Homolog 3 (MSH3) were also chosen from the CNV data, with the latter for DFS prediction and the others for OS prediction.

For DFS prediction, fewer genes were deemed significant, including the TUBB3 gene, indicative of aggressiveness in ovarian cancer [88]; MIR145, associated with cisplatin resistance through PD-L1 expression regulation [89]; and DCTN4, suggested as a prognostic marker and therapeutic target for metastasis prevention, recurrence, and drug resistance reversal in ovarian cancer [90].

4.1.4 DNA Methylation

In the present study, the efficacy of the employed feature selection method was evaluated by comparing identified features with epigenetically altered genes commonly reported in the literature, including genes like BRCA1, CDH2, RASSF1, and PTEN, which are known for hypermethylation, as well as ABCB1, TMEM88, SERPINE1, and VIM, associated with hypomethylation [14],[18]. Remarkably, none of these genes were selected for OS prediction. However, for DFS prediction, genes such as TMEM88, BRCA1, CDH2, and RGS10 were identified. Notably, TMEM88 exhibited significantly elevated methylation beta values, averaging 0.78 ± 0.20, in stark contrast to the lower values of BRCA1 (0.36 ± 0.20), CDH2 (0.02 ± 0.03), and RGS10 (0.03 ± 0.05), despite literature suggesting TMEM88's hypomethylation correlates with resistance to platinum-based chemotherapy and others' hypermethylation [91].

Moreover, the analysis revealed genes pivotal for OS prediction in ovarian cancer, including BRCA2; CD274, encoding the PD-L1 protein critical for tumor immune evasion [92]; and Alpha Kinase 2 (ALPK2), proposed as a potential therapeutic target [93]. The DFS prediction model encompassed a broader spectrum of genes implicated in ovarian cancer pathogenesis and progression. Noteworthy among these were FABP4, involved in metastasis and metabolic regulation within cancer cells [82]; Histone Deacetylase 3 (HDAC3), associated with cellular proliferation, invasion, and migration [94]; C-X-C motif chemokine receptor 4 (CXCR4), a contributor to cancer cell invasion and metastasis [95]; Basonuclin Zinc Finger Protein 2 (BNC2), influential in cell survival post oxidative stress [96]; and NOTCH1, essential for the maintenance of cancer stem cells [97]. Additional significant genes related to survival, including, Zinc Finger E-Box Binding Homeobox 1 (ZEB1)[98], Enhancer of Zeste Homolog 2 (EZH2)[99], Deleted in Liver Cancer 1 (DLC1)[100], SOX18[79], KL[78], Lamin A (LMNA)[101] and drug resistance, namely, Jagged Canonical Notch Ligand 1 (JAG1)[102] were also identified.

4.1.5 Protein Expressions

The selection process for features within RPPA-Exp data pinpointed a limited yet significant array of proteins for the prediction of OS. Notably, this selection emphasized proteins associated with the PI3K/Akt/mTOR signaling pathway, which is known to undergo alterations in ovarian cancer scenarios [10]. This includes the Akt protein, specifically when phosphorylated at Ser473, and the mTOR protein, phosphorylated at Ser2448. In addition to these, proteins pivotal in the mechanisms of tumorigenesis and tumor surveillance were identified. Among these are the Vascular Endothelial Growth Factor Receptor 2 (VEGFR2), which plays a critical role in angiogenesis [83]; Cyclin B1 (CCNB1), a regulator of cell cycle progression [103]; Heat Shock Protein 70 (HSP70), known for its role in apoptosis inhibition and its association with chemoresistance in ovarian cancer [104]; and the c-Met receptor tyrosine kinase, which is integral to cellular processes such as proliferation, survival, and migration [105]. Furthermore, the feature selection underscored the significance of N-Cadherin (CDH2), which is implicated in cell-cell adhesion and the epithelial-to-mesenchymal transition, correlating with tumor grade, distant metastasis, recurrence, and consequently, a poorer prognosis [106]. Additionally, SERPINE1 was highlighted as a crucial factor in tumor invasion and metastasis, with a particular focus on peritoneal metastasis in ovarian cancer [87].

Similar proteins were identified for the prediction of DFS as for OS prediction, including Akt, CCNB1, CDH2, HSP70, c-Met, mTOR, and SERPINE1. Additionally, this analysis highlighted proteins such as TP53, BRCA2, EGFR, ERBB2, MYC, PTEN, PARP1, RB1, SRC, STAT3, CCNE1, and CCNE2. Their roles in ovarian cancer have been discussed in preceding sections, underscoring their importance in the disease's pathophysiology. Moreover, proteins involved in the PI3K/Akt/mTOR and MAPK pathways were particularly emphasized for DFS prediction. These include not only Akt but also PI3K, TSC1, TSC2, Rictor, and mTOR from the PI3K/Akt/mTOR pathway, along with MEK1, ERK2, p38 MAPK, JNK, and RAF1 from the MAPK pathway. Additionally, proteins that regulate apoptosis were identified as key to DFS prediction. This group encompasses BAX and BIM, which facilitate cell death, and BCL-2 and BCL-xL, which prevent it, alongside specific caspases such as Caspase 7

and 8, highlighting the intricate balance between cell survival and death in ovarian cancer [107]. The selection also included Beclin, a protein associated with autophagy, and CDKN1B, both identified as risk factors for ovarian cancer prognosis [108],[19]. Furthermore, the Estrogen Receptor (ESR1) and Progesterone Receptor (PGR) proteins, known for their association with improved survival in epithelial ovarian cancer, were also identified [109].

4.2 Comparison of Image Encoders

The comparative analysis of image encoders–ResNet-50$_{ImageNet}$, CTransPath$_{TCGA}$, and HistoSSL$_{TCGA}$–revealed that HistoSSL$_{TCGA}$ outperformed the others in predicting both OS and DFS in the TCGA test set. However, this performance advantage was only reflected in the Başkent dataset for DFS prediction, not for OS prediction. While CTransPath$_{TCGA}$ displayed consistent performance across both datasets for either survival prediction, it did not match the predictive accuracy of HistoSSL$_{TCGA}$, except for OS prediction in Başkent. ResNet-50$_{ImageNet}$ showed comparable performance to CTransPath$_{TCGA}$ in OS prediction but was less effective in DFS prediction.

These findings prompt a deeper examination of the factors contributing to the superior performance of HistoSSL$_{TCGA}$. One notable aspect is the domain-specific pretraining of HistoSSL$_{TCGA}$ on the TCGA dataset, which likely enables the encoder to capture nuanced, clinically relevant features that are pivotal for accurate survival predictions. This underscores the importance of leveraging domain-specific knowledge in the development of machine learning models for clinical applications. The diminished performance of HistoSSL$_{TCGA}$ in the Başkent dataset for OS prediction, compared to the TCGA test set, also suggests a potential variability in the encoder's effectiveness across different populations or datasets. This variability may be attributed to differences in dataset characteristics, such as image quality, staining protocols, or demographic variations, highlighting the need for robust models that can generalize across diverse clinical settings.

Furthermore, the consistent but lower performance of CTransPath$_{TCGA}$ across both tasks and datasets suggests that while this encoder is capable of capturing relevant features for survival prediction, it may lack the specificity or depth of feature extraction provided by HistoSSL$_{TCGA}$. This could point to the potential benefits of further optimizing encoder architectures or training strategies to enhance their predictive capabilities.

The comparative underperformance of ResNet-50$_{ImageNet}$, especially in DFS prediction, emphasizes the limitations of using general-purpose image encoders for specialized medical imaging tasks. This highlights the critical need for specialized, task-specific model training or fine-tuning to improve performance in clinical prediction tasks.

In conclusion, this study's findings advocate for the integration of domain-specific pretraining and the exploration of encoder architectures tailored to the unique demands of medical imaging tasks. The superior performance of HistoSSL$_{TCGA}$ not only demonstrates the value of specialized pretraining but also sets a benchmark for future research aimed at enhancing the predictive accuracy and generalizability of machine learning models in oncology.

4.3 Efficacy of Fusion Techniques

The exploration of multi-modal fusion strategies in this study provides insightful revelations into the efficacy of integrating diverse data types for oncological survival prediction. The methodologies encompassed three distinct fusion locations (early, mid, and late) and five fusion methods (concatenation, multiplication, adaptive learning, cross-attention for mid-fusion, and bilinear for late fusion). The evaluation spanned across various data categories with differing sizes (Large, Medium-high, Medium-low, Small I, Small II, Small III) for both OS and DFS prediction.

The analysis underscored early concatenation as a particularly potent fusion

strategy for OS prediction evident by the average c-indices for all data combinations as shown in Table 3.3. This method's success can be attributed to its ability to preserve original feature representations before any substantial model-specific transformations occur. By combining features at an early stage, the model can exploit the raw, complementary information from multiple modalities, enhancing its ability to identify nuanced, predictive patterns. This strategy's effectiveness was consistent across most data categories, save for Small I and III, where cross-attention and mid-level concatenation outperformed others.

The cross-attention fusion strategy's effectiveness is partly due to its sophisticated mechanism of concatenating keys and values within the multi-head attention framework, while queries are derived exclusively from the image modality. This specific configuration allows the model to direct its attention towards integrating complementary information from non-image modalities, enriching the image-derived queries with a broader contextual understanding. The effect of this approach is a more nuanced and contextually informed prediction model. By focusing the queries on image data, the model leverages the rich, intricate details available in images, while the concatenated keys and values from other modalities introduce additional, relevant information that may not be directly observable in the image data. This method enhances the model's ability to discern subtle, predictive patterns across modalities, leading to improved accuracy in survival predictions by effectively balancing the detailed visual information with complementary data types.

Conversely, the DFS prediction scenario presented a more uniform distribution of performance across fusion strategies, with no singular approach markedly outperforming others. This parity suggests a nuanced challenge in DFS prediction, where the complexity of disease recurrence patterns may not be fully captured by the current fusion methodologies. The observed ceiling in predictive performance, as seen in Figure 3.4, indicates potential limitations in the existing fusion strategies' ability to capture and integrate predictive signals for DFS outcomes effectively.

The relative underperformance of bilinear fusion, despite its success in the POR-

POISE model [2], particularly highlights the complexities inherent in multi-modal fusion for survival prediction. Bilinear fusion's mathematical intricacy allows for the interaction of features across modalities, theoretically enabling a rich representation of combined feature spaces. However, its limited success, except in the DFS prediction for the Small II dataset, suggests that such complexity might not always translate to better predictive performance. This could be due to the overfitting risk or the challenge in optimally tuning such models to exploit the nuanced interactions between modalities effectively.

Similarly, the lack of success with adaptive learning strategies, which aim to optimize the contribution of each modality through a weighted sum, raises questions about the adaptability of such methods to the specific challenges of survival prediction. The potential reasons for this shortfall might include the difficulty in learning optimal weights in the presence of complex, non-linear relationships between modalities and survival outcomes. Furthermore, the adaptive approach's reliance on a predefined structure for weight adjustment might limit its flexibility in capturing more dynamic, context-dependent interactions between modalities.

In sum, the differential success of these fusion strategies illuminates the critical importance of selecting an appropriate fusion methodology that aligns with the data characteristics and the specific predictive task. The superior performance of early concatenation for OS prediction across multiple data categories underscores the value of leveraging raw, complementary information from diverse modalities. Meanwhile, the uniform performance landscape for DFS prediction suggests a need for novel strategies or enhancements to current methodologies to better capture the complexities of disease recurrence patterns. This study's findings emphasize the nuanced interplay between fusion strategy, data category size, and prediction task, offering a roadmap for future research to refine and advance multi-modal fusion approaches in clinical oncology.

4.4 Benchmarking Analysis

The comparative analysis between OViTANet and PORPOISE, two multi-modal survival prediction models, reveals significant insights into the efficacy of integrating tabular data with image features for oncological prognosis. Through a meticulous 5-fold cross-validation process, the study examined the performance of both models across various data categories for predicting OS and DFS, utilizing HistoSSL image features combined with selected tabular features.

For OS prediction, OViTANet consistently outperformed PORPOISE across all data categories, showcasing its superior ability to leverage multi-modal data for survival analysis. The integration of clinical variables with OViTANet achieved a notably higher test c-index than PORPOISE, indicating its enhanced capability in synthesizing and extracting meaningful patterns from clinical data alongside image features. This advantage was particularly evident in the smaller data categories, where OViTANet demonstrated a pronounced superiority, suggesting its effectiveness in handling datasets with limited samples through its advanced fusion strategies, such as cross-attention, which allows for a more nuanced and adaptive integration of multimodal data.

In the realm of DFS prediction, OViTANet also exhibited superior mean test c-indices across nearly all data categories when compared to PORPOISE. The marked difference in the Large data category, where OViTANet integrated clinical and RPPA-Exp data with early multiplication fusion, underscores the model's adeptness at combining disparate data types to improve predictive accuracy. However, it's noteworthy that in specific categories, such as Medium-high and Small III, the performance differences between OViTANet and PORPOISE were marginal or favored PORPOISE, indicating potential areas for further refinement in OViTANet's fusion and modeling strategies.

The divergent performances of OViTANet and PORPOISE across different data categories and prediction tasks underscore the complexity of multi-modal fusion in survival prediction. OViTANet's overall superior performance can be attributed to several

key technological and methodological advancements integrated within its framework. These enhancements not only bolster the model's predictive accuracy but also underscore the importance of tailored approaches in the development of cancer-specific prognostic tools.

Firstly, the integration of ViT within OViTANet represents a significant leap forward in leveraging deep learning architectures for image feature extraction. Unlike the gated attention mechanism used in PORPOISE, which has become somewhat outdated, ViT harnesses the power of self-attention mechanisms to process images. This approach allows for a more nuanced understanding of spatial hierarchies within histopathological images, enabling OViTANet to capture complex patterns and interactions that are indicative of survival outcomes. The self-attention mechanism in ViT facilitates a dynamic focus on relevant image regions, enhancing the model's ability to discern prognostically significant features from histopathology slides.

Moreover, OViTANet's flexibility in experimenting with different fusion strategies is pivotal to its success. By tailoring fusion methods to the specific characteristics of the data type, OViTANet optimizes the integration of multimodal data, including clinical variables and image features. This contrasts with PORPOISE's reliance on bilinear fusion, a method that, despite its potential to capture interactions between modalities, may not be ideally suited to all data types. Bilinear fusion can be too complex for some datasets, introducing unnecessary parameters and potentially leading to overfitting, or too simplistic for others, failing to capture the depth of interactions between modalities. OViTANet's adaptive use of fusion strategies, such as cross-attention and early concatenation, allows for a more nuanced and effective synthesis of multimodal data, contributing to its enhanced predictive performance.

The specificity of OViTANet's design for ovarian cancer also plays a crucial role in its efficacy. Unlike PORPOISE, which was developed as a pan-cancer model, OViTANet is tailored to the unique clinical and molecular landscape of ovarian cancer. This specialization is critical, given the generally shorter survival times and higher mortality rates associated with ovarian cancer. By focusing on the specific prognos-

tic factors and treatment outcomes relevant to ovarian cancer, OViTANet can offer more accurate and clinically relevant predictions. This specificity enables the model to incorporate ovarian cancer-specific features into its predictions, which can be particularly advantageous for identifying subtle prognostic indicators that are unique to this malignancy.

In summary, OViTANet's outperformance of PORPOISE can be attributed to its advanced image processing capabilities, flexible and data-type-specific fusion strategies, and targeted design for ovarian cancer. These factors collectively enhance the model's ability to provide precise and meaningful survival predictions, demonstrating the potential of specialized, multi-modal fusion models in the domain of cancer prognosis.

4.5 Limitations

The study presents several notable limitations that warrant discussion, each contributing to the context within which the findings should be interpreted.

Firstly, the application of feature selection algorithms to identify the optimal combination of clinical and genetic features for integration with image data, while methodologically sound, may have inadvertently led to the loss of significant prognostic signals. This is particularly concerning given the potential omission of critical genes or proteins directly related to survival outcomes. Despite the use of several algorithms, the similar test c-indices reported for each method, as illustrated in Figure A.3, suggest that the feature selection process may not have effectively discriminated between clinically relevant and less pertinent genes. This limitation underscores the potential value of incorporating domain knowledge into the feature selection process to ensure the retention of significant biological markers.

Secondly, the decision to utilize HistoSSL as the image encoder, based on its superior performance in the TCGA test set, is challenged by its limited efficacy in

the Başkent dataset, especially for OS prediction. This limitation highlights a potential lack of generalizability, potentially attributable to the model's pretraining on the TCGA dataset. Although this pretraining involved unlabeled FFPE slides, the risk of overfitting to the specific characteristics of the TCGA dataset cannot be discounted. Conversely, the relatively stable performance of CTransPath across both datasets, despite also being pretrained on TCGA, points to varying levels of generalizability and performance among models, suggesting a need for broader exploration of self-supervised models pretrained on diverse histopathological image datasets.

The absence of external validation for OViTANet further constrains the study's conclusions. The scarcity of publicly available genetic and histopathological data for ovarian cancer, compounded by the high costs associated with acquiring such data (e.g., mRNA sequencing or whole-exome sequencing), presents a substantial barrier to evaluating the model's reliability across different data distributions. This limitation highlights the challenges inherent in conducting comprehensive validation studies in the field of oncological research, where access to diverse datasets is crucial for assessing model generalizability and reliability.

Lastly, the benchmarking phase of this study was limited by my own challenges in adapting other models for a comprehensive comparative analysis. The process of ensuring that inputs were processed in a manner consistent with our model posed a significant challenge, especially when faced with models implemented in different programming languages or those documented with less clarity. This limitation is a reflection of the steep learning curve and technical barriers that can arise when attempting to integrate and compare complex models from diverse sources. Recognizing this, it becomes clear that enhancing my skills in model adaptation and seeking collaborative opportunities for knowledge exchange could greatly contribute to overcoming these hurdles. This experience has underscored the importance of continuous learning and adaptability in the rapidly evolving field of computational research.

In summary, while the study contributes valuable insights into the efficacy of multi-modal fusion strategies for oncological survival prediction, these limitations high-

light areas for future research and methodological refinement. Addressing these challenges through the incorporation of domain knowledge, exploration of alternative models, external validation, and improved documentation practices will be critical for advancing the field and enhancing the reliability and generalizability of predictive models like OViTANet.

5. CONCLUSION

In conclusion, this thesis has contributed significant insights into the potential of multi-modal fusion strategies to enhance oncological survival predictions, with a particular focus on ovarian cancer. Through comprehensive experimentation and analysis, it has been demonstrated that the integration of diverse data types–ranging from histopathological images to clinical and genetic features–can substantially improve the predictive accuracy of survival models. The development and evaluation of OViTANet, in comparison to the existing PORPOISE model, underscore the advancements in image processing and data fusion techniques, highlighting the importance of model adaptability and specificity to the cancer type in question.

OViTANet's superior performance across various data categories for both OS and DFS predictions can be attributed to its innovative use of the ViT for patch aggregation and its flexible approach to fusion strategies. This adaptability allowed for more effective integration of multi-modal data, tailored to the specific characteristics of ovarian cancer, thereby enhancing the model's prognostic capabilities. Furthermore, the selection of HistoSSL as the image encoder, despite its limitations in generalizability across different datasets, represents a pivotal step towards understanding the impact of domain-specific pretraining on model performance.

The study's limitations, including the challenges in feature selection and external validation, as well as the difficulties encountered in adapting and benchmarking against other models, serve as valuable lessons for future research. They highlight the importance of domain knowledge in feature selection, the need for broadening the scope of model comparison, and the necessity for continued development of skills in model adaptation.

Future directions for this research include exploring alternative self-supervised learning models, enhancing the external validation process to improve model reliability

across different data distributions, and incorporating domain expertise more explicitly in the feature selection process. Additionally, fostering collaborations and adopting standardized practices for documentation and model sharing could alleviate some of the challenges faced in model adaptation for benchmarking purposes.

This thesis not only advances the field of computational oncology by introducing a more effective model for survival prediction but also sets the stage for future work that could further refine and expand the capabilities of multi-modal fusion strategies in medical research. The insights gained from this study underscore the potential for such models to contribute to personalized medicine, ultimately aiding in the development of targeted treatment strategies and improving patient outcomes.

APPENDIX A. Feature Selection

A.1 Statistical Methods

The application of statistical methods for feature selection in the dataset led to the identification of distinct feature sets. Using 18 clinical features 14 feature sets were defined with a minimum number of 2 (11%) and a maximum of 17 (94%). The CNV dataset exhibited the largest number of features at 24,765 genes. Despite none displaying low variance, a vast majority were found to be collinear. This led to a significant reduction to 184 (0.7%) genes post multi-collinearity reduction. Only a modest fraction, 2592 (10.5%), were deemed significant by the log-rank test, and 195 genes (0.8%) were identified using the CoxPH model with high regularization. The RPPA-Exp dataset followed a similar trend, lacking any low-variance features. Post multi-collinearity reduction, 191 features (94%) remained, and the log-rank test ascertained 24 (12%) proteins as significant. The CoxPH model elucidated feature sets with 160 (78%) and 32 (16%) proteins under intermediate and high regularization, respectively. Mutation data were substantially impacted by the variance threshold, with only 672 (8%) genes retained, reflecting the sparsity of mutations. Multi-collinearity reduction was also effective, narrowing the field to 2,133 (24%) genes. The feature sets determined by the log-rank test and the CoxPH model comprised 844 (10%) and 380 (4%) genes, respectively. In contrast, the mRNA-Seq dataset was less affected by variance and collinearity thresholds, retaining 19,840 (97%) and 14,103 (69%) genes, respectively. However, the log-rank test and $\text{CoxPH}_{\text{high}}$ selected only 1,176 (6%) and 223 (1%) genes, respectively. Finally, DNAm data displayed a high degree of low variance, remaining 4385 (30%) genes. Collinearity was also prevalent, resulting in approximately half of the genes being discarded, leaving 7,876 (55%) genes subsequent to multi-collinearity reduction. The log-rank test identified 2194 (15%) genes, and the CoxPH model discerned 182 (1%) genes as significant.

Table A.1
The table displays the number of features retained after applying various feature selection methods and their combinations for OS prediction. The methods include variance threshold (VarThr), multi-collinearity reduction (Collin), log-rank test (LR), and Cox proportional hazards model with varying levels of regularization: low ($\text{CoxPH}_{\text{low}}$), intermediate ($\text{CoxPH}_{\text{int}}$), and high ($\text{CoxPH}_{\text{high}}$). Features chosen for each data category are highlighted in bold.

Method	**Clinical**	**CNV**	**Mut**	**mRNA-Seq**	**DNAm**	**RPPA-Exp**
All	18	24765	8765	20515	14373	204
VarThr	17	-	672	19840	4385	-
Collin	14	184	2133	14103	7876	191
LR	4	**2592**	844	1176	2194	24
$\text{CoxPH}_{\text{low}}$	17	-	-	-	-	-
$\text{CoxPH}_{\text{int}}$	14	-	-	-	-	160
$\text{CoxPH}_{\text{high}}$	6	195	380	223	182	32
VarThr+Collin	13	-	555	13602	3656	-
VarThr+LR	-	-	37	1160	330	-
Collin+LR	**2**	19	88	803	719	23
VarThr+$\text{CoxPH}_{\text{low}}$	16	-	-	-	-	-
VarThr+$\text{CoxPH}_{\text{int}}$	13	-	-	-	-	-
VarThr+$\text{CoxPH}_{\text{high}}$	-	-	109	**223**	125	-
Collin+$\text{CoxPH}_{\text{low}}$	-	180	-	-	-	188
Collin+$\text{CoxPH}_{\text{int}}$	13	158	-	-	-	154
Collin+$\text{CoxPH}_{\text{high}}$	4	27	161	198	169	32
LR+$\text{CoxPH}_{\text{low}}$	-	-	-	-	-	23
LR+$\text{CoxPH}_{\text{int}}$	-	475	-	-	-	21
LR+$\text{CoxPH}_{\text{high}}$	-	94	267	128	96	13
VarThr+Collin+LR	-	-	32	800	228	-
VarThr+Collin+$\text{CoxPH}_{\text{int}}$	12	-	-	-	-	-
VarThr+Collin+$\text{CoxPH}_{\text{high}}$	-	-	102	200	116	-
VarThr+LR+$\text{CoxPH}_{\text{int}}$	-	-	-	-	266	-
VarThr+LR+$\text{CoxPH}_{\text{high}}$	-	-	**35**	117	64	-
Collin+LR+$\text{CoxPH}_{\text{int}}$	-	-	-	-	-	**22**
Collin+LR+$\text{CoxPH}_{\text{high}}$	-	13	68	107	79	13
VarThr+Collin+LR+$\text{CoxPH}_{\text{low}}$	-	-	-	-	225	-
VarThr+Collin+LR+$\text{CoxPH}_{\text{int}}$	-	-	-	-	192	-
VarThr+Collin+LR+$\text{CoxPH}_{\text{high}}$	-	-	-	105	**58**	-

Table A.2
The table displays the number of features retained after applying various feature selection methods and their combinations for DFS prediction. The methods include variance threshold (VarThr), multi-collinearity reduction (Collin), log-rank test (LR), and Cox proportional hazards model with varying levels of regularization: low ($\text{CoxPH}_{\text{low}}$), intermediate ($\text{CoxPH}_{\text{int}}$), and high ($\text{CoxPH}_{\text{high}}$). Features chosen for each data category are highlighted in bold.

Method	**Clinical**	**CNV**	**Mut**	**mRNA-Seq**	**DNAm**	**RPPA-Exp**
All	18	24765	8765	20515	14373	204
VarThr	17	-	1141	19824	4368	-
Collin	14	187	2703	13785	7880	188
LR	5	1373	739	1005	**865**	19
$\text{CoxPH}_{\text{low}}$	-	-	-	-	-	-
$\text{CoxPH}_{\text{int}}$	-	-	-	-	-	**167**
$\text{CoxPH}_{\text{high}}$	6	288	**397**	224	241	47
VarThr+Collin	13	-	740	13291	3653	-
VarThr+LR	4	-	97	970	241	-
Collin+LR	4	9	81	**666**	497	18
VarThr+$\text{CoxPH}_{\text{low}}$	14	-	-	-	-	-
VarThr+$\text{CoxPH}_{\text{int}}$	11	-	-	-	-	-
VarThr+$\text{CoxPH}_{\text{high}}$	-	-	175	227	182	-
Collin+$\text{CoxPH}_{\text{low}}$	13	185	-	-	-	-
Collin+$\text{CoxPH}_{\text{int}}$	-	160	-	-	-	156
Collin+$\text{CoxPH}_{\text{high}}$	-	33	156	210	223	-
LR+$\text{CoxPH}_{\text{low}}$	-	-	-	-	-	18
LR+$\text{CoxPH}_{\text{int}}$	-	**434**	-	-	-	17
LR+$\text{CoxPH}_{\text{high}}$	-	72	337	131	103	11
VarThr+Collin+LR	3	-	60	656	207	-
VarThr+Collin+$\text{CoxPH}_{\text{low}}$	12	-	-	-	-	-
VarThr+Collin+$\text{CoxPH}_{\text{int}}$	**10**	-	-	-	-	-
VarThr+Collin+$\text{CoxPH}_{\text{high}}$	6	-	148	216	151	-
VarThr+LR+$\text{CoxPH}_{\text{low}}$	-	-	-	-	234	-
VarThr+LR+$\text{CoxPH}_{\text{int}}$	-	-	-	-	197	-
VarThr+LR+$\text{CoxPH}_{\text{high}}$	-	-	72	129	63	-
Collin+LR+$\text{CoxPH}_{\text{low}}$	-	-	-	-	-	-
Collin+LR+$\text{CoxPH}_{\text{int}}$	-	7	-	-	-	17
Collin+LR+$\text{CoxPH}_{\text{high}}$	-	5	64	117	84	-
VarThr+Collin+LR+$\text{CoxPH}_{\text{low}}$	-	-	-	-	205	-
VarThr+Collin+LR+$\text{CoxPH}_{\text{int}}$	-	-	-	-	176	-
VarThr+Collin+LR+$\text{CoxPH}_{\text{high}}$	-	-	51	115	60	-

A.1.1 Analysis of the Clinical Features

This section presents a comprehensive examination of the outcomes derived from the statistical feature selection process, focusing on clinical variables. Through this analytical procedure, an array of clinical variables was meticulously evaluated to identify those with significant predictive value.

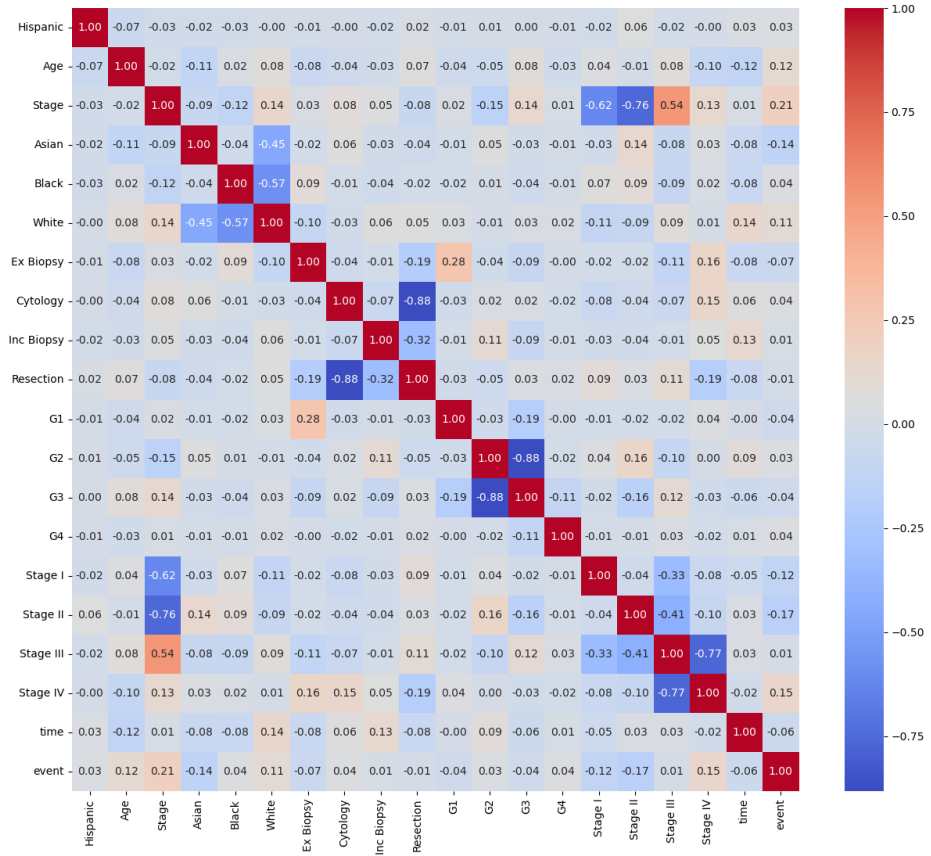


Figure A.1 Heatmap of the Correlation Matrix of the Clinical Features. Pearson's correlation coefficient values are shown in the figure for each pair of clinical features as well as the overall survival months and exitus status.

A.1.1.1 Correlation. The analysis identified several pairs of closely correlated clinical variables, such as clinical stage II with binary stage, stage III with stage IV, tumor resection with cytology, and G2 with G3, showcasing negative correlations rang-

ing from -0.76 to -0.88. In instances where variables were highly correlated, the selection process favored those with a weaker correlation to survival months for removal, ensuring a more robust feature set for survival analysis. Intriguingly, no clinical variable demonstrated a strong correlation with survival months, with 'White' race showing the highest absolute correlation of 0.14. Likewise, the binary clinical stage, though the most significantly correlated with exitus status, presented a modest correlation coefficient of 0.21.

Table A.3
Log-rank test p-values for various clinical features are given for OS and DFS prediction. Significant p-values < 0.05 are bolded.

Clinical Feature	**OS**	**DFS**
Hispanic	0.8400	**0.0303**
Age	**0.0381**	0.1845
Binary Stage	**0.0047**	**0.0006**
Race - Asian	0.4077	0.9689
Race - Black	0.0645	0.9866
Race - White	0.3592	0.6550
Biopsy - Excisional	0.5129	0.5105
Biopsy - Cytology	0.6483	0.2032
Biopsy - Incisional	0.1584	0.6352
Biopsy - Resection	0.2851	0.1771
G1	0.5828	0.8173
G2	0.3421	0.1075
G3	0.6594	0.0969
G4	0.6658	$<$ **0.0001**
Clinical Stage I	0.2603	**0.0046**
Clinical Stage II	**0.0094**	**0.0338**
Clinical Stage III	0.8826	0.2278
Clinical Stage IV	**0.0206**	0.0834

A.1.1.2 Univariate Analysis. Further examination through univariate analysis revealed significant associations between survival outcomes and variables such as age, binary stage, stage II, and stage IV, with respective p-values indicating their statistical significance. The visualization of these relationships through Kaplan-Meier survival

curves, as illustrated in Figure A.2, highlighted the differential impact of these variables on survival probabilities over time. Remarkably, lower age groups exhibited a more rapid decline in survival probabilities compared to their older counterparts. In an unexpected twist, the analysis also found that patients with higher clinical stages displayed longer survival trajectories than those with lower stages, challenging conventional expectations and underscoring the complexity of survival dynamics in ovarian cancer.

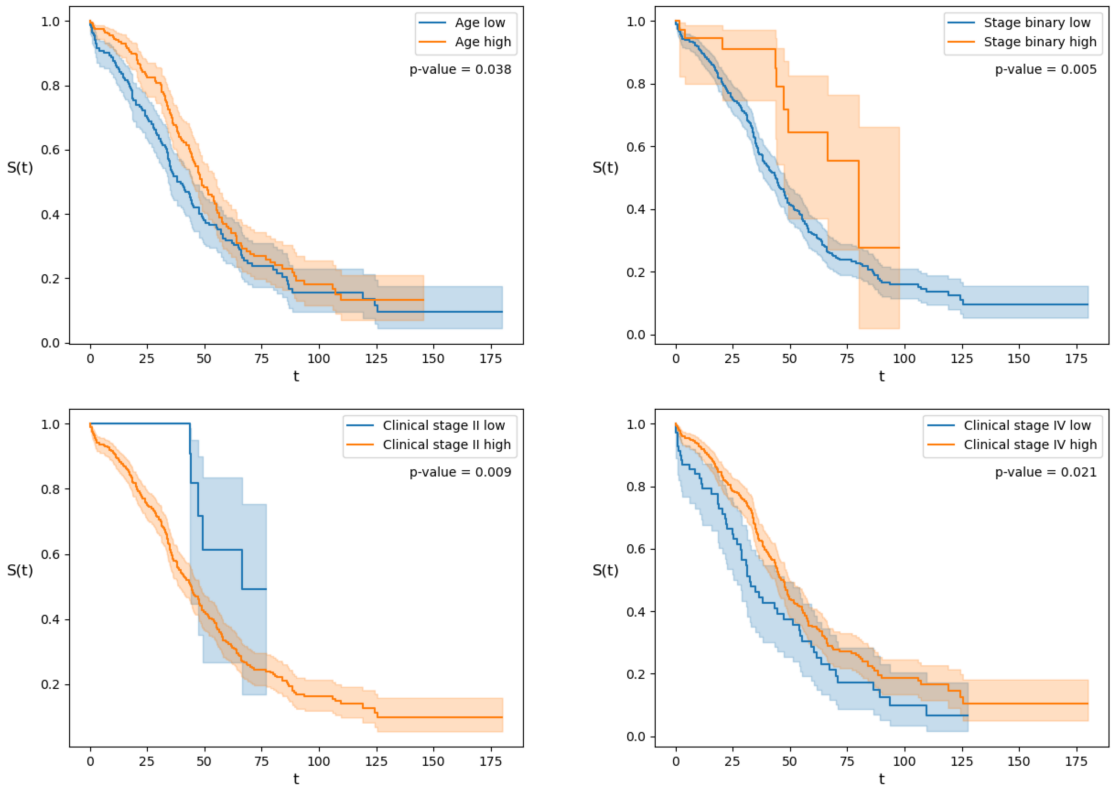


Figure A.2 Kaplan-Meier Survival Curves for Clinically Significant Variables. This figure presents four Kaplan-Meier curves, each representing the survival function $S(t)$ over time t for different clinical variables identified as significant in the log-rank test. Each graph displays the survival estimates for the two groups, illustrating the differences in survival probabilities over time.

A.1.1.3 Multivariate Analysis. The multivariate analysis, conducted on the clinical data using the CoxPH model, explored the effects of varying levels of regularization–low, intermediate, and high–corresponding to α values of 0.001, 0.01, and 0.1, respectively. At the lowest level of regularization, only clinical stage I was found to be non-contributory and was thus excluded from the model. When the regularization was

adjusted to an intermediate level, additional variables including ethnicity, cytology, and clinical stages I and III were determined to have zero coefficients and were therefore not included in the predictive model. A further increase in regularization to a high level refined the model to include only six features which were age, binary stage, Black race, incisional biopsy, and clinical stages II and IV.

Table A.4
The outcomes of the multivariate feature selection using Cox's proportional hazards model with an elastic net penalty are displayed for Overall (OS) and Disease-free (DFS) Survival predictions. Features with zero coefficients are bolded for clarity across different α values, signifying their exclusion from the feature set.

Clinical Variables	**OS**			**DFS**
	$\alpha = 0.001$	$\alpha = 0.01$	$\alpha = 0.1$	$\alpha = 0.1$
Hispanic	-0.0088	**0.000**	**0.000**	0.0331
Age	0.2603	0.2470	0.1367	0.0380
Binary Stage	0.2217	0.1633	0.0609	0.1152
Race - Asian	-0.0875	-0.0522	**0.000**	**0.000**
Race - Black	0.0480	0.0635	0.0172	**0.000**
Race - White	-0.0906	-0.0543	**0.000**	**0.000**
Biopsy - Excisional	0.0659	0.0442	**0.000**	**0.000**
Biopsy - Cytology	0.0206	**0.000**	**0.000**	**0.000**
Biopsy - Incisional	-0.0507	-0.0557	-0.0221	**0.000**
Biopsy - Resection	0.1129	0.0818	**0.000**	**0.000**
G1	-0.0987	-0.0627	**0.000**	**0.000**
G2	-0.2343	-0.1363	**0.000**	**0.000**
G3	-0.2359	-0.1326	**0.000**	0.0136
G4	-0.0008	0.0057	**0.000**	**0.000**
Clinical Stage I	**0.000**	**0.000**	**0.000**	-0.0661
Clinical Stage II	-0.0763	-0.0804	-0.0315	**0.000**
Clinical Stage III	-0.0492	**0.000**	**0.000**	**0.000**
Clinical Stage IV	0.1243	0.1541	0.0586	0.0116

A.2 Neural Network Approach

The evaluation for feature sets delineated through statistical methods and their conglomerations was performed via a neural network model, which was tailored to employ a continuous time survival loss function. The objective was to discern the feature sets that manifest the highest test c-index across various data types, including clinical, CNV, Mut, mRNA-Seq, RPPA-Exp, and DNAm, for both OS and DFS predictions. The empirical outcomes of this assessment are encapsulated in Figure A.3.

The analysis unveiled that certain data types, notably clinical, Mut, and DNAm, showcased feature sets that significantly outperformed others in terms of OS prediction. This disparity underscores the varying predictive power and relevance of different data types in survival analysis. Conversely, the comparative performance among feature sets for DFS prediction, and to some extent for OS in other data types, did not exhibit as pronounced differentiation. This observation suggests a more nuanced and balanced predictive capability across the board, highlighting the intrinsic complexity and interplay of factors influencing survival outcomes.

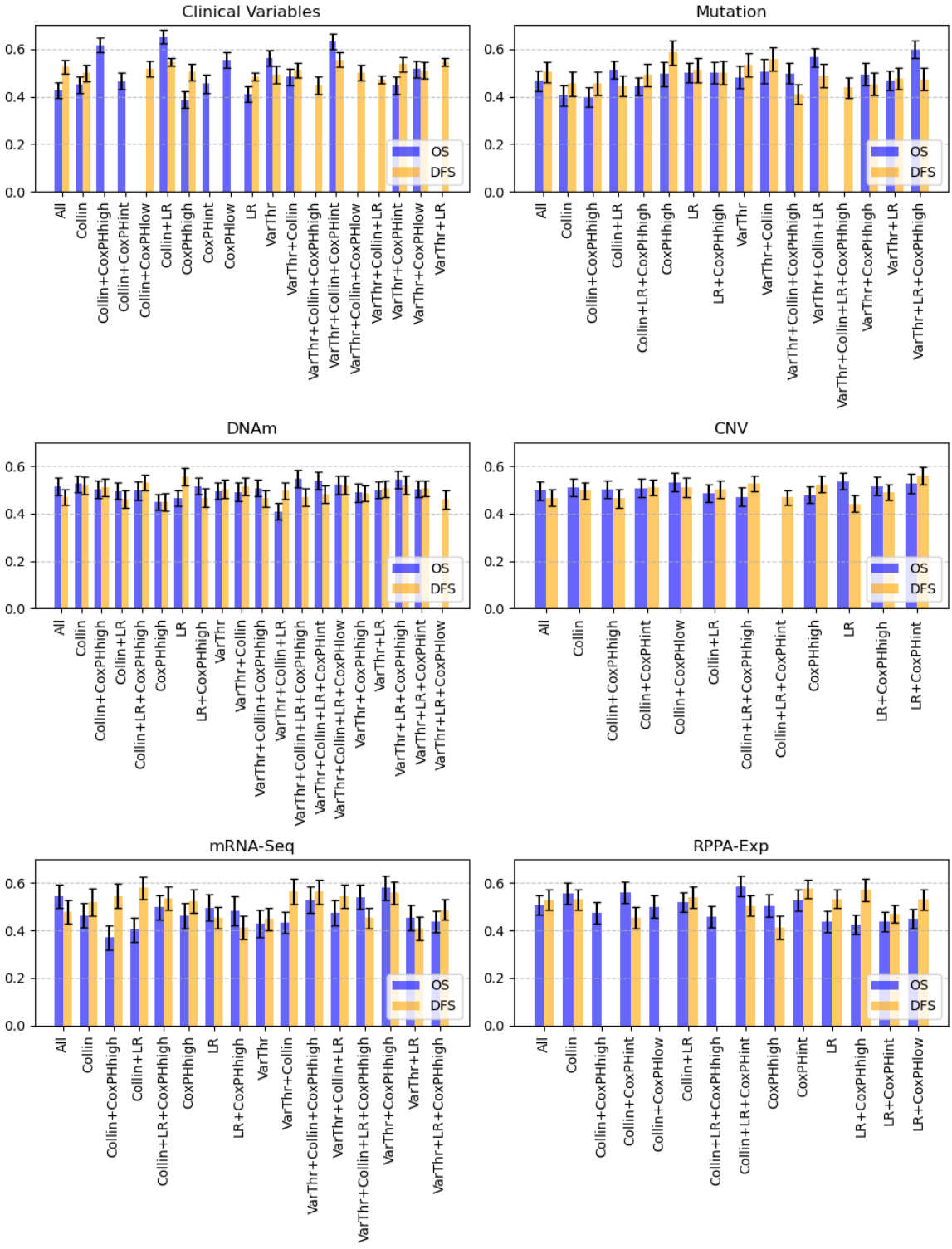


Figure A.3 Evaluation of Feature Sets by Neural Network Training. This figure presents comparative bar plots for six distinct data types for both overall (OS) and disease-free (DFS) survival prediction. For each data type, mean and 95% confidence interval values derived from a 5-fold cross-validation process, augmented with 1000 bootstrapping iterations, are depicted.

APPENDIX B. Additional Comparative Analysis

Additionally, early concatenation results are given as this was the fusion strategy that generally yielded good performance. 5-fold cross-validation outcome showed an improvement for medium datasets with 0.643 ± 0.0151 and 0.6555 ± 0.0161 test c-indices for medium-high and low, respectively. On the other hand, either no improvement or decrease in performance was seen in small datasts. In Small I data category, PORPOISE model yielded better performance with mean test c-index of 0.6773 ± 0.0118 compared to 0.6222 ± 0.0433 in OViTANet. The performance was approximately same in Small II dataset for both model. In Small III dataset a decrease in performance was observed with 0.6707 ± 0.0936 in OViTANet, however still exceeding the improved results in PORPOISE at 0.6407 ± 0.0174.

Table B.1
The table displays the 5-fold cross-validation results for overall survival prediction of the proposed model OViTANet and PORPOISE [2] with mean ± standard deviation of test concordance index. Image features were combined with the tabular data combinations using early concatenation for OViTANet and bilinear fusion for PORPOISE models.

Category	**Tabular Data**	**OViTANet**	**PORPOISE**
Large	Clinical	**0.6424 ± 0.0238**	0.6289 ± 0.0044
Medium-high	Clinical, RPPA-Exp	**0.643 ± 0.0151**	0.6141 ± 0.0247
Medium-low	CNV, DNAm, Mut	**0.6555 ± 0.0161**	0.5888 ± 0.011
Small I	Clinical, RPPA-Exp, mRNA-Seq	0.6222 ± 0.0433	**0.6773 ± 0.0118**
Small II	mRNA-Seq, DNAm, Mut	**0.6548 ± 0.0298**	0.6043 ± 0.0096
Small III	RPPA-Exp, mRNA-Seq, CNV, Mut, DNAm	**0.6707 ± 0.0936**	0.6407 ± 0.0174

REFERENCES

1. Filiot, A., Ghermi, R., Olivier, A. *et al.*, "Scaling self-supervised learning for histopathology with masked image modeling," *medRxiv*, 2023.

2. Chen, R. J., Lu, M. Y., Williamson, D. F. *et al.*, "Pan-cancer integrative histology-genomic analysis via multimodal deep learning," *Cancer Cell*, 2022.

3. Kandemir, H., *Preoperatif Görüntüleme Yöntemlerinin (MR, BT, 18F-FDG PET/BT) Over Kanserinin Yayılımını Saptamada ve Tedavi Yöntemini Belirlemede Etkinliği.* PhD thesis, Istanbul University, Istanbul, Turkey, 2018.

4. Morand, S., Devanaboyina, M., Staats, H. *et al.*, "Ovarian cancer immunotherapy and personalized medicine," *International Journal of Molecular Sciences*, Vol. 22, p. 6532, June 2021.

5. Surveillance Research Program, N. C. I., "Seer*explorer: An interactive website for seer cancer statistics." `https://seer.cancer.gov/statistics-network/explorer/`, Nov. 2023. Accessed: 2024-02-23.

6. Fathalla, M. F., "Incessant ovulation and ovarian cancer–a hypothesis re-visited," *Facts, Views & Vision in ObGyn*, Vol. 5, pp. 292–297, 2013.

7. American Joint Committee on Cancer (AJCC), "Ovarian cancer stages." `https://www.cancer.org/cancer/types/ovarian-cancer/detection-diagnosis-staging/staging.html`, Apr. 2018. Accessed: 2024-02-23.

8. Matsuno, R. K., Sherman, M. E., Visvanathan, K. *et al.*, "Agreement for tumor grade of ovarian carcinoma: analysis of archival tissues from the surveillance, epidemiology, and end results residual tissue repository," *Cancer Causes & Control*, Vol. 24, pp. 749 – 757, Feb. 2013.

9. Lheureux, S., Braunstein, M. and Oza, A. M., "Epithelial ovarian cancer: Evolution of management in the era of precision medicine," *CA: A Cancer Journal for Clinicians*, Vol. 69, pp. 280 – 304, May 2019.

10. Bast, R. C., Hennessy, B. and Mills, G. B., "The biology of ovarian cancer: new opportunities for translation," *Nature Reviews Cancer*, Vol. 9, pp. 415–428, June 2009.

11. Akter, S., Rahman, M. A., Hasan, M. N. *et al.*, "Recent advances in ovarian cancer: Therapeutic strategies, potential biomarkers, and technological improvements," *Cells*, Vol. 11, p. 650, Feb. 2022.

12. Guo, T., Dong, X., Xie, S. *et al.*, "Cellular mechanism of gene mutations and potential therapeutic targets in ovarian cancer," *Cancer Management and Research*, Vol. 13, pp. 3081–3100, Apr. 2021.

13. Hirst, J., Crow, J. and Godwin, A., *Ovarian Cancer Genetics: Subtypes and Risk Factors*, ch. 1. InTech, Oct. 2018.

14. Network, T. C. G. A. R., "Integrated genomic analyses of ovarian carcinoma," *Nature*, Vol. 474, pp. 609–615, June 2011.

15. Garsed, D. W., Pandey, A., Fereday, S. *et al.*, "The genomic and immune landscape of long-term survivors of high-grade serous ovarian cancer," *Nature Genetics*, Vol. 54, pp. 1853–1864, Dec. 2022.

16. Hentze, J., Høgdall, C. and Høgdall, E., "Methylation and ovarian cancer: Can DNA methylation be of diagnostic use?," *Molecular and Clinical Oncology*, Jan. 2019.

17. Teschendorff, A. E., Menon, U., Gentry-Maharaj, A. *et al.*, "An epigenetic signature in peripheral blood predicts active ovarian cancer," *PLoS ONE*, Vol. 4, p. e8274, Dec. 2009.

18. Song, K., and Artibani, M., "The role of dna methylation in ovarian cancer chemoresistance: A narrative review," *Health Science Reports*, Vol. 6, Apr. 2023.

19. Gong, T. T., Guo, S., Liu, F. H. *et al.*, "Proteomic characterization of epithelial ovarian cancer delineates molecular signatures and therapeutic targets in distinct histological subtypes," *Nature Communications*, Vol. 14, no. 7802, 2023.

20. Kleinbaum, D. G., and Klein, M., *Survival Analysis: A Self-Learning Text*, ch. 1. Springer, 2012.

21. Musa, K. I., Mansor, W. N. A. W. and Hanis, T. M., *Data Analysis in Medicine and Health Using R*, ch. 11. CRC Press, 2023.

22. Kleinbaum, D. G., and Klein, M., *Survival Analysis: A Self-Learning Text*, ch. 7. Springer, 2012.

23. Kaplan, E. L., and Meier, P., "Nonparametric estimation from incomplete observations," *Journal of the American Statistical Association*, Vol. 53, no. 282, pp. 457–481, 1958.

24. Scher, C., Davidov, R. and Geara, E., *Experimental designs for addiction research*, ch. 4, pp. 31–53. Elsevier, 2023.

25. Kleinbaum, D. G., and Klein, M., *Survival Analysis: A Self-Learning Text*, ch. 2. Springer, 2012.

26. Kleinbaum, D. G., and Klein, M., *Survival Analysis: A Self-Learning Text*, ch. 3. Springer, 2012.

27. Faraggi, D., and Simon, R., "A neural network model for survival data," *Statistics in Medicine*, Vol. 14, pp. 73–82, Jan. 1995.

28. Mariani, L., Coradini, D., Biganzoli, E. *et al.*, "Prognostic factors for metachronous contralateral breast cancer: A comparison of the linear cox regression model and its artificial neural network extension," *Breast Cancer Research and Treatment*, Vol. 44, pp. 167 – 178, June 1997.

29. Xiang, A., Lapuerta, P., Ryutov, A. *et al.*, "Comparison of the performance of neural network methods and cox regression for censored survival data," *Computational Statistics & Data Analysis*, Vol. 34, pp. 243 – 257, Aug. 2000.

30. Sargent, D. J., "Comparison of artificial neural networks with other statistical approaches: Results from medical data sets," *Cancer*, Vol. 91, no. S8, pp. 1636 – 1642, 2001.

31. Katzman, J. L., Shaham, U., Cloninger, A. *et al.*, "Deepsurv: personalized treatment recommender system using a cox proportional hazards deep neural network," *BMC Medical Research Methodology*, Vol. 18, Feb. 2018.

32. Kvamme, H., Borgan, Ø. and Scheel, I., "Time-to-event prediction with neural networks and cox regression," *J. Mach. Learn. Res.*, Vol. 20, pp. 129:1–129:30, 2019.

33. Yousefi, S., Amrollahi, F., Amgad, M. *et al.*, "Predicting clinical outcomes from large scale cancer genomic profiles with deep survival models," *Scientific Reports*, Vol. 7, Sept. 2017.

34. Zhu, X., Yao, J. and Huang, J., "Deep convolutional neural network for survival analysis with pathological images," in *2016 IEEE International Conference on Bioinformatics and Biomedicine (BIBM)*, pp. 544–547, 2016.

35. Kvamme, H., and Borgan, ø., "Continuous and discrete-time survival prediction with neural networks," *Lifetime Data Analysis*, Vol. 27, pp. 710 – 736, Oct. 2021.

36. Lee, C., Zame, W., Yoon, J. *et al.*, "Deephit: A deep learning approach to survival analysis with competing risks," *Proceedings of the AAAI Conference on Artificial Intelligence*, Vol. 32, Apr. 2018.

37. Gensheimer, M. F., and Narasimhan, B., "A scalable discrete-time survival model for neural networks," *PeerJ*, Vol. 7, p. e6257, Jan. 2019.

38. Harrel, F. E., Lee, K. L. and Mark, D. B., "Multivariable prognostic models: Issues in developing models, evaluating assumptions and adequacy, and measuring and reducing errors," *Statistics in Medicine*, Vol. 15, pp. 361 – 387, Feb. 1996.

39. Graf, E., Schmoor, C., Sauerbrei, W. *et al.*, "Assessment and comparison of prognostic classification schemes for survival data," *Statistics in Medicine*, Vol. 18, pp. 2529 – 2545, Sept. 1999.

40. Wang, X., Yang, S., Zhang, J. *et al.*, "Transpath: Transformer-based self-supervised learning for histopathological image classification," in *International Conference on Medical Image Computing and Computer-Assisted Intervention*, pp. 186–195, Springer, 2021.

41. Yang, Z., Zhang, Y., Zhuo, L. *et al.*, "Prediction of prognosis and treatment response in ovarian cancer patients from histopathology images using graph deep learning: a multicenter retrospective study," *European Journal of Cancer*, Vol. 199, p. 113532, Mar. 2024.

42. Azarianpour, S., Corredor, G., Bera, K. *et al.*, "Computational image features of immune architecture is associated with clinical benefit and survival in gynecological cancers across treatment modalities," *Journal for ImmunoTherapy of Cancer*, Vol. 10, p. e003833, Feb. 2022.

43. Szegedy, C., Ioffe, S., Vanhoucke, V. *et al.*, "Inception-v4, inception-resnet and the impact of residual connections on learning," 2016.

44. Fu, Y., Jung, A. W., Torne, R. V. *et al.*, "Pan-cancer computational histopathology reveals mutations, tumor composition and prognosis," *Nature Cancer*, Vol. 1, pp. 800 – 810, July 2020.

45. Laury, A. R., Blom, S., Ropponen, T. *et al.*, "Artificial intelligence-based image analysis can predict outcome in high-grade serous carcinoma via histology alone," *Scientific Reports*, Vol. 11, Sept. 2021.

46. Nero, C., Boldrini, L., Lenkowicz, J. *et al.*, "Deep-Learning to Predict BRCA Mutation and Survival from Digital H&E Slides of Epithelial Ovarian Cancer," *International Journal of Molecular Sciences*, Vol. 23, p. 11326, Sept. 2022.

47. Liu, Y., Lawson, B. C., Huang, X. *et al.*, "Prediction of ovarian cancer response to therapy based on deep learning analysis of histopathology images," *Cancers*, Vol. 15, p. 4044, Aug. 2023.

48. Weinstein, J. N., Collisson, E. A., Mills, G. B. *et al.*, "The cancer genome atlas pan-cancer analysis project," *Nature Genetics*, Vol. 45, pp. 1113–1120, Sept. 2013.

49. Lu, M. Y., Williamson, D. F., Chen, T. Y. *et al.*, "Data-efficient and weakly supervised computational pathology on whole-slide images," *Nature Biomedical Engineering*, Vol. 5, no. 6, pp. 555–570, 2021.

50. Cerami, E., Gao, J., Dogrusoz, U. *et al.*, "The cBio Cancer Genomics Portal: An open platform for exploring multidimensional cancer genomics data," *Cancer Discovery*, Vol. 2, pp. 401–404, May 2012.

51. Li, B., and Dewey, C. N., "RSEM: Accurate transcript quantification from RNA-Seq data with or without a reference genome," *BMC Bioinformatics*, Vol. 12, Aug. 2011.

52. He, K., Zhang, X., Ren, S. *et al.*, "Deep residual learning for image recognition," 2015.

53. Liu, Z., Lin, Y., Cao, Y. *et al.*, "Swin transformer: Hierarchical vision transformer using shifted windows," in *Proceedings of the IEEE/CVF International Conference on Computer Vision (ICCV)*, 2021.

54. Simon, N. R., Friedman, J. H., Hastie, T. J. *et al.*, "Regularization paths for Cox's proportional hazards model via coordinate descent," *Journal of statistical software*, Vol. 39,5, pp. 1–13, 2011.

55. Ching, T., Zhu, X. and Garmire, L. X., "Cox-nnet: An artificial neural network method for prognosis prediction of high-throughput omics data," *PLOS Computational Biology*, Vol. 14, pp. 1–18, 04 2018.

56. Ching, T., "cox-nnet." `https://github.com/traversc/cox-nnet`, 2017.

57. Dosovitskiy, A., Beyer, L., Kolesnikov, A. *et al.*, "An image is worth 16x16 words: Transformers for image recognition at scale," 2021.

58. "Kegg pathway database." `https://www.genome.jp/kegg/pathway.html`, 2024. Accessed: 2024-02-24.

59. Flaum, N., Crosbie, E. J., Edmondson, R. J. *et al.*, "Epithelial ovarian cancer risk: A review of the current genetic landscape," *Clinical Genetics*, Vol. 97, pp. 54–63, May 2019.

60. "RAD51 RAD51 recombinase [Homo sapiens (human)] - Gene - NCBI." `https://www.ncbi.nlm.nih.gov/gene/5888`, 2024. Accessed: 2024-02-23.

61. "CSMD3 CUB and Sushi multiple domains 3 [Homo sapiens (human)] - Gene - NCBI." `https://www.ncbi.nlm.nih.gov/gene/114788`, 2024. Accessed: 2024-02-23.

62. Chen, C.-H., Shyu, M.-K., Wang, S.-W. *et al.*, "MUC20 promotes aggressive phenotypes of epithelial ovarian cancer cells via activation of the integrin β1 pathway," *Gynecologic Oncology*, Vol. 140, pp. 131–137, Jan. 2016.

63. Nymoen, D. A., Holth, A., Hetland Falkenthal, T. E. *et al.*, "CIAPIN1 and ABCA13 are markers of poor survival in metastatic ovarian serous carcinoma," *Molecular Cancer*, Vol. 14, Feb. 2015.

64. Zhao, Y., Li, Q., Wu, X. *et al.*, "Upregulation of p27Kip1 by demethylation sensitizes cisplatin-resistant human ovarian cancer SKOV3 cells," *Molecular Medicine Reports*, Vol. 14, pp. 1659–1666, June 2016.

65. Bi, L., Yang, Q., Yuan, J. *et al.*, "MicroRNA-127-3p acts as a tumor suppressor in epithelial ovarian cancer by regulating the BAG5 gene," *Oncology Reports*, Vol. 36, pp. 2563–2570, Aug. 2016.

66. Basuli, D., Tesfay, L., Deng, Z. *et al.*, "Iron addiction: a novel therapeutic target in ovarian cancer," *Oncogene*, Vol. 36, pp. 4089–4099, Mar. 2017.

67. Xia, P., Choi, A. H., Deng, Z. *et al.*, "Cell membrane-anchored MUC4 promotes tumorigenicity in epithelial carcinomas," *Oncotarget*, Vol. 8, pp. 14147–14157, Nov. 2016.

68. Wang, L., Zhao, S. and Yu, M., "Mechanism of low expression of miR-30a-5p on epithelial-mesenchymal transition and metastasis in ovarian cancer," *DNA and Cell Biology*, Vol. 38, pp. 341–351, Apr. 2019.

69. Hefler, L. A., Ludwig, E., Lampe, D. *et al.*, "Polymorphisms of the endothelial nitric oxide synthase gene in ovarian cancer," *Gynecologic Oncology*, Vol. 86, pp. 134–137, Aug. 2002.

70. Henry, C., Hacker, N. and Ford, C., "Silencing ROR1 and ROR2 inhibits invasion and adhesion in an organotypic model of ovarian cancer metastasis," *Oncotarget*, Vol. 8, pp. 112727–112738, Nov. 2017.

71. Duyndam, M. C., van Berkel, M. P., Dorsman, J. C. *et al.*, "Cisplatin and doxorubicin repress vascular endothelial growth factor expression and differentially down-regulate hypoxia-inducible factor i activity in human ovarian cancer cells," *Biochemical Pharmacology*, Vol. 74, pp. 191–201, July 2007.

72. Zhao, Y., Zhou, X., He, Y. *et al.*, "SLC6A1-miR133a-CDX2 loop regulates SK-OV-3 ovarian cancer cell proliferation, migration and invasion," *Oncology Letters*, Aug. 2018.

73. Gusev, A., Lawrenson, K., Lin, X. *et al.*, "A transcriptome-wide association study of high-grade serous epithelial ovarian cancer identifies new susceptibility genes and splice variants," *Nature Genetics*, Vol. 51, 05 2019.

74. Mase, S., Shinjo, K., Totani, H. *et al.*, "ZNF671 DNA methylation as a molecular predictor for the early recurrence of serous ovarian cancer," *Cancer Science*, Vol. 110, pp. 1105–1116, Jan. 2019.

75. Veneris, J. T., Matulonis, U. A., Liu, J. F. *et al.*, "Choosing wisely: Selecting PARP inhibitor combinations to promote anti-tumor immune responses beyond BRCA mutations," *Gynecologic Oncology*, Vol. 156, pp. 488–497, Feb. 2020.

76. Bram, E. E., Stark, M., Raz, S. *et al.*, "Chemotherapeutic Drug-Induced ABCG2 Promoter Demethylation as a Novel Mechanism of Acquired Multidrug Resistance," *Neoplasia*, Vol. 11, pp. 1359–IN11, Dec. 2009.

77. Yan, X., Yin, J., Yao, H. *et al.*, "Increased rxpression of Annexin A3 Is a mechanism of platinum resistance in ovarian cancer," *Cancer Research*, Vol. 70, pp. 1616–1624, Feb. 2010.

78. Yan, Y., Wang, Y., Xiong, Y. *et al.*, "Reduced Klotho expression contributes to poor survival rates in human patients with ovarian cancer, and overexpression of Klotho inhibits the progression of ovarian cancer partly via the inhibition of systemic inflammation in nude mice," *Molecular Medicine Reports*, Vol. 15, pp. 1777–1785, Feb. 2017.

79. Sun, Y., Lei, B. and Huang, Q., "SOX18 affects cell viability, migration, invasiveness, and apoptosis in hepatocellular carcinoma (HCC) cells by participating in epithelial-to-mesenchymal transition (EMT) progression and adenosine monophosphate activated protein kinase (AMPK)/mammalian target of rapamycin (mTOR)," *Medical Science Monitor*, Vol. 25, pp. 6244–6254, Aug. 2019.

80. Wu, L., Ling, Z.-H., Wang, H. *et al.*, "Upregulation of SCNN1A Promotes Cell Proliferation, Migration, and Predicts Poor Prognosis in Ovarian Cancer Through Regulating Epithelial-Mesenchymal Transformation," *Cancer Biotherapy and Radiopharmaceuticals*, Vol. 34, pp. 642–649, Dec. 2019.

81. Nakayama, K., Kanzaki, A., Ogawa, K. *et al.*, "Copper-transporting P-type adenosine triphosphatase (ATP7B) as a cisplatin based chemoresistance marker in ovarian carcinoma: Comparative analysis with expression of MDR1, MRP1, MRP2, LRP and BCRP," *International Journal of Cancer*, Vol. 101, pp. 488–495, Sept. 2002.

82. Gharpure, K. M., Pradeep, S., Sans, M. *et al.*, "FABP4 as a key determinant of metastatic potential of ovarian cancer," *Nature Communications*, Vol. 9, p. 2923, July 2018.

83. Sopo, M., Anttila, M., Hämäläinen, K. *et al.*, "Expression profiles of VEGF-A, VEGF-D and VEGFR1 are higher in distant metastases than in matched primary high grade epithelial ovarian cancer," *BMC Cancer*, Vol. 19, June 2019.

84. Tilli, T. M., Franco, V. F., Robbs, B. K. *et al.*, "Osteopontin-c splicing isoform contributes to ovarian cancer progression," *Molecular Cancer Research*, Vol. 9, no. 3, 2011.

85. Mills, K. A., Quinn, J. M., Roach, S. T. *et al.*, "p5RHH nanoparticle-mediated delivery of AXL siRNA inhibits metastasis of ovarian and uterine cancer cells in mouse xenografts," *Scientific Reports*, Vol. 9, Mar. 2019.

86. Xu, Z., Tang, H., Zhang, T. *et al.*, "TEX19 promotes ovarian carcinoma progression and is a potential target for epitope vaccine immunotherapy," *Life Sciences*, Vol. 241, p. 117171, Jan. 2020.

87. Peng, Y., Kajiyama, H., Yuan, H. *et al.*, "PAI-1 secreted from metastatic ovarian cancer cells triggers the tumor-promoting role of the mesothelium in a feedback loop to accelerate peritoneal dissemination," *Cancer Letters*, Vol. 442, pp. 181–192, Feb. 2019.

88. Raspaglio, G., Petrillo, M., Martinelli, E. *et al.*, "Sox9 and Hif-2α regulate TUBB3 gene expression and affect ovarian cancer aggressiveness," *Gene*, Vol. 542, pp. 173–181, June 2014.

89. Sheng, Q., Zhang, Y., Wang, Z. *et al.*, "Cisplatin-mediated down-regulation of miR-145 contributes to up-regulation of PD-L1 via the c-Myc transcription factor in cisplatin-resistant ovarian carcinoma cells," *Clinical and Experimental Immunology*, Vol. 200, pp. 45–52, Dec. 2019.

90. Wang, J., Garbutt, C., Ma, H. *et al.*, "Expression and role of autophagy-associated p62 (SQSTM1) in multidrug resistant ovarian cancer," *Gynecologic Oncology*, Vol. 150, pp. 143–150, July 2018.

91. de Leon, M., Cardenas, H., Vieth, E. *et al.*, "Transmembrane protein 88 (TMEM88) promoter hypomethylation is associated with platinum resistance in ovarian cancer," *Gynecologic Oncology*, Vol. 142, pp. 539–547, Sept. 2016.

92. Wang, Q., Lou, W., Di, W. *et al.*, "Prognostic value of tumor PD-L1 expression combined with CD8 + tumor infiltrating lymphocytes in high grade serous ovarian cancer," *International Immunopharmacology*, Vol. 52, pp. 7–14, Nov. 2017.

93. Zhu, X., Yan, S., Xiao, S. *et al.*, "Knockdown of ALPK2 inhibits the development and progression of ovarian cancer," *Cancer Cell International*, Vol. 20, June 2020.

94. Lou, T., Zhuang, H., Liu, C. *et al.*, "HDAC3 positively regulates HE4 expression to promote ovarian carcinoma progression," *Archives of Biochemistry and Biophysics*, Vol. 675, p. 108044, Oct. 2019.

95. Luo, N., Chen, D.-d., Liu, L. *et al.*, "CXCL12 promotes human ovarian cancer cell invasion through suppressing ARHGAP10 expression," *Biochemical and Biophysical Research Communications*, Vol. 518, pp. 416–422, Oct. 2019.

96. Cesaratto, L., Grisard, E., Coan, M. *et al.*, "BNC2 is a putative tumor suppressor gene in high-grade serous ovarian carcinoma and impacts cell survival after oxidative stress," *Cell Death & Disease*, Vol. 7, pp. e2374–e2374, Sept. 2016.

97. Seo, E. J., Kim, D. K., Jang, I. H. *et al.*, "Hypoxia-NOTCH1-SOX2 signaling is important for maintaining cancer stem cells in ovarian cancer," *Oncotarget*, Vol. 7, pp. 55624–55638, July 2016.

98. Cortés, M., Sánchez-Moral, L., de Barrios, O. *et al.*, "Tumor-associated macrophages (TAMs) depend on ZEB1 for their cancer-promoting roles," *The EMBO Journal*, Vol. 36, pp. 3336–3355, Oct. 2017.

99. Wan, L., Xu, K., Wei, Y. *et al.*, "Phosphorylation of EZH2 by AMPK suppresses PRC2 methyltransferase activity and oncogenic function," *Molecular Cell*, Vol. 69, pp. 279–291.e5, Jan 2018.

100. Ren, F., Shi, H., Zhang, G. *et al.*, "Expression of deleted in liver cancer 1 and plasminogen activator inhibitor 1 protein in ovarian carcinoma and their clinical significance," *Journal of Experimental & Clinical Cancer Research*, Vol. 32, Aug. 2013.

101. Wang, Y., Jiang, J., He, L. *et al.*, "Effect of lamin-a expression on migration and nuclear stability of ovarian cancer cells," *Gynecologic Oncology*, Vol. 152, pp. 166–176, Jan. 2019.

102. Yang, J., Xing, H., Lu, D. *et al.*, "Role of Jagged1/STAT signalling in platinum-resistant ovarian cancer," *Journal of Cellular and Molecular Medicine*, Vol. 23, pp. 4005–4018, Apr. 2019.

103. Yang, X., Zhou, S., Yang, C. *et al.*, "CCNB1, negatively regulated by miR-559, promotes the proliferation, migration, and invasion of ovarian carcinoma cells," *Molecular Biotechnology*, Vol. 64, pp. 958–969, Mar. 2022.

104. Li, X.-F., Hua, T., Li, Y. *et al.*, "The HSP70 gene predicts prognosis and response to chemotherapy in epithelial ovarian cancer," *Annals of Translational Medicine*, Vol. 9, pp. 806–806, May 2021.

105. Sawada, K., Radjabi, A. R., Shinomiya, N. *et al.*, "c-met overexpression is a prognostic factor in ovarian cancer and an effective target for inhibition of peritoneal dissemination and invasion," *Cancer Research*, Vol. 67, pp. 1670–1679, Feb. 2007.

106. Assidi, M., "High N-Cadherin protein expression in ovarian cancer predicts poor survival and triggers cell invasion," *Frontiers in Oncology*, Vol. 12, Apr. 2022.

107. Al-Alem, L. F., Baker, A. T., Pandya, U. M. *et al.*, "Understanding and targeting apoptotic pathways in ovarian cancer," *Cancers*, Vol. 11, p. 1631, Oct. 2019.

108. Cai, M., Hu, Z., Liu, J. *et al.*, "Beclin 1 expression in ovarian tissues and its effects on ovarian cancer prognosis," *International Journal of Molecular Sciences*, Vol. 15, pp. 5292–5303, Mar. 2014.

109. Shen, F., Zhang, X., Zhang, Y. *et al.*, "Hormone receptors expression in ovarian cancer taking into account menopausal status: a retrospective study in chinese population," *Oncotarget*, Vol. 8, pp. 84019–84027, Aug. 2017.